

Politecnico di Torino

Karlsruher Institut für Technologie

Influence of Particle Size Distribution on Fluidization and Reduction of Iron Oxide Particles with Hydrogen in a Fluidized Bed Reactor

Master's Thesis
by

Francesco Notarianni

Politecnico di Torino - Dipartimento di Ingegneria Meccanica (DIMEAS)
Karlsruher Institut für Technologie - Engler-Bunte-Institut - Verbrennungstechnik

Main Supervisor (Italy):	Prof. Matteo Fasano
Co-Supervisor:	Dr. Fabian Hagen
Additional Support:	M. Sc. Malte Seitz

Submission Period: 14/04/2025 – 16/02/2026

Contents

List of Figures **iv**

List of Tables **v**

Abstract **1**

1 Introduction **3**
1.1 Background and Motivation 3
1.2 Objectives of the Thesis 5
1.3 Thesis Structure 5

2 Theoretical Background **7**
2.1 Iron Oxide Reduction 7
2.1.1 Temperature Influence 10
2.1.2 Pressure Influence 11
2.1.3 Gas Composition Influence 12
2.1.4 Grain Size Influence 13
2.1.5 Porosity Influence 14
2.1.6 Mineralogy Influence 14
2.1.7 Gangue Influence 15
2.1.8 Gas Flow Rate Influence 16
2.1.9 Gas Residence Time Influence 18
2.2 Hydrogen as a Reducing Agent 19
2.2.1 Kinetic Mechanisms 22
2.2.2 Environmental Aspects 23
2.3 Fluidized Bed Reactors 24
2.3.1 Gas Properties Influence 31
2.3.2 Bulk Particle Properties Influence 32
2.3.3 Particle Properties Influence 33
2.3.4 Minimum Fluidization Velocity Calculations 35
2.4 Cooling Time and Temperature Profiles 40

3 Materials and Methods **43**
3.1 Experimental Setup 43
3.2 Analysis of Historical Sensor Data from the Furnace 47
3.3 Minimum Fluidization Velocity Determination 49
3.3.1 Excel Model 49
3.3.2 Cold Bed Reactor 50
3.4 Particle Characterization and Powder Selection 56

3.4.1 Calorimetric analysis . . . 57
3.4.2 TGA Analysis . . . 58
3.4.3 BET Analysis . . . 59
3.4.4 XRD Analysis . . . 62
3.4.5 Foreign Element Analysis . . . 63
3.4.6 External Analysis of Particle Size Distribution . . . 64

4 Results **67**
4.1 Characterization Results . . . 67
4.1.1 TGA Results . . . 67
4.1.2 BET Results . . . 70
4.1.3 TGA compared to BET Results . . . 73
4.1.4 XRD Results . . . 75
4.1.5 Particle Size Distribution Results . . . 77
4.1.6 Electron Spectroscopy Imaging . . . 78
4.1.7 Optical Emission Spectroscopy . . . 82
4.1.8 Foreign Elements in the Powders . . . 84
4.2 Fluidization Results . . . 86
4.2.1 Theoretical Results . . . 86
4.2.2 Experimental Results . . . 88
4.2.3 Comparison of Theoretical and Experimental Results . . . 95
4.3 High Temperature Reduction Results . . . 96
4.3.1 Calorimetric Analysis . . . 97
4.3.2 TGA Analysis . . . 97
4.3.3 BET Analysis . . . 101
4.4 Summary of Powder Characteristics . . . 102

5 Discussion **105**
5.1 Changes in BET Data . . . 105
5.2 Estimation of the Reduction degree . . . 109
5.3 Possible Solutions . . . 110

6 Conclusions **111**

A Appendix **113**

Bibliography **117**

List of Figures

1.1 The primary causes and the wide-ranging impacts of climate change. Some effects act as positive feedbacks that amplify climate change. [1] 3

1.2 Metal combustor and possible applications [4] 5

2.2 Baur-Glässner diagram for the Fe−O−H_2 and Fe−O−C system. [11] . 9

2.3 Effect of temperature on reduction rate for the reducing wüstite with hydrogen. [11] 11

2.4 Effect of absolute pressure on reduction rate of hematite reduced at 1053 K. [12] 12

2.5 Influence of gas composition on the reduction rate of hematite pellets at 850 °C. [11] 13

2.6 Influence of particle size on the reduction rate of magnetite concentrate with hydrogen at 400 °C. [11] 14

2.7 Effect of mineralogy on the reduction rate with hydrogen and carbon monoxide.[11] 15

2.8 Effect of Al_2O_3 doping amount on the reduction rate of magnetite at 750 °C. [11] 16

2.9 Effect of flow rate on reduction curves at 927 °C. [18] 17

2.10 Effect of molar flow rate on reduction rate constant, k [18]. 18

2.11 a) Progress of reduction over time for different gas mixtures and b) Procedure for determining the effective diffusion coefficient [11][20]. . 20

2.12 Temperature programmed reduction (TPR) patterns of different heating rates: (a) = 3 K/min, (b) = 7 K/min, (c) = 21 K/min [22]. . . . 21

2.13 Physical and chemical processes during redox reactions [24]. 23

2.14 Change of pore structure during reaction process [24]. 23

2.15 Three types of fluidized bed reactors [30]. 24

2.16 Some industrial fluidized bed and circulating fluidized bed processes [31]. 25

2.17 Typical bubbling gas-solid fluidized bed [29]. 27

2.18 The five different regimes of fluidization [29]. In this figure U_{mf} is the minimum fluidization velocity, U_{mb} is the minimum bubbling velocity, U_k is the velocity at which the system transitions to a turbulent bed regime, and U_{tr} is the transport velocity (the velocity at which all particles can be transported out of the fluidized bed by gas). 28

2.19 Flow regime map for gas-solids fluidization. Heavy lines indicate transition velocities, while the shaded region bounded by thin lines is the typical operating range of bubbling fluidized beds [34]. 29

2.20 Geldart powder classification group boundaries for fluidization in air at 20 °C and 1 atm pressure [36] [37]. 31

2.21 Typical sphericities of common materials [37]. 34

2.22 Graphical identification of the minimum fluidization velocity [37]. . . 36

2.23 Minimum fluidization velocity, u_{mf} , for spherical particles of different densities and mean diameters in air at 20 °C and 1 atm pressure, and in water at 20 °C [37]. 38

2.24 Properties used in minimum fluidization model [44]. Since the values depend on the material (iron-oxide), they can be used for a preliminary theoretical calculation. 40

2.25 Comparison of gas and oven temperature trends during a representative experimental run and its subsequent cooling phase. As illustrated, the gas temperature remains consistently lower than that of the oven throughout the entire process. 41

3.1 The furnace used in the experiments, inside of the laboratory. 44

3.2 Scheme of the internal structure of the furnace. The tip of the gas temperature sensor (indicated with number 3 in the picture) is located near the first 90° bend of the gas input line when it is mounted. From IBT's manual of the furnace. 45

3.3 The cold bed reactor used for the experiments. 51

3.4 Diagram of the various connections between elements. The outputs of the flow controllers is the signal that effectively controls the amount of gas, and the input of the differential pressure sensor is the signal obtained from the pressure drop. 53

3.5 Screenshot from the LabVIEW program during use. The left graph showed the 5 s view of the pressure drop, the right one showed the 30 s view. The topmost button allowed to start and stop the recording of the data inside of the file specified in the "Pfad Druckdifferenz" field. The "Drucksignal" showed the conversion to a pressure from the instantaneous "Spannungssignal" (voltage signal) received from the Halstrup Walcher pressure difference sensor. 54

3.6 Visual of the FlowView program used to control the flow of the gas through the bed. 55

3.7 The calorimetry vessel used for the analyses [47]. 57

3.8 Schematics of the internal structure of the TGA machine [48]. 58

3.9 The TGA machine used for the analyses. 59

3.10 The BET adsorption model. N_i represents the adsorption sites that are covered by i layers of adsorbed molecules. At adsorption equilibrium N_i must remain constant, for every value of i [49]. 60

3.11 The BET machine used for the analyses. 61

3.12 A typical XRD graph for an iron oxide sample. The peaks correspond to the various elements present in the sample [52]. 63

3.13 Particle size distribution of the different powders. 65

4.1 TGA plots for the 01/25 powder. 68

4.2 TGA plots for the 36/24 powder. 68

4.3 TGA plots for the 39/24 powder. 69

4.4 Correlation between the minimum fluidization velocity and the BET specific surface area 73

4.5 The new data is shown in blue, whereas the data from the previous research is in orange. Every point corresponds to a different material. 74

4.6 Comparison of images at 500x and 2500x of the various powders. . . . 76

4.7 Pictures for the 01/25 powder. 78

4.8 Pictures for the 36/24 powder. 80

4.9 Pictures for the MP24 powder. 81

4.10 Concentration of elements inside of the three iron ores. 82

4.11 Percentages of elements inside of the three iron ores, con asse y dal 95%. 82

4.12 90

4.12 The graphs obtained in the second experimental run for the pressure drop of the various diffuser plate designs. 91

4.13 92

4.13 93

4.13 Comparisons between different volumes of powder for the new fluidization tests. 94

4.14 Reduction degrees calculated for each powder at 500 °C and 600 °C. . 97

4.15 98

4.15 99

4.15 Graphs of the TGA experiments on the combusted powders. 100

A.1 Examples of graphs that show an atypical shape. 114

A.2 Graph of the pressure drop through the diffuser. The step at 20 l/min is due to the change in flow controller, that, as stated previously, is less accurate at lower flows. 115

List of Tables

2.1 Particle properties and gas relative humidities (RHs) that generally promote good "fluidizability" [37]. 33

3.1 Average, standard deviation and standard deviation as a percentage of the average for the cooling coefficients. 48

4.1 Mass loss of the samples, expressed as a percentile value of the initial mass. 69

4.2 t_{10} times for the various powders at different temperatures, in minutes. 70

4.3 t_{90} times for the various powders at different temperatures, in minutes. 70

4.4 Results from the BET plot anlysis. 71

4.5 Results from the mesopores analysis, obtained by averaging the results from the BJH, CI, DH and INNES plots. 71

4.6 Results from the micropores analysis. 71

4.7 Diameters of the particles corresponding to the respective cumulative volume, in μm. 77

4.8 Concentrations of the main elements obtained from the ICP-OES analysis. Due to the limited legibility of the labels in the externally provided graph (Figure 4.10), the exact numerical values for the most relevant species are reported here. 83

4.9 Percentages of the main elements obtained from the ICP-OES analysis. 83

4.10 Predicted minimum fluidization velocities based on the different theoretical equations, with the average, the standard deviation and the standard deviation as a percentage of the average for the calculated velocities. 87

4.11 Calorimetric values in J/g for the different powders. 97

4.12 BET results for the powders that reacted at 500 °C. 101

4.13 BET results for the powders that reacted at 600 °C. 102

4.14 Summary of the main physical, chemical, and behavioral properties of the tested iron-oxide powders. 103

Abstract

The transition towards carbon-neutral energy systems has identified the iron/iron-oxide cycle as a promising solution for long-duration energy storage and transport, due to iron's abundance, high energy density, and recyclability. However, the industrial viability of this technology relies on the efficient regeneration of iron oxides using green hydrogen in fluidized bed reactors. A key challenge lies in optimizing this reduction process, which is strongly influenced by the physical and chemical variability of the iron ore powders.

This thesis investigates the influence of particle size distribution, morphology, and chemical composition on the fluidization behaviour and hydrogen reduction of iron-oxide powders. A multi-technique approach was applied, combining detailed particle characterization (using TGA, BET, XRD, SEM/EDS and ICP-OES analyses) with cold-bed tests and high-temperature reduction experiments at 500 and 600 °C.

The results demonstrate that reduction and fluidization quality are not determined by particle size alone but are controlled by the coupled effects of particle microstructure and impurity phases. Specifically, the presence of foreign elements (such as Mg, Al, and Si) was found to alter both the mechanical stability of the fluidized bed and the reaction kinetics. Finally, critical experimental limitations regarding particle entrainment and re-oxidation were identified. Practical recommendations (including optimized protocols for fines collection and inert gas cooling) are proposed to increase experimental reliability and to better resolve intrinsic material behaviour in future campaigns.

1. Introduction

1.1 Background and Motivation

In the last decades the quest for new and greener ways to produce and store energy has driven research, since it is widely accepted nowadays that fossil fuels and their use are a major cause of global warming and climate change. If their use is not stopped or at least waned, the possibility of devastating and irreversible effects on the flora, fauna and in general on the natural environment increase every year.

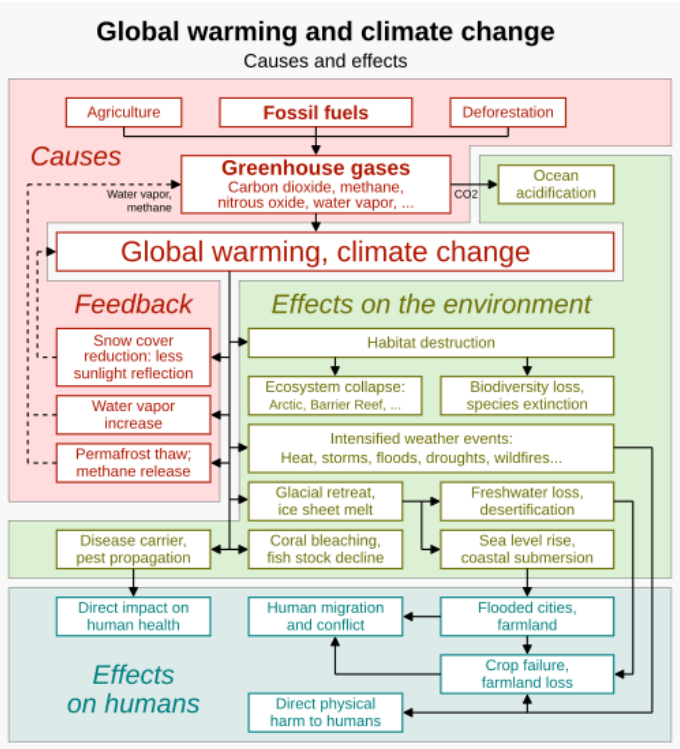


Figure 1.1: The primary causes and the wide-ranging impacts of climate change. Some effects act as positive feedbacks that amplify climate change. [1]

An alternative green energy storage solution is sorely needed, and metal fuels could provide one. Metal fuels offer a compelling solution because of their innate high energy density, and ability to be recycled through clean processes. Moreover, they can be burned in air or made to react with water, and having solid products of the reaction [2], their handling is easier compared to other alternatives. Moreover metals, when burned in air, have the highest volumetric heat production, making them ideal for applications in which energy density is crucial [3].

Compared to conventional electrochemical batteries, iron-based metal fuels do not rely on hazardous electrolytes, acids, or toxic raw materials. Consequently, they present a significantly lower environmental and health risk. Furthermore, solid metal powders are much easier and safer to handle and store than hydrogen or ammonia, which require specialized pressurized or cryogenic vessels.

There is also the possibility of using hydrocarbon fuels to drive a metal-oxide/metal reaction, which allows the use of reserves of standard fuel with the advantage of allowing the easy capture of CO_2 [4] [5] [6] [7].

Out of all the metals present in the Earth's crust, iron distinguish itself for its abundance, stability, non toxicity and low cost. Additionally, being one of the first metals ever mastered by humans and by far the most used from that point in time onwards, making its various chemical interactions extremely well understood.

A way of recovering the iron-oxide after the combustion is through hydrogen, that if it is produced using green technologies, like electrolysis or artificial leaves, could then provide not only a green way of recovering the by-product of the metal combustion, but also a way of easily storing the energy of clean hydrogen [8].

Specialized combustors could be used to produce energy through the use of commercially available micron-sized powders (significantly cheaper and easier to produce compared to nanometric powders). Similarities between the physical properties of these powders and pulverized coal implies that they could be used to retro-fit current power generators [9] . This is an advantage, since it reduces the need for new infrastructure and therefore the cost of the energy transition [10].

For now, the biggest obstacle to the production of clean energy through the use of metal fuels is the stabilization of the flame inside of a burner that can capture the combustion products and transfer the heat efficiently [4].

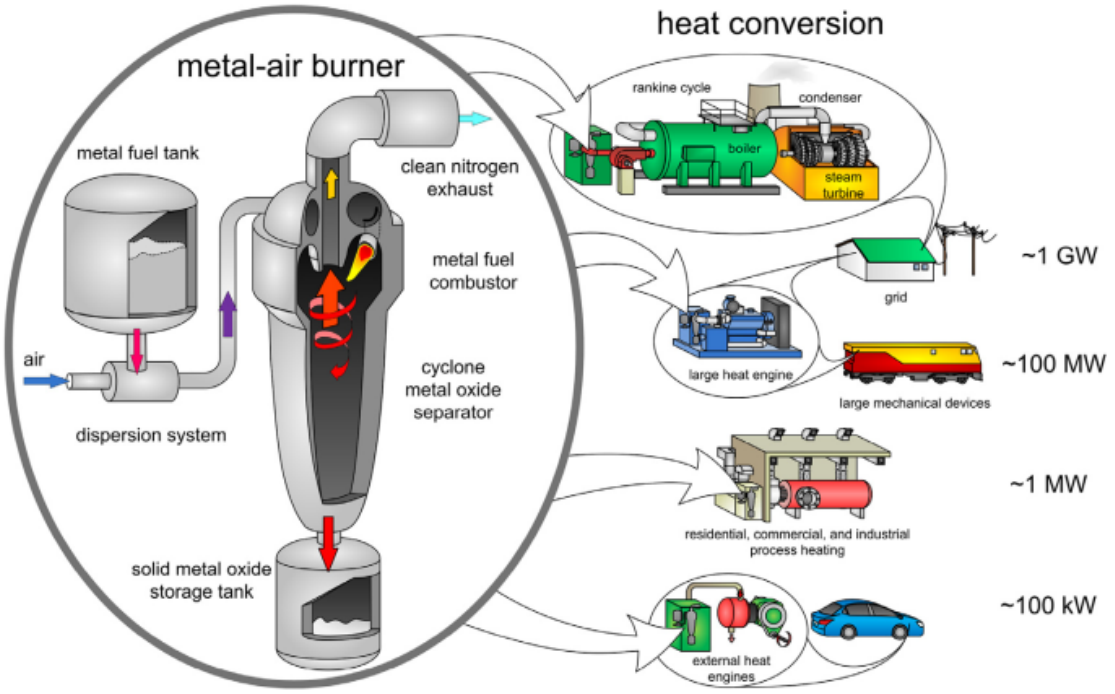


Figure 1.2: Metal combustor and possible applications [4] .

Another key issue that must be solved in order to make this technology suitable for the open market is making the recovery of the oxides not only efficient and cheap enough so that it is economically viable, but also in a form that allows for the direct re-usage of the obtained iron inside of the combustors without too many additional intermediate steps.

1.2 Objectives of the Thesis

The main objective of the thesis is to analyse the fluidizing behaviour and the reduction through hydrogen of iron oxide powders inside of a fluidized bed reactor, within the context of the iron cycle as a potential method for energy storage.

In addition, several iron-oxide powder's properties were studied, in order to characterize their fluidization and reduction behaviour, mass-loss during prolonged fluidization and how the morphology relates to these properties.

The project includes theoretical calculations and data analysis of the behaviour of the furnace and the system as a whole, in order to have a reference for future experiments.

1.3 Thesis Structure

Following this introduction, the second chapter on the theoretical background provides the necessary framework for the study. It explores the mechanisms of iron oxide reduction, the advantages of using hydrogen as a reducing agent, and the fundamental principles governing fluidized bed reactors, including the influence of particle morphology and operating conditions on fluidization.

The materials and methods chapter details the experimental setups and the analytical techniques employed. It describes the cold-bed reactor and the high-temperature furnace, introduces the selected iron-oxide powders, and outlines the methodologies used for particle characterization (such as TGA, BET, XRD, and ICP-OES), along with the theoretical models used for minimum fluidization velocity calculations.

The results chapter presents the data obtained from the experimental campaign. This includes the initial structural and chemical characterization of the raw powders, the outcomes of the cold-bed fluidization tests, and the results from the high-temperature reduction experiments, as well as the post-reaction analyses of the combusted samples.

In the final discussion a critical interpretation of the experimental results is provided. It focuses on the morphological evolution of the particles during reduction, estimates the reduction degrees, and analyses the experimental limitations encountered (namely, fine particle entrainment and post-oxidation) proposing practical solutions to mitigate these issues in future experimental campaigns.

Finally, in the conclusion, the main findings of the thesis are summarized, highlighting the interplay between powder characteristics, fluidization behaviour, and reduction kinetics; and perspectives for future research and optimization of the process are outlined.

2. Theoretical Background

In this chapter the mechanisms for the reduction of iron oxides, and especially in regards to reduction through hydrogen as a cleaner alternative to carbon-based reduction are studied. Afterwards the theory behind fluidized beds and fluidized bed reactor will be explained, and how the influence of the morphology of the powders can influence the fluidization and reduction processes.

2.1 Iron Oxide Reduction

Reduction is the name used to refer to the chemical reactions in which the oxidation state (the hypothetical electric charge of an atom when it forms the maximum number of possible ionic bonds) is modified by the acceptance of electron from another chemical species. In the case of iron, it is a process through which iron oxides are transformed to metallic iron at temperatures lower than the melting point, by removing the oxygen present.

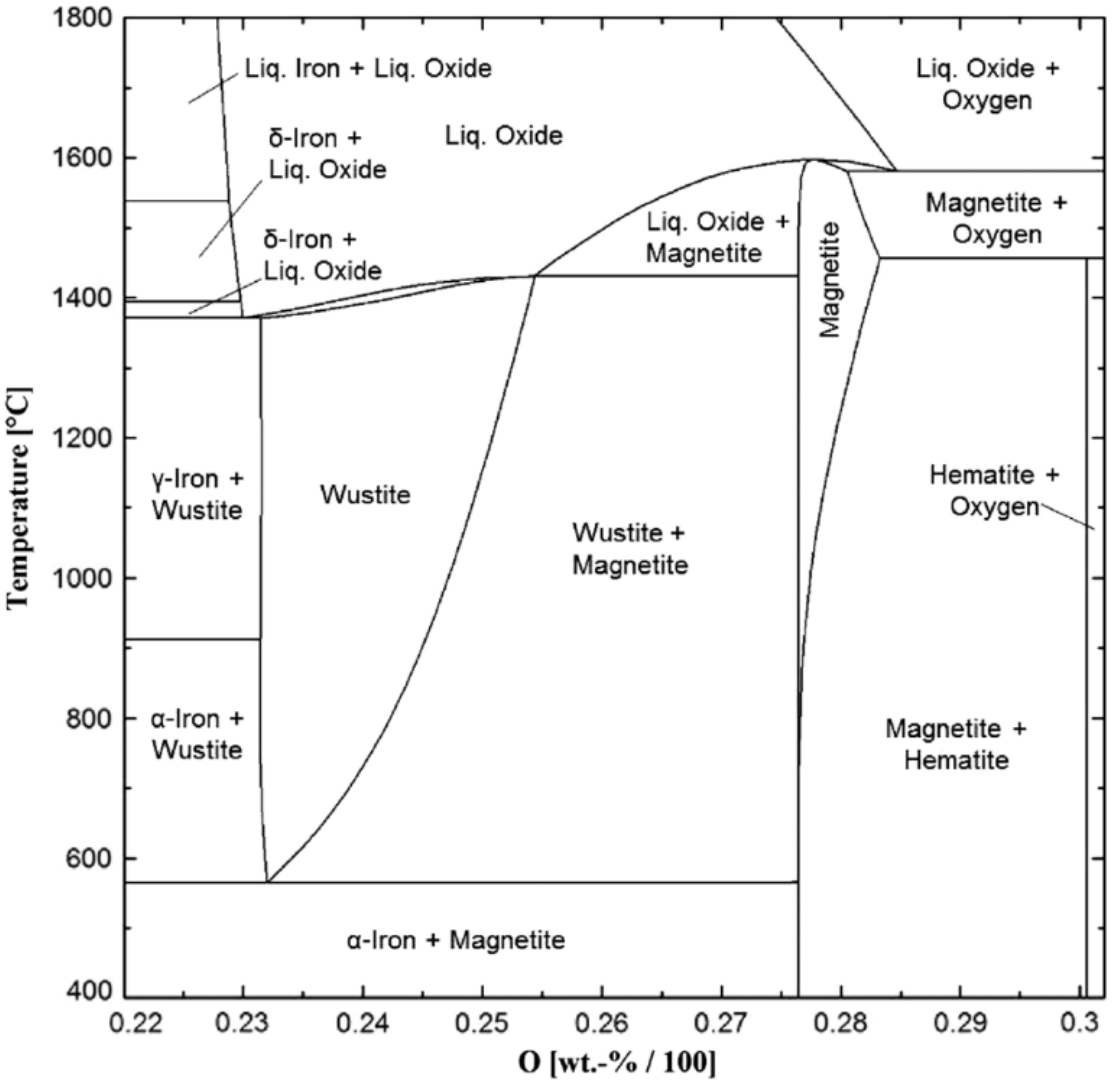


Figure 2.1: Binary Fe-O diagram, from [11]

As it is visible in the diagram, the reduction process crosses different areas of the phase diagram, meaning that it is not a continuous process but it happens in steps. Moreover, the steps themselves depend on the temperature of the reaction, since above 570°C the phase wüstite is also present.

This is done through the use of a reducing agent, usually CO or H_2. The kinetics of the process change based on the reducing agent and on the reaction temperature:

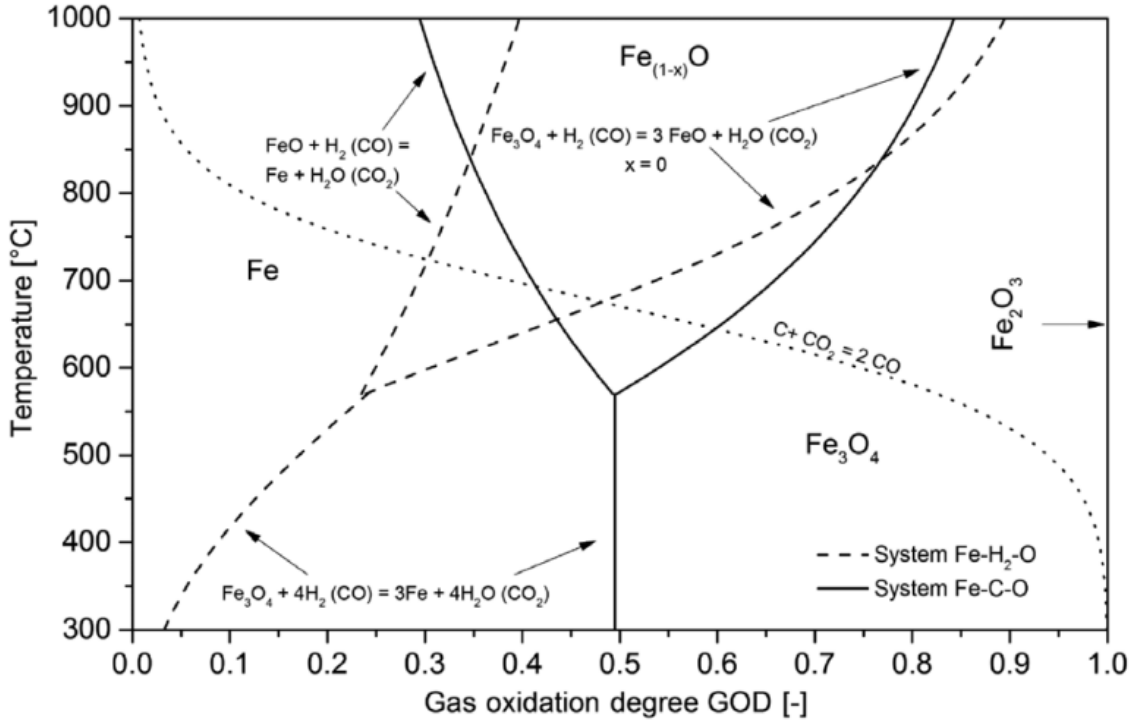


Figure 2.2: Baur-Glässner diagram for the Fe−O−H_2 and Fe−O−C system. [11]

The gas oxidation degree (or GOD) is the ratio of oxidised gas components (in the case of CO and H_2 these are CO_2 or H_2O respectively) over the sum of oxidized and oxidizable gas components:

$$\begin{aligned} GOD_{\mathrm{CO}} &= \frac{\mathrm{CO_2}}{\mathrm{CO} + \mathrm{CO_2}} \\ GOD_{\mathrm{H_2}} &= \frac{\mathrm{H_2O}}{\mathrm{H_2} + \mathrm{H_2O}} \end{aligned} \tag{2.1}$$

It is a good indicator of the reduction force of a gas mixture: if it is close to 1 then it means that the gas is mostly oxidised and so its reductive power is limited, whereas if it is close to 0 it means that most of the gas mixture is available for reducing the iron.

From figure 2.2 we can see that the use of a different reducing agent changes the kinetics of the reaction: the stability area of iron in the Fe−O−C diagram expands at lower temperatures, which means that reduction at a lower temperature leads to a better gas use. Instead, the reduction with hydrogen shows an opposite behaviour, in which the stability area of iron is larger at higher temperatures. Moreover the former reaction is exothermic (it releases heat as the reaction progresses), while the latter is endothermic (heat needs to be added to the system to guarantee a constant reaction temperature).

During reduction of a porous iron ore particle, the following process steps occur:

1. Mass transfer of the gaseous species (reducing gases H_2 and CO) from the gas stream through the laminar layer of the oxide to the interface;

2. Diffusion through macro- and micropores to the oxide interface;
3. Adsorption at the oxide interface;
4. Oxygen removal via phase boundary reaction (formation of H_2O, CO_2, and iron ions;
5. Desorption of gaseous reaction products;
6. Solid-state diffusion of solid reaction products, nucleation, and growth of nuclei;
7. Diffusion of gaseous reaction products back to the laminar layer;
8. Mass transfer of gaseous products through the laminar layer back to the gas stream.

The slowest step in the reaction is what hinders the reduction rate of the oxides, and is therefore called rate-limiting step. Since the parameters that influence the reaction are many, and the reaction itself depends on numerous mechanisms, the influence of various parameters will be discussed in the following sections.

2.1.1 Temperature Influence

The Baur-Glässner diagram shows that, when hydrogen is a reducing agent, the driving force of reduction increases with the temperature. This means that a higher temperature is beneficial for the reaction both in terms of thermodynamics and of kinetics.

Another consideration is that at different temperatures, the type of iron formed through reduction also changes. If a dense iron phase is formed, the reduction rate is limited by the solid-state diffusion, since this phase prevents an optimal contact of the gas phase with the iron oxide interface.

Generally, since the reaction depends on temperature-dependent mechanisms, a higher temperature tends to be preferable. Just like Fick's laws of diffusion the rate of reaction at the surface (as seen in 2.3), and the nucleation and growth of new phases all follow an Arrhenius-type law that depends on the temperature. Another thing to consider is that at lower temperatures the reachable gas utilization may be insufficient due to kinetic limitations, meaning that in order to obtain an acceptable gas utilization (in an industrial perspective) a certain minimum temperature needs to be reached.

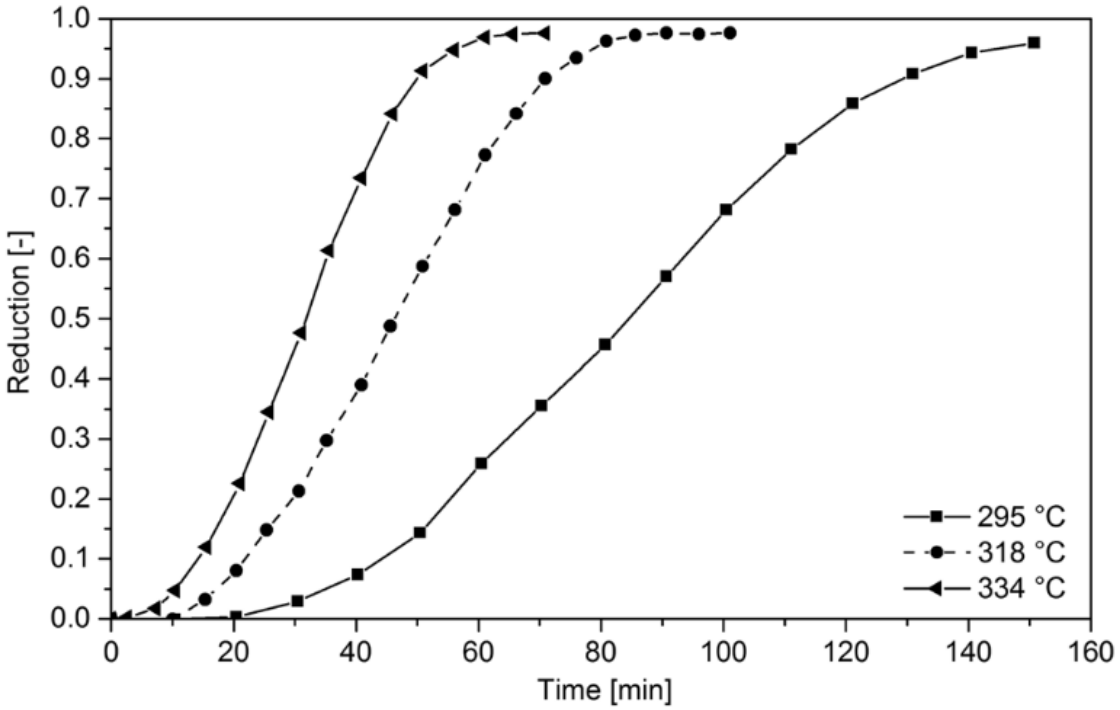


Figure 2.3: Effect of temperature on reduction rate for the reducing wüstite with hydrogen. [11]

2.1.2 Pressure Influence

In the case of the pressure at which the reaction takes place, an important distinction needs to be done: whether the pressure that changes is the total pressure of the gas(es) in the reaction chamber, or only the partial pressure of the reducing gas (H_2 in our case).

Various investigations on the effects of pressure on the reduction rate have been done [12][13],[14], but no clear correlation between pressure and reduction across studies has been found. This could be attributed simply to the fact that the gas velocities and the residence time of the gas in the reactor are not directly comparable.

In general, if the total pressure of the gas mixture is increased, but the partial pressure of hydrogen is kept constant (so at a constant molar flow), no appreciable change in the reaction rate is present at the beginning of the reaction (visible in figure 2.4), but in the final stages of the reaction, the natural decay of the reaction rate can be shifted up to higher reduction degrees (so higher total pressures can shift the natural decay of the reaction to a later time in the reaction itself).

If, on the other hand, we increase both the total and the partial pressure, an increase in the reduction rate is achieved.

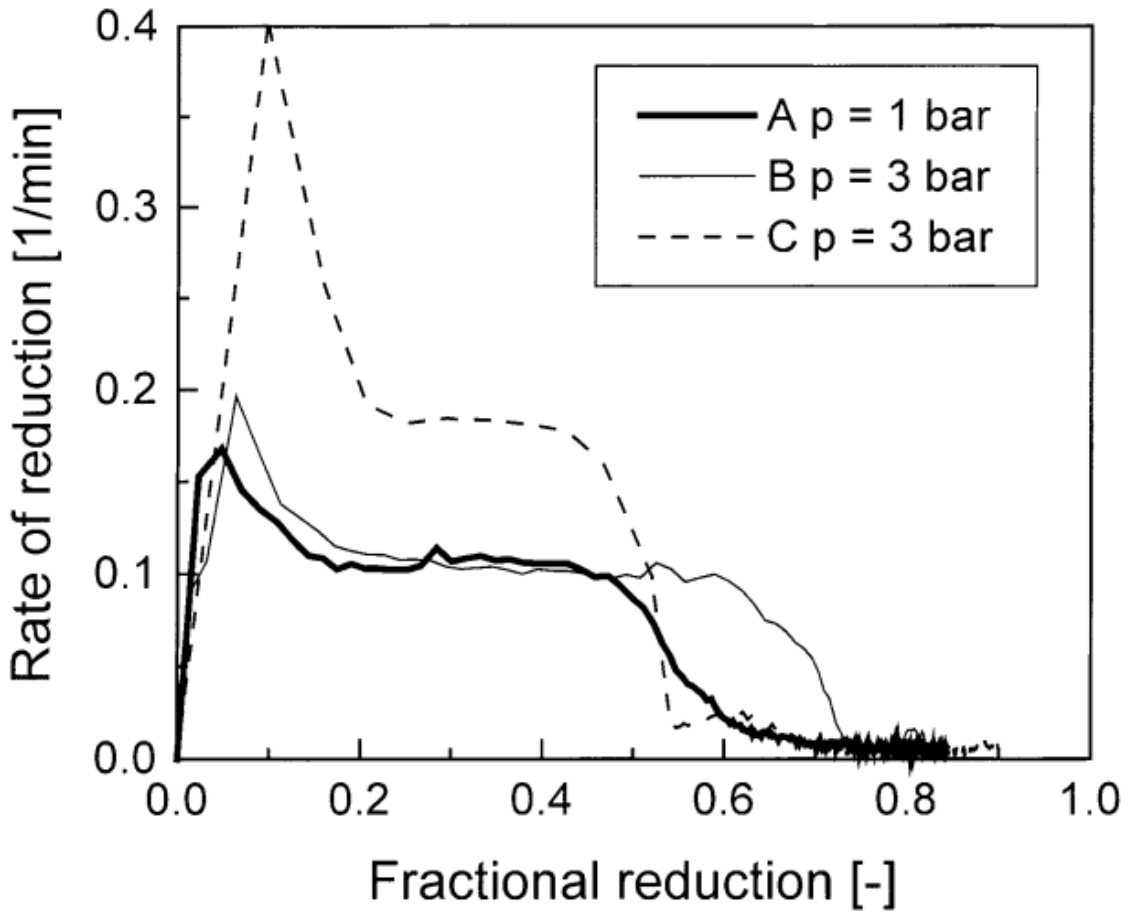


Figure 2.4: Effect of absolute pressure on reduction rate of hematite reduced at 1053 K. [12]

2.1.3 Gas Composition Influence

Again, an important distinction needs to be done: the gas composition can vary based on the gas oxidation degree and on the reducing gas.

In the first case, it is easy to see from figure 2.2 how a lower oxidation degree is better, since the reduction potential is higher (since proportionally more of the gas is available for reduction).

In the second case, using a different gas influences the reaction rate, since the kinetics and the thermodynamical characteristics of the reaction are different for H_2 and CO. At the same temperature, a reaction done with hydrogen as a reducing agent will be faster than one with carbon monoxide (figure 2.5). Moreover, adding H_2 to CO increases the reduction rate (and conversely, adding CO to H_2 slows down the reaction rate). The difference between the behaviour of the two gases is due to the fact that by using hydrogen, the formation of iron nuclei at the interface is facilitated. In addition to that, a reduction done with carbon monoxide shows an initial incubation period, that explains the delay in the first stages of the reaction compared to an hydrogen reaction.

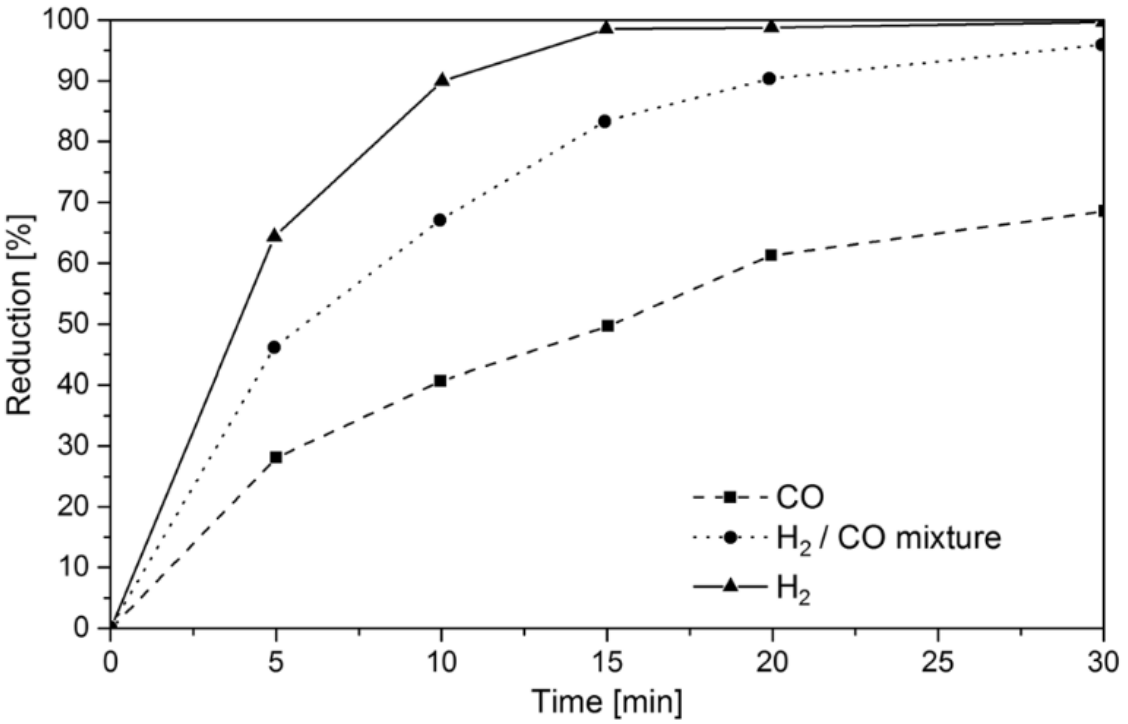


Figure 2.5: Influence of gas composition on the reduction rate of hematite pellets at 850 °C. [11]

2.1.4 Grain Size Influence

Different grain sizes can lead to different rate-limiting steps. The importance of grain size is seen especially at higher temperatures, since at lower temperatures the rate-limiting steps do not depend strongly on the grain size.

From the study of Teplov ([15]), we know that the reduction process is only limited by the removal of the reaction product (namely, water molecules). For smaller particles (<100 μm) this is the major effect, whereas for bigger particles the rate limiting step tends to be the chemical reaction, which is slower.

In general, bigger particles tend to reduce slower than smaller particles (as shown in figure 2.6).

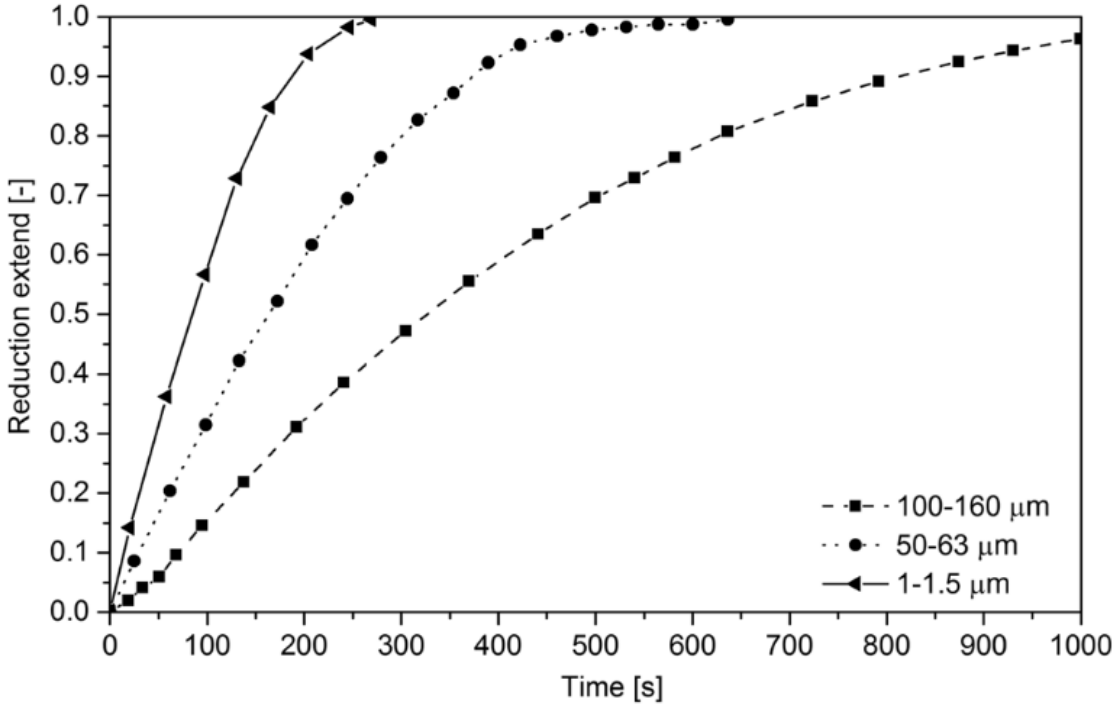


Figure 2.6: Influence of particle size on the reduction rate of magnetite concentrate with hydrogen at 400 °C. [11]

2.1.5 Porosity Influence

A higher porosity in the raw material leads to a faster reduction, since the reducing gas is better able to reach the reaction interface (this because permeability, the ability of a fluid to flow through the media, is higher in a media with higher porosity).

It was also found that macropores are more important for reducibility compared to micropores [11][16]. This is due to the fact that the reduction happens through a phase change, which causes increasing stress and eventually to cracks in the matrix of the porous compact. These cracks allow access to pores that were previously closed, allowing the reducing gases to enter and carry out the reaction. Smaller pores allow the stresses to distribute more evenly, reducing the formation of these cracks and the subsequent spread of the reducing gas.

2.1.6 Mineralogy Influence

Different types of iron ores reduce differently (figure 2.7). This is not only due to the actual material itself, but also due to the fact that oxides during reduction form different structures with different porosities [11], which as we have seen in the previous section is a factor in reducibility.

For example, magnetite typically shows a non-porous structure that forms a dense iron layers around the particle during reduction.

As we have seen in 2.1 wüstite has a structure that, through vacancies, allows for a better transfer of iron ions to the surface of the particle, it may cause a thick layer of pure iron to form at the gas-metal interface. This causes further reduction to happen through solid-state diffusion of the oxygen atoms through the iron layer, resulting in

a lower reduction rate (since the diffusion coefficient in this instance is much lower compared to the normal gaseous diffusion).

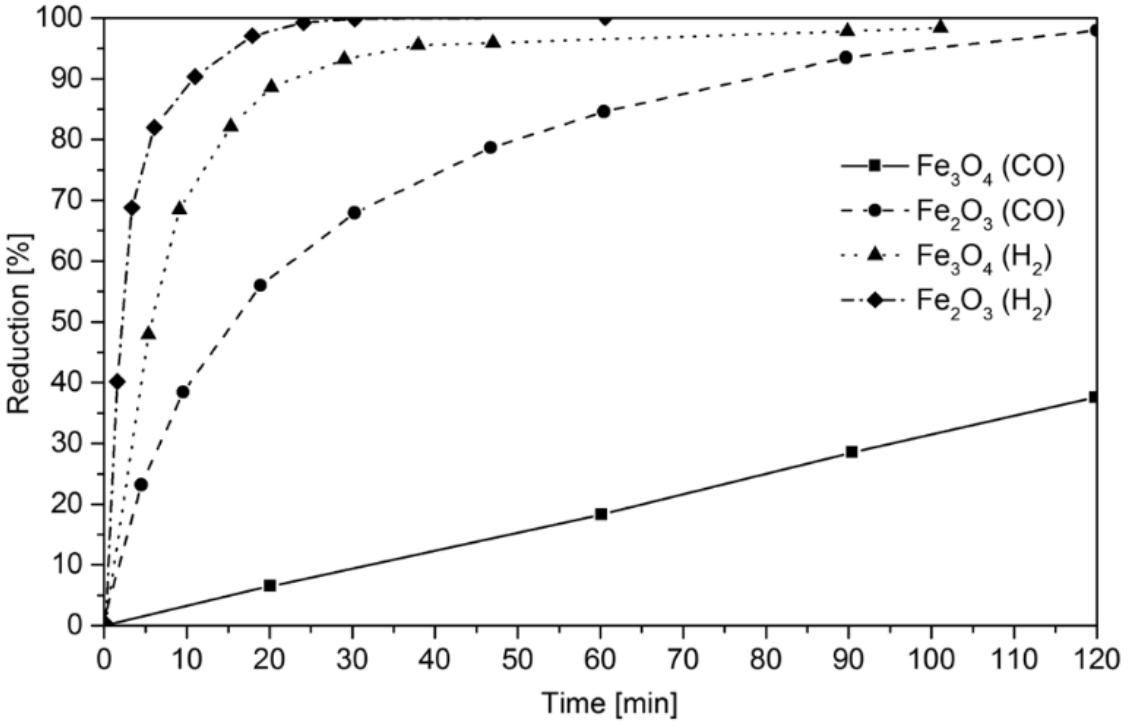


Figure 2.7: Effect of mineralogy on the reduction rate with hydrogen and carbon monoxide.[11]

2.1.7 Gangue Influence

Gangue is defined as ”the commercially worthless material that surrounds, or is closely mixed with, a wanted mineral in an ore deposit” [17].

Research shows that the reduction rate is independent on the amount of silica SiO_2, whereas having some calcium oxide CaO (also known as quicklime) positively impacts the reduction rate. In addition to this, it was also shown how magnesia MgO lowers the reducibility of a sample.

Another important gangue element is alumina Al_2O_3, which, if present, results in a ”network-like wüstite structure” [11], which causes iron to form along it as the reduction progresses, eliminating the aforementioned effect of a dense iron layer, therefore increasing the reduction rate (which can be seen in figure 2.8).

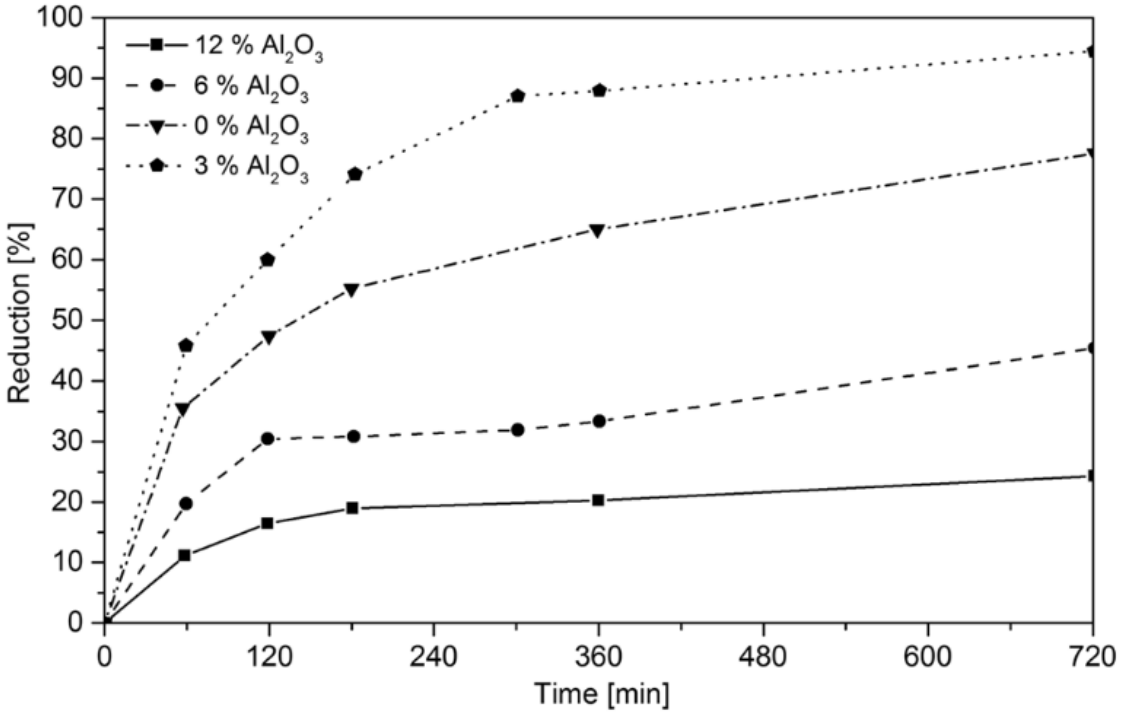


Figure 2.8: Effect of Al_2O_3 doping amount on the reduction rate of magnetite at 750 °C. [11]

2.1.8 Gas Flow Rate Influence

The effective availability of the reducing gas for the reaction can be controlled not only by its partial pressure but also by maintaining a continuous flow of gas through the reaction chamber. This approach not only prevents the progressive decline in reaction rate due to the gas consumption, but also allows for a higher thermodynamic driving force without the need to raise the system pressure to potentially unsafe levels.

The effect of gas flow rate on the reduction process has been investigated, revealing diminishing returns at higher flow rates (as denoted by the closeness of the curves for 9.3 and 12.4 $g \cdot mol/cm^2hr$ in figure 2.9). This indicates that the reaction rate cannot be increased indefinitely, as it is ultimately limited by kinetic and transport constraints.

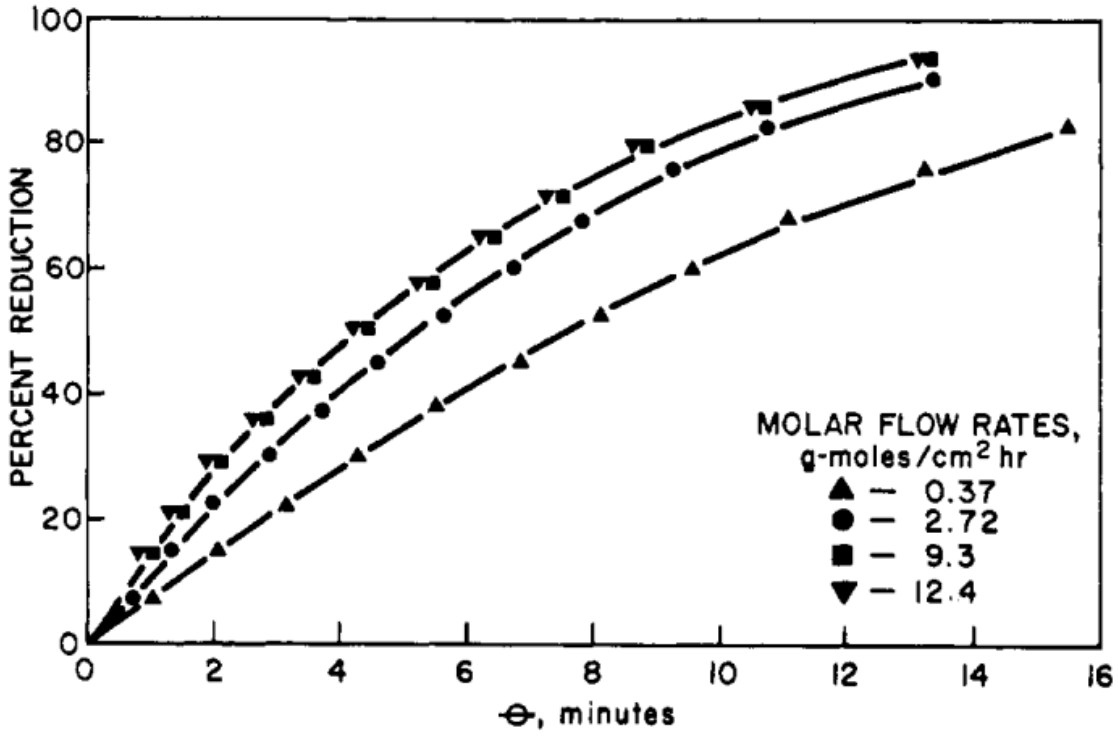


Figure 2. Effect of flow rate on reduction curves at 927° C.

Figure 2.9: Effect of flow rate on reduction curves at 927 °C. [18]

This asymptote is present at all temperatures, and is itself proportional to the reaction temperature. The reduction rate k in grams of oxide per square centimeter per minute (g/cm^2/min), is defined as:

$$r_0 d_0[1 - (1 - R)^{1/3}] = kt \tag{2.2}$$

where r_0 denotes the pellet radius in centimeters, d_0 the pellet density in grams per cubic centimeter, R the fractional reduction, and t the time in minutes.

This reduction rate is used to characterise how the reaction progresses at various temperatures (it gives an idea on the kinetics of the reaction). As we can see in figure 2.10, the reaction rate slows down at higher molar flow rates of H_2, at the asymptote increases with temperature:

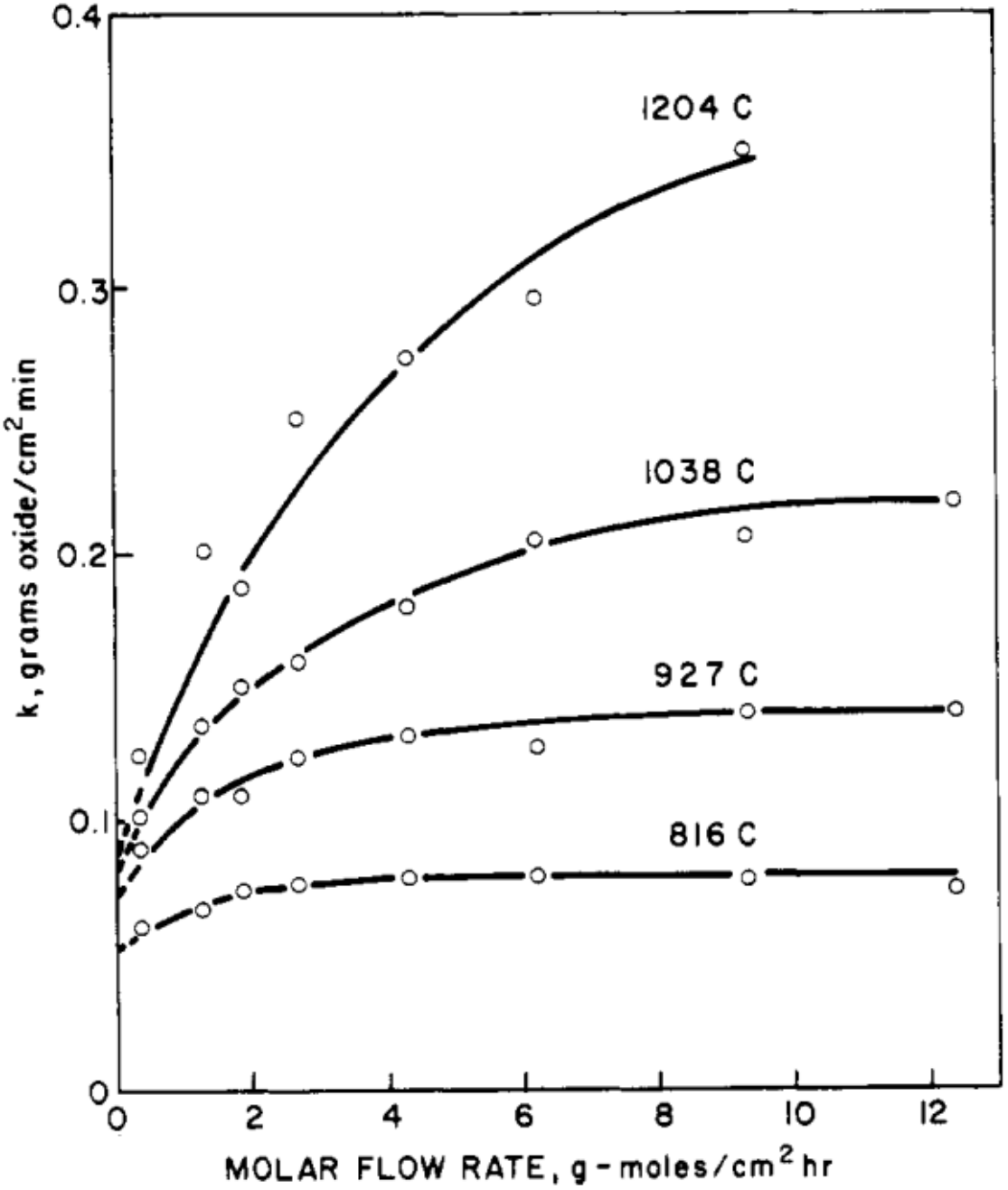


Figure 2.10: Effect of molar flow rate on reduction rate constant, k [18].

2.1.9 Gas Residence Time Influence

As we have previously discussed, the availability of the gas for the reaction is a very important parameter. A way of characterising this factor is the residence time of the gas, or the time that a fluid parcel spends inside of a control volume, in our case how much time a molecule spends inside of the reactor. If a molecule spends too little time inside of the reactor, it has a lower probability of reacting, which causes incomplete reactions and reduced H_2 consumption (which might cause an increase in costs if the unreacted hydrogen is not recycled back into the chamber and is therefore wasted) [19].

This effect gives a practical limit to how much we can increase the flow gas rate and the pressure inside of the chamber, since after a certain point both of these reduce the residence time of the gas inside of the chamber.

2.2 Hydrogen as a Reducing Agent

There are two main reducing agents used in the reduction process of iron oxides: hydrogen (H_2) and carbon monoxide (CO). Results show that reduction in a CO atmosphere takes more time (visible in figure 2.11) compared with H_2 due to better effective gas diffusivities of $H_2 - H_2O$.

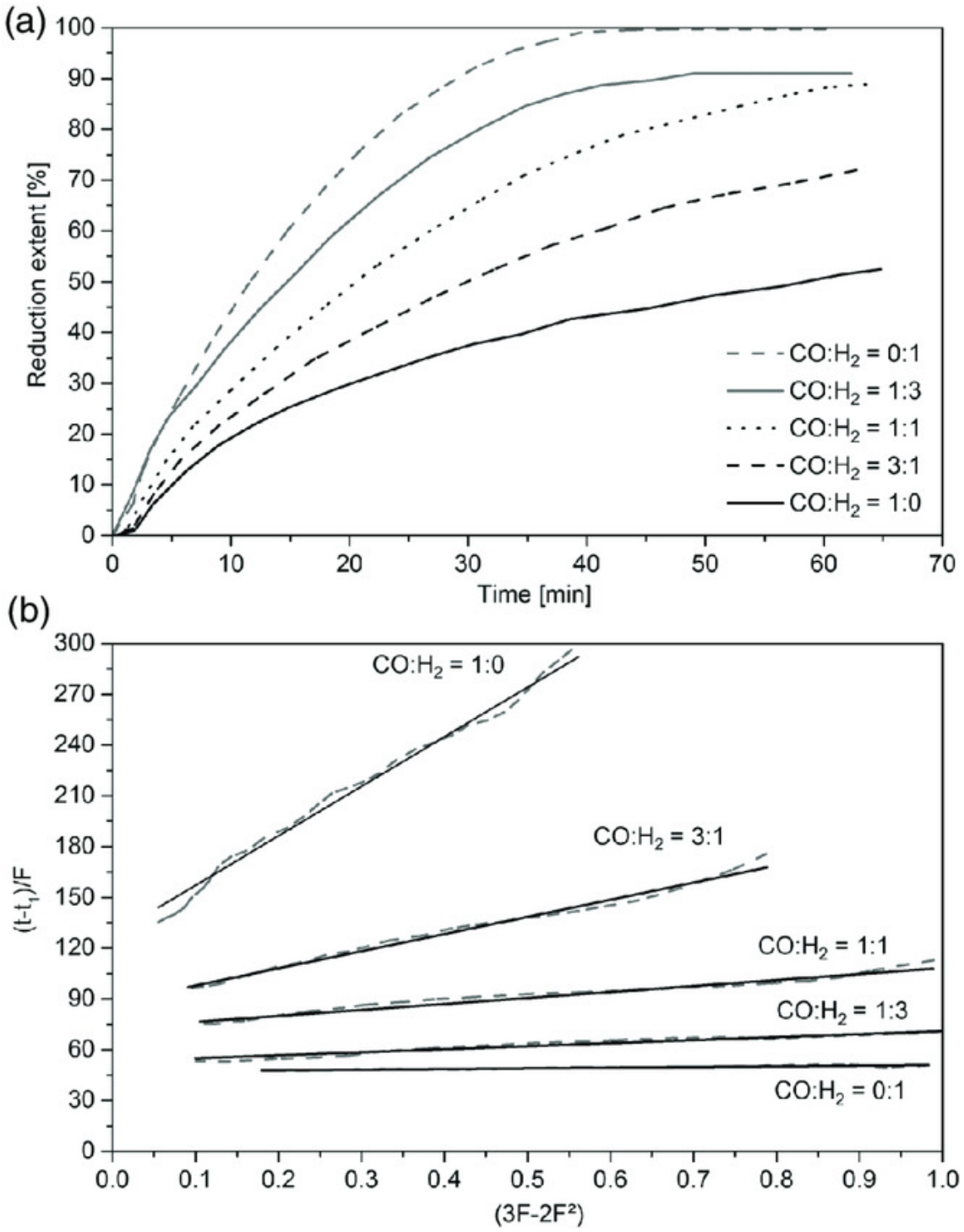


Figure 2.11: a) Progress of reduction over time for different gas mixtures and b) Procedure for determining the effective diffusion coefficient [11][20].

This effect happens because the diffusivity of hydrogen is much better than that of carbon monoxide (0.756 cm^2/s for the former compared to the 0.16 of the latter, at 20°C and atmospheric pressure [21]), which allows the former to reach the reaction sites easier compared to the latter, irrespective of the driving force, since the diffusion-controlled kinetics dominate [11].

Another effect is that, with increasing amount of CO gas not only the diffusivity of the mixture decreases, but the bigger carbon monoxide molecules block the diffusion paths of the H_2 molecules, further hindering the reaction [11].

Thus, we are mainly interested in reduction with hydrogen, not only because of its superior reducing capabilities, but also because it generates only water as a reaction product and can be obtained from renewable energy sources, making it the better choice for a green industrial process.

In this case the reduction reaction is represented by the following equations:

$$\begin{gathered} 3Fe_2O_3 + H_2 \rightarrow 2Fe_3O_4 + H_2O \\ T < 570°C \\ Fe_3O_4 + 4H_2 \rightarrow 3Fe + 4H_2O \\ T > 570°C \\ (1-x)Fe_3O_4 + (1-4x)H_2 \rightarrow 3Fe_{(1-x)}O + (1-4x)H_2O \\ Fe_{(1-x)}O + H_2 \rightarrow (1-x)Fe + H_2O \end{gathered} \tag{2.3}$$

With increasing temperature, the stability area of wüstite expands because not all places in the lattice are occupied by iron ions. Therefore, the formula for wüstite is written as Fe(1-x)O instead of FeO, where $(1-x)$ represents vacancies in the iron lattice.

The typical hydrogen reduction profiles present a two-stage reductions, which has been shown by various researchers:

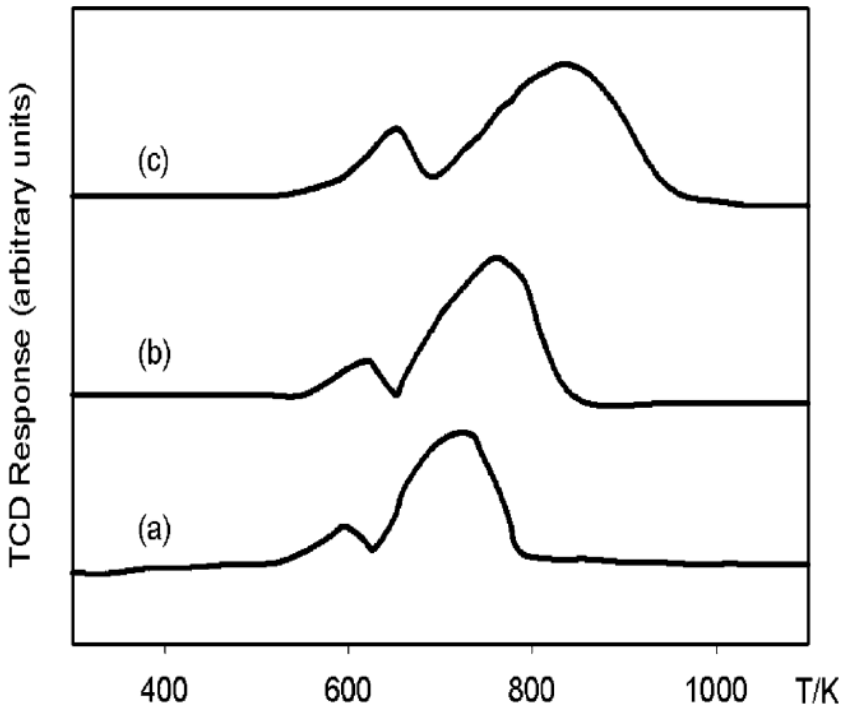


Figure 2.12: Temperature programmed reduction (TPR) patterns of different heating rates: (a) = 3 K/min, (b) = 7 K/min, (c) = 21 K/min [22].

As is visible in figure 2.12, there is a peak at about 570 °C in all of the graph, due to the reaction from Fe_2O_3 to Fe_3O_4, whereas the second peaks are due to the reduction of Fe_3O_4 to metallic iron. According to the second equation in (2.3) this second peak should have an area 8 times that of the first one [22] if the reduction is completed. This can be used to determine whether one of the two reduction steps is incomplete.

Since hydrogen based reduction is endothermic in nature, using it for reduction increases the energy demand of the process, already incredibly energy intensive (when natural gas is used, the reaction requires over than 18 GJ of energy per tonne of iron produced [23]). This is the main reason for the current use of exothermic chemical reactions in industrial reduction processes.

2.2.1 Kinetic Mechanisms

Having a kinetic model that accurately describes the reduction reaction is crucial for being able to understand and predict the reduction behaviour of iron.

Various models have been developed through the years [24]:

- The apparent model: it is a simple model, and therefore could not take into account various processes like gas and solid diffusion or structural changes;
- The shrinking core model: it is more advanced compared to the apparent model, but it still does not take porosity or its changes throughout the reaction into account;
- The grain model [25]: it is an evolution of the previous model. It considers the effects of pore structure by assuming that particles are composed of numerous spherical grains with pores between them. Gas molecules diffuse along these pores to reach the grain surface and participate in chemical reactions, with each grain described by the shrinking core model;
- The random pore model [26][27]: it also considers randomly distributed and overlapping pore structures within the particle. Gas molecules diffuse through these pores to react with the solid reactant, forming a solid product that gradually covers the pore surfaces during the reaction process.

These models assume that the solid product forms a continuous layer uniformly covering the solid reactant surface during the gas-solid reactions, when in reality they grow in discrete and separated structures (as depicted in figure 2.13):

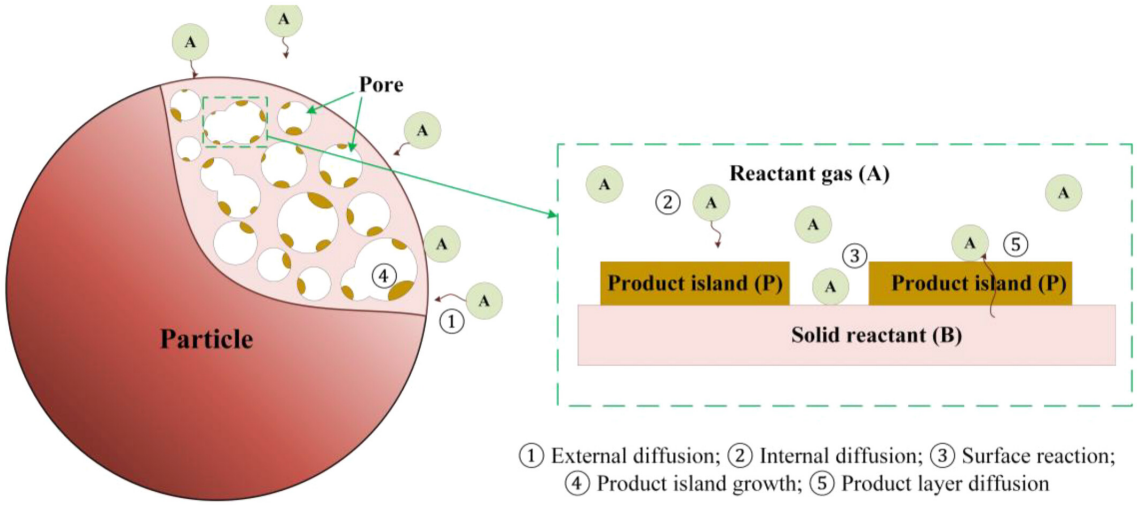


Figure 2.13: Physical and chemical processes during redox reactions [24].

The gas-solid reaction of porous particles follows the following steps (also illustrated in figure 2.14):

1. Chemical reaction, product island growth, and product layer diffusion on the interface between the solid reactant and pore;
2. Internal diffusion of reacting gas within the particle;
3. External diffusion of reacting gas to the particle outer surface.

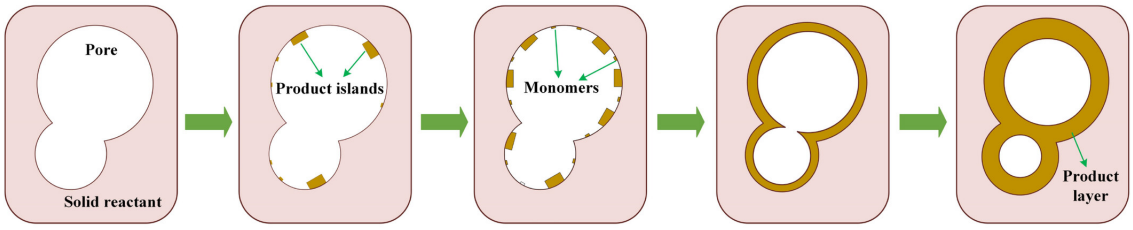


Figure 2.14: Change of pore structure during reaction process [24].

2.2.2 Environmental Aspects

While hydrogen may need more energy in order to conduct the reduction reaction, it would also prevent the emissions of many tonnes of CO_2 (producing steel through a blast furnace emits approximately 1870 $kgCO_2/tls$ (kilograms of CO_2 per tonne of liquid steel)).

Moreover, since hydrogen has application in various other sectors (chemical production, aviation, etc.), catering to the demands for hydrogen for one industry would allow to reduce the costs for all other industries that use it, thanks to economy of scale mechanisms.

In total the use of green hydrogen in the iron and steel sector, has the potential to reduce emissions by 2.3 GtCO2/y globally [28].

It is evident therefore that achieving industrial-scale production of green hydrogen is key for the development of processes that use it in order to reduce iron oxides.

2.3 Fluidized Bed Reactors

Fluidization is the process through which finely divided solid particles acquire fluid-like behaviour when brought into contact with a gas, a liquid, or a combination of the two [29]. In the remainder of this chapter, only gas-solid fluidization will be considered, even though many types of fluidized bed reactors exist, as seen in figure 2.15.

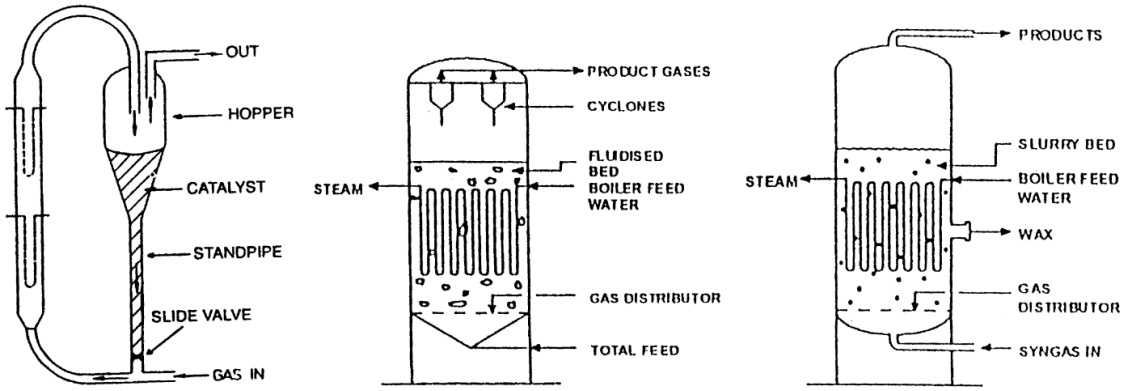


Figure 2.15: Three types of fluidized bed reactors [30].

Since its invention in 1921 for the gasification of coal, the fluidized bed has found application in a wide range of processes that require efficient mixing and heat transfer, such as chemical production, gasification, combustion and oxidation reactions, and pyrolysis. However, the terms ”fluidization” and ”fluid bed” did not emerge until about 1940 when researchers in the United States developed gas-supported beds for catalytic cracking of heavy hydrocarbons.

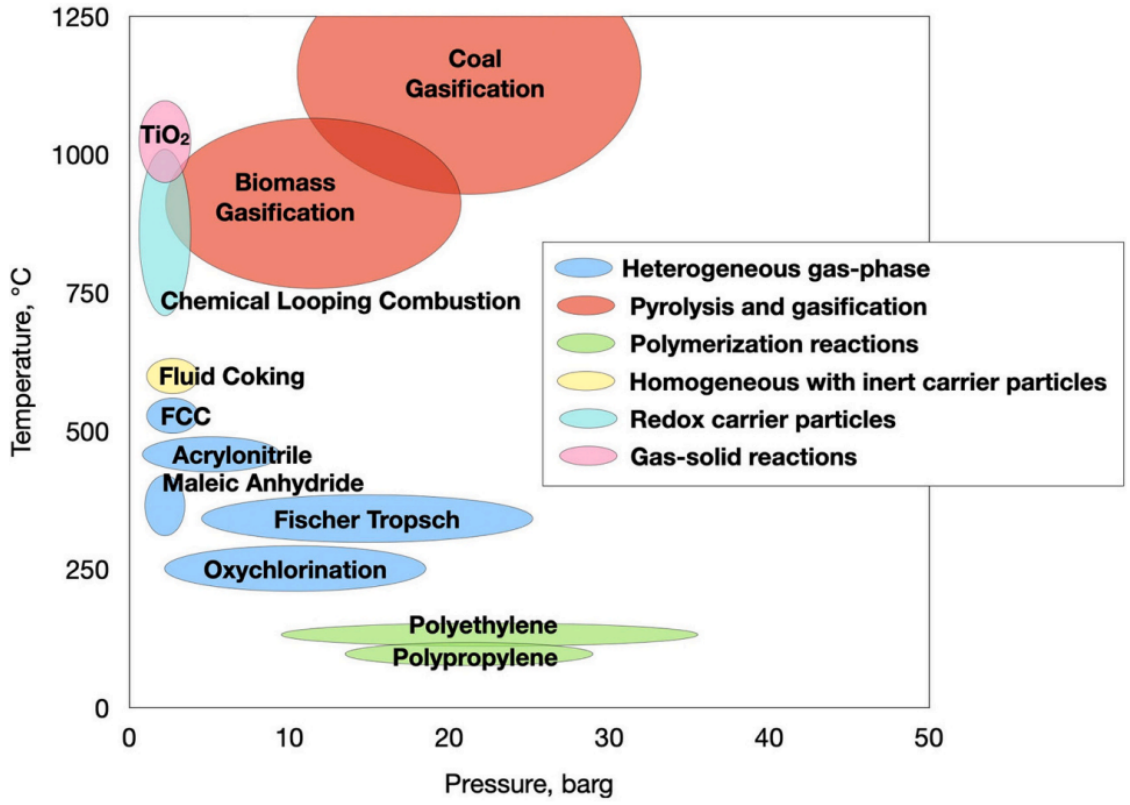


Figure 2.16: Some industrial fluidized bed and circulating fluidized bed processes [31].

Modern applications (summarised in figure 2.16) of this technique include the production of carbon nanotubes [32], the manufacture of a significant portion of the silicon used in solar cells [31], and chemical looping combustion [31], which is closely related to the subject of this thesis.

For clarity and completeness, several key terms commonly encountered in gas-solid fluidization are briefly defined below. While not all of these are directly employed in the present thesis, they are key to understanding the principles of fluidization and its related phenomena:

- Agglomeration: Particles sticking together to form assemblies (agglomerates);
- Bed expansion: Height of operating fluidized bed divided by static bed height or bed height at minimum fluidization;
- Elutriation: Progressive selective removal of finer particulates by entrainment; Freeboard: Region extending from dense fluidised bed upper surface to top of vessel;
- Superficial velocity: Volumetric flow rate of fluid divided by total column cross-sectional area.

Fluidized beds are employed in a wide variety of applications due to several advantageous characteristics, including:

- Fluidized solids can be easily transferred between reactors;
- The intense internal mixing that occurs within a fluidized bed produces an essentially uniform temperature throughout the system;
- This same mixing also promotes a homogeneous distribution of chemical reactants when the bed is used as a reaction medium;
- The heat transfer between a fluidized bed and heat exchangers immersed within it is significantly enhanced;
- Relatively low pressure drops: only enough to support the bed weight per unit of cross-sectional area;
- Scalable to very large sizes: some industrial beds reach diameters in the order of meters [33];
- Wide particle size distributions: ratios of upper to lower decile particle diameter, d_{p90}/d_{p10} , of 10:20 [33].

However, fluidised bed also have some intrinsic disadvantages:

- Vertical mixing of gas: the gas is dragged downwards by descending particles resulting in "backmixing";
- Vertical dispersion of solids: because of the motion of the particles, some of them end up spending very little time inside of the bed, while others spend much longer than the mean residence time;
- Gas bypass: gas in a lower-density phase (like that in bubbles), passes through the bed more quickly and with less access to particles than gas associated in a denser phase in which there is better gas-solid contact;
- Limitations on particle fluidization: particles of weird shapes, or smaller than about 30 μm in mean diameter are difficult, or even impossible, to fluidise [33];
- Entrainment: particles, especially fine ones, are carried upwards by the exhaust or product gas and leave the column through the exit;
- Attrition: particles can break or be abraded when they collide/interact with each other and with fixed surfaces;
- Wear on surfaces: particle motion causes erosion/wastage of fixed surfaces;
- Complexity: fluidized beds are more complex to design, operate, and model than fixed bed reactors.

When a stream of gas flows upward through a bed of particles, it exerts a drag force on them. As the velocity of the gas increases, this drag force becomes increasingly significant. When it eventually balances the gravitational force acting on the particles, their weight is effectively supported by the gas. At this point, the particles become suspended, and the bed is said to be fluidized. The corresponding gas velocity is

known as the minimum fluidization velocity. Below this velocity, the drag force is insufficient to overcome gravity, and the bed remains stationary in a fixed or packed state.

A typical fluidized bed, as figure 2.17 displays, consists of a gas distributor, often a grid plate, positioned at the bottom of the column. The function of this plate is to act as a diffuser, ensuring that the gas flow entering the system is evenly distributed across the cross-section of the bed. Above the distributor lies the powder bed, also referred to as the dense phase, which contains the majority of the solid particles. Over the upper surface of this dense phase develops the dilute phase, an aerosol composed of particles entrained and carried by the fluidizing gas. In many setups, a cyclone separator is installed above the dilute phase to capture and recover these entrained particles.

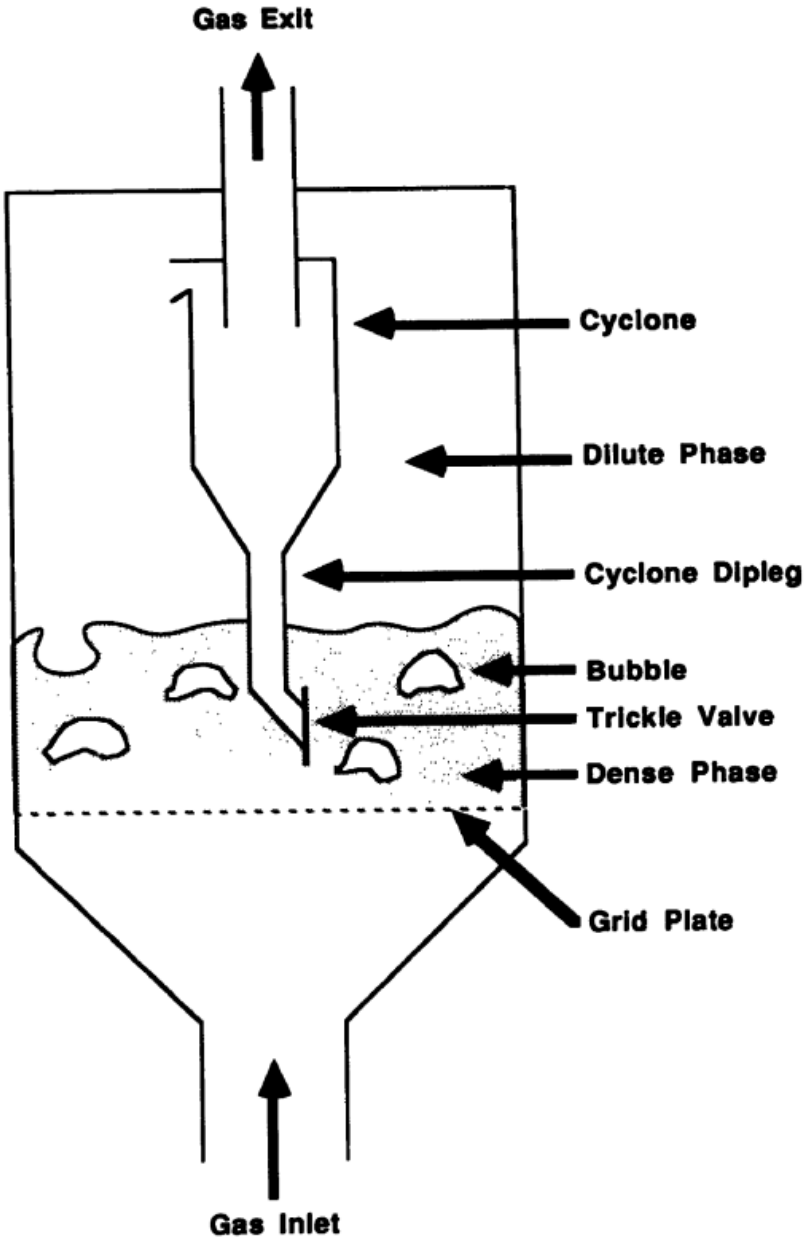


Figure 2.17: Typical bubbling gas-solid fluidized bed [29].

The gas velocity used to describe fluidized systems is usually called the superficial velocity, which is the velocity calculated on the basis of the empty cross-section of the column, measured at the surface of the dense phase. As this superficial velocity is gradually increased, the bed passes through a series of distinct flow regimes, each characterized by different patterns of gas-solid interaction. These regimes are schematically represented in figure 2.18.

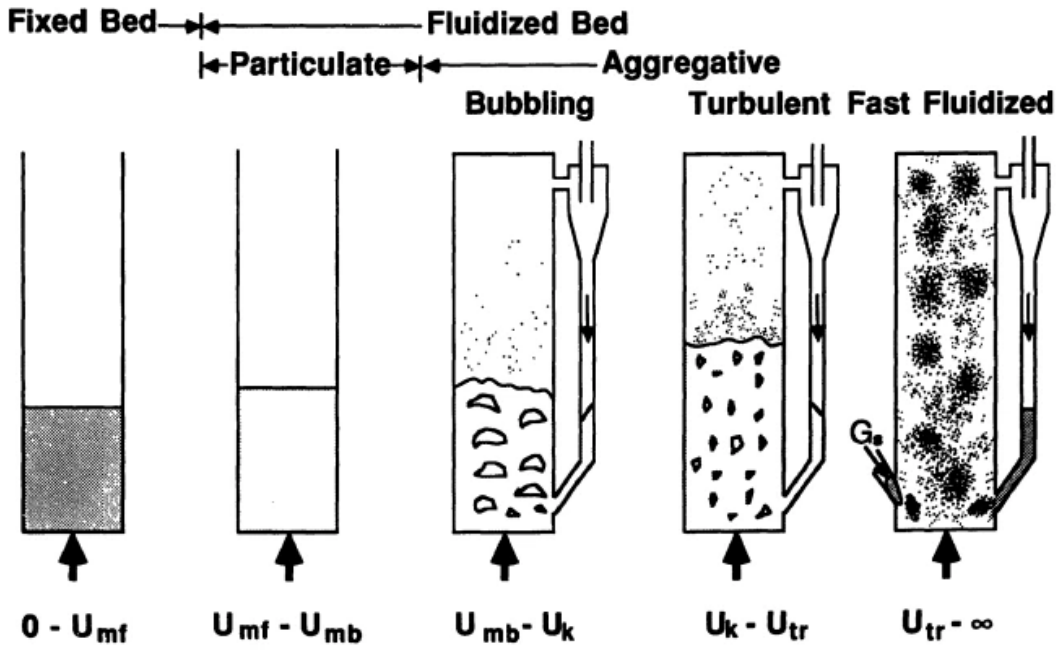


Figure 1-2: Schematic Diagram depicting five different regimes of gas-solid fluidization

Figure 2.18: The five different regimes of fluidization [29]. In this figure U_{mf} is the minimum fluidization velocity, U_{mb} is the minimum bubbling velocity, U_k is the velocity at which the system transitions to a turbulent bed regime, and U_{tr} is the transport velocity (the velocity at which all particles can be transported out of the fluidized bed by gas).

Further increasing the gas flow rate beyond the minimum fluidization velocity enhances the fluid-like behaviour of the bed. The particles move more freely, and the system becomes increasingly dynamic, until eventually the particles no longer form a coherent bed and are instead entrained and transported by the gas stream.

After reaching the minimum fluidization velocity, at which the bed begins to exhibit fluid-like behaviour, fine particle systems start to display the formation of bubbles once the minimum bubbling velocity, u_{mb}, is attained. As the gas velocity increases further, slugs begin to form at the minimum slugging velocity, u_{ms}.

The transition from this bubbling or slugging behaviour to the turbulent fluidization regime is generally assumed to occur when the superficial velocity, u, reaches u_c, the velocity at which the standard deviation of pressure fluctuations attains a maximum value [34].

Finally, the entrainment velocity, u_e, defines the upper operational limit of a fluidized bed reactor. Beyond this point, particles can no longer be retained within the column unless the entrained solids are effectively captured and returned to the bed.

To characterize these different regimes, flow regime maps like the one in figure 2.19 are typically employed. These maps correlate particle diameter and gas velocity, or their dimensionless equivalents, with the corresponding flow regimes.

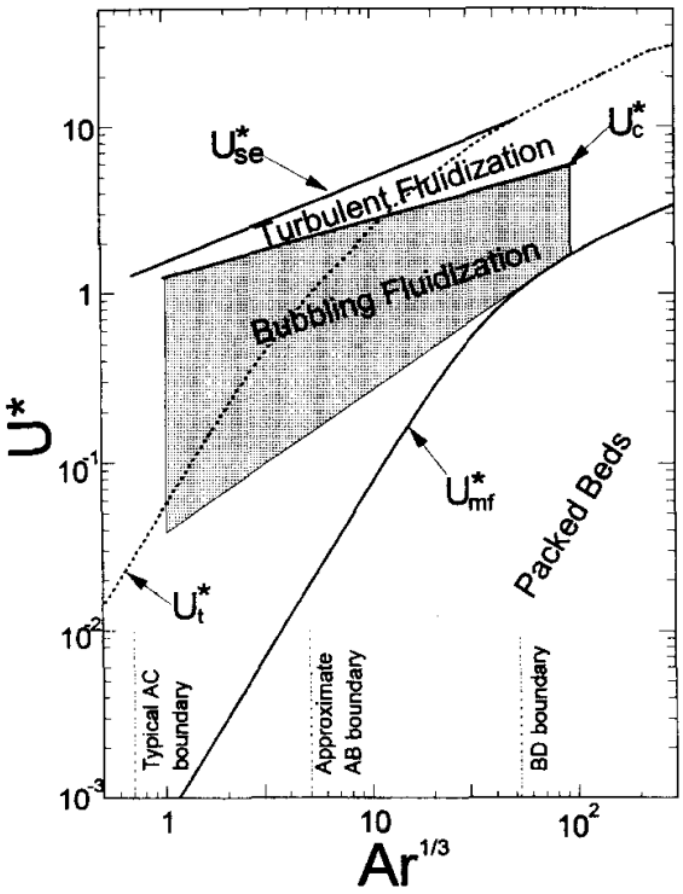


Figure 2.19: Flow regime map for gas-solids fluidization. Heavy lines indicate transition velocities, while the shaded region bounded by thin lines is the typical operating range of bubbling fluidized beds [34].

In figure 2.19 the axes are represented by the dimensionless parameters

$$U^* = \frac{Re}{Ar^{1/3}} \qquad \text{and} \qquad d_p^* = Ar^{1/3} \tag{2.4}$$

with Re the Reynolds number and Ar the Archimedes number.

Geldart [35][36] proposed a widely used and practical classification system that divides particulate materials into four groups according to their gas-solid fluidization behaviour. In his second paper on the subject [36], groups C and D were added to extend the classification to smaller and larger particles, respectively, than those originally included in Groups A and B in his first publication [35] and as a result, when the four groups are ordered by increasing particle size, they do not follow alphabetical order.

Their characteristics are:

- Group C (cohesive): these powders are dominated by interparticle cohesive forces, which prevent them from fluidizing readily. Instead, they tend to form fissures through which the gas preferentially passes. A common example of a Group C powder is cooking flour;
- Group A (aeratable): interparticle forces are less significant than in Group C materials. As the upward gas velocity increases and becomes sufficient to fluidize the bed, the particles expand smoothly, initially without bubble formation [37]. Upon further increase in gas velocity, a minimum bubbling velocity, u_{mb}, is reached. A typical example of a Group A powder is fluid catalytic cracking (FCC) catalyst;
- Group B (bubbling readily): in this group, interparticle forces are negligible, and bubbles form immediately once the superficial gas velocity exceeds the minimum fluidization velocity. Fluidization is generally good, although Group A powders typically exhibit superior fluidization behaviour. Sand is a representative example of this group;
- Group D: these powders consist of coarser particles that can be fluidized, but less smoothly and less uniformly than Groups A and B. Examples include cereal grains and peas.

Although these four groups are presented as distinct categories (and also depicted as such, like in figure 2.20), the boundaries between them are not sharply defined, and the transitions from one group to another occur gradually.

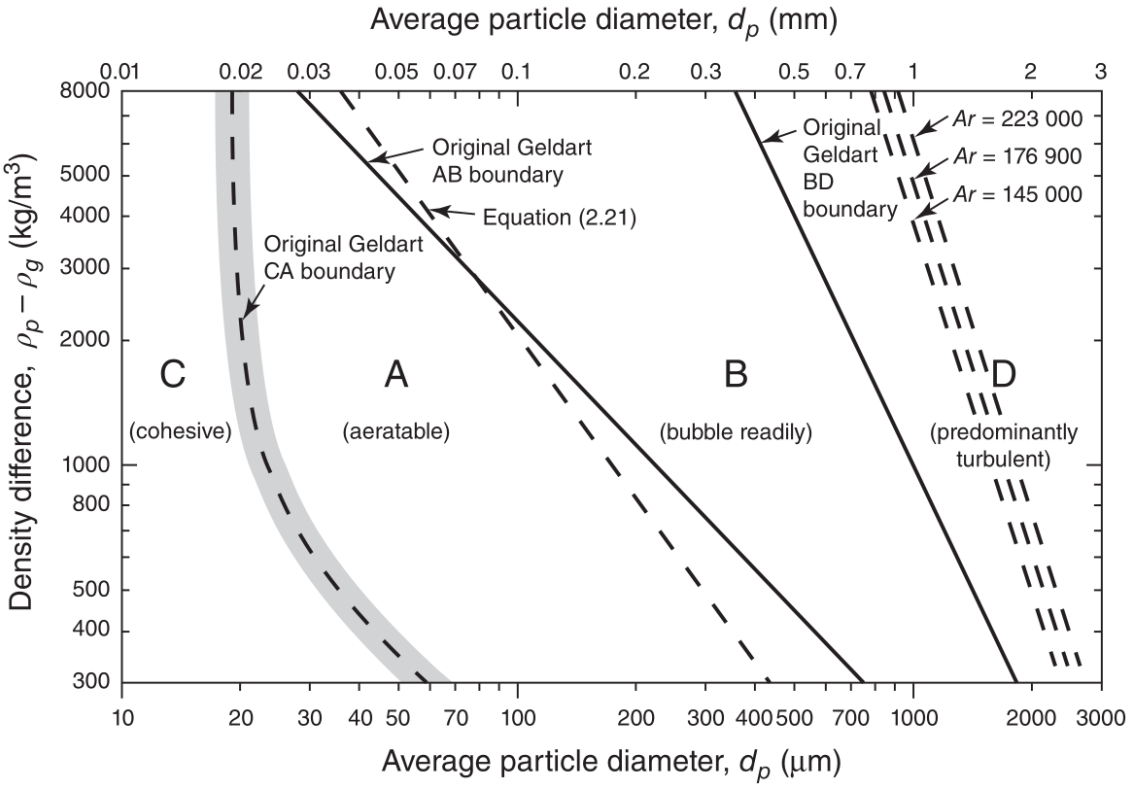


Figure 2.20: Geldart powder classification group boundaries for fluidization in air at 20 °C and 1 atm pressure [36] [37].

Due to their complex flow patterns and the large number of interacting factors, fluidized beds are challenging systems to model accurately. Therefore, it is essential to characterize their key properties in order to develop a proper understanding of the underlying processes. In the following sections, the influence of various parameters on the fluidization behaviour of the system is examined.

2.3.1 Gas Properties Influence

As previously stated, it is the drag force of the gas on the particles that enables fluidization, and the two main gas properties that influence it are density and viscosity.

Higher densities (caused not only by different gas mixtures, but also by increased pressures or lower temperatures) lead to earlier (in terms of gas flow speeds) and more vigorous fluidization. Ideal gas behaviour can usually be assumed as a good approximation when assessing the roles of temperature and pressure on gas-fluidized beds [37].

On the other hand, when the viscosity of the gas increases (which is almost independent of pressure and can again vary due to higher temperature or different gases), the drag on small particles increases, while the effect on larger particles is limited [37].

Humidity (the water vapour content of the gas) and adsorptivity (the presence of gaseous components that adsorb on the surface of particles) also influence the fluidization behaviour of a system, but as relevant to the case studied in this work,

since the first is basically non-existent in the high-temperature ambient of the furnace, and the second only affects the interactions between particles mediated by van der Waals forces, which are negligible compared to the other effects.

2.3.2 Bulk Particle Properties Influence

While the previous section focused on the properties of individual particles, the behaviour of a powder bed is also strongly influenced by the collective, or bulk, properties of the material. Parameters such as bulk density, flowability, compressibility, and porosity determine how the powder behaves as an ensemble in a fluidized bed.

2.3.2.1 Mean Size Characteristics

A number of techniques are available to determine particle size distributions, the most common of which is sieve analysis. This method is particularly used to quantify the amount of fines, defined as the proportion of particles (by mass) that pass through the finest standard sieve, typically corresponding to sizes below approximately 37 μm.

These fine particles play a particularly important role in determining the fluidization behaviour of gas-solid fluidized beds. When a substantial fraction of the material consists of particles smaller than about 40 μm, alternative characterization methods can be employed, such as Coulter counters or Malvern Mastersizers.

2.3.2.2 Bulk Density and Flowability

When a significant volume of a particulate material is collected in a containing vessel with stationary air filling the interstices, the material is said to be a bulk material [37].

Several important properties can be determined for bulk materials, among which the bulk density, ρ_{bulk}, is defined as the ratio between the mass of the particles and the total volume they occupy within the container. The corresponding void fraction is then calculated as:

$$\varepsilon_{\text{bulk}} = 1 - \frac{\rho_{\text{bulk}}}{\rho_p} \tag{2.5}$$

Because this measurement depends on the packing efficiency of the particles inside the vessel, it cannot be regarded as exact. If the powder is poured gently, the resulting bed will occupy a larger volume and therefore exhibit a lower bulk density; conversely, if the material is poured rapidly or tapped, the particles will settle more compactly, producing a higher bulk density.

The degree of compressibility of a particulate material can be expressed through the Hausner Index, defined as:

$$\text{Hausner index} = \frac{\text{Tapped bulk density}}{\text{Loose packed bulk density}} = \frac{\text{Loose packed bulk volume}}{\text{Tapped bulk volume}} \tag{2.6}$$

A particulate material with a Hausner index less than about 1.2 generally flows and fluidizes well, whereas a value of 1.5 or greater denotes poor flowability [37][38].

A summary of particle characteristics and environmental conditions that typically promote good fluidization behaviour is reported in the following table:

Property	Desirable	Undesirable
Shape	Rounded, sphericity $\gtrsim$0.7	Extreme, e.g. needles, discs
Mean diameter	Between ~50 µm and ~1.6 mm	$\lesssim$40 µm and $\gtrsim$3 mm
Size distribution	Unimodal, $2 \lesssim d_{p90}/d_{p10} \lesssim 20$	Bi- or tri-modal; excessively broad; completely uniform
Surface roughness	Smooth surfaces	Asperities higher than $d_p/20$
Rigidity/flexibility	Rigid	Flexible, deformable
Attrition resistance	Robust	Friable
Humidity	10% $\lesssim$ RH $\lesssim$ 60%	RH $\lesssim$ 2% and $\gtrsim$80%

Table 2.1: Particle properties and gas relative humidities (RHs) that generally promote good "fluidizability" [37].

It should be noted that these guidelines are primarily applicable to low-temperature fluidization processes. In high-temperature systems, such as those considered in this work, particle and gas properties can differ significantly from their values under ambient conditions. In particular, elevated temperatures may cause softening or partial melting of particle surfaces, which can lead to sintering—that is, the formation of a solid mass through compaction without the particles reaching their melting point.

2.3.3 Particle Properties Influence

The fluidization behaviour of a particle bed depends not only on the properties of the fluidizing gas but also strongly on the characteristics of the particles themselves. Parameters such as particle diameter, shape, density, and porosity, as well as surface roughness and thermal or dielectric properties, influence the drag forces, interparticle interactions, and heat and mass transfer within the bed.

2.3.3.1 Diameter

Particle diameter is extremely important for characterisation of fluidization processes. It is determined either through a sieve/screening analysis, or through a particle size distribution analysis (the latter is the technique used in this thesis). Various sphere-equivalent diameters are also often used, and the one most used in fluidization [37] is the Sauter mean diameter, defined as:

$$d_{p,32} = \frac{6V_p}{S_p} \tag{2.7}$$

here, V_p and S_p represent the total volume and the total exterior surface area of the particle, respectively. In case of a perfectly spherical particle, it equals the actual diameter.

The number 32 inside of the subscript comes from the fact that the Sauter mean diameter is the ratio of the third moment over the second moment of the probability density function.

2.3.3.2 Shape

Real systems never have perfectly spherical particles, so the sphericity ϕ is used to characterise their deviation from the ideal case:

$$\phi = \frac{\text{Surface area of a sphere of the same volume as the particle}}{\text{Actual exterior surface area of the particle}} \tag{2.8}$$

It is evident that in order to calculate the real sphericity of a particle, preliminary analysis of the geometrical characteristics of the particle system need to be carried out. Typical sphericities are shown in figure 2.21:

Particulate material	Typical sphericity
Glass beads	0.99
Crushed coal	0.75
Rounded sand	0.90–0.95
Angular sand	0.6–0.8
Common salt	0.84
Mica flakes	0.28

Figure 2.21: Typical sphericities of common materials [37].

The values in figure 2.21 are purely representative, since the actual shape of a particle depends heavily on the process through which it was made and not only on the material.

Since it might be difficult to determine the sphericity accurately, an estimation can be carried out using circularity, which is the 2D analogue of sphericity (based on the perimeter of the projected area).

2.3.3.3 Density

To achieve fluidization, the upward drag force exerted by the gas must equal or exceed the gravitational force acting on the particles. Consequently, the particle density ρ_p becomes a crucial parameter. This value is determined by both the intrinsic density of the constituent materials ρ_m and the particle's internal porosity. It is given by:

$$\rho_p = \rho_m \cdot (1 - \text{particle porosity}) \tag{2.9}$$

Using the bulk density (density of a mass of loose-packed particles) is also common [33]:

$$\rho_{\text{bulk}} = \rho_p \cdot (1 - \varepsilon_{\text{bulk}}) \tag{2.10}$$

In equation 2.10 $\varepsilon_{\text{bulk}}$ stands for the bulk voidage or void fraction of the bulk particulate material (usually around 0.36 for spherical particles arranged in a random close packing).

2.3.3.4 Surface roughness

Surface roughness increases friction between particles that come into contact and slide on each other during their movement, causing some of their kinetic energy to be lost [39].

Asperities on the surface might also affect the drag force and how close particles can get to each other [40], therefore also influencing interactions like van der Waals forces, and particle-to-wall and particle-to-particle heat transfer.

2.3.4 Minimum Fluidization Velocity Calculations

The superficial gas velocity at which fluidization is initiated, known as the minimum fluidization velocity (u_{mf}), is one of the most important parameters in fluidized bed applications. It defines the minimum gas flow rate required to achieve fluidization in a given column, and therefore determines the gas consumption within the furnace in this study. Furthermore, u_{mf} appears in several correlations and equations that are essential for predicting other properties of fluidized beds.

Although it is theoretically possible to calculate this velocity using empirical or semi-empirical correlations, it should always be verified experimentally. This is because such correlations often neglect many of the particle properties discussed in Chapter 2.3.3, which can significantly influence the behaviour of the fluidization process, leading to potential inaccuracies in theoretical predictions.

2.3.4.1 Experimental Determination of the Minimum Fluidization Velocity

The most common method for the experimental determination of the minimum fluidization velocity is the pressure drop method. In this approach, a sample of powder is placed inside a cylindrical vessel equipped with a gas distributor—a horizontal perforated plate located at the bottom of the column. The distributor allows the gas to pass through while preventing particle leakage. Its main function, as the name suggests, is to ensure uniform gas distribution across the vessel cross-section.

After leveling the surface of the powder bed, the gas flow rate is gradually increased in steps. At each step, the pressure drop (ΔP) across the bed and the diffuser plate is measured. To isolate the contribution of the powder bed from that of the distributor, a blank test (without powder) must be performed. The pressure drop measured in this test is then subtracted from the total to obtain the pressure drop due solely to the bed.

When the results are plotted, the minimum fluidization velocity corresponds to the intersection point of two extrapolated lines:

- An horizontal line that is fitted to the horizontal part of the graph, which is the part after which fluidization was initiated;

- A line fitted to the increasing d_p line at lower flow rates.

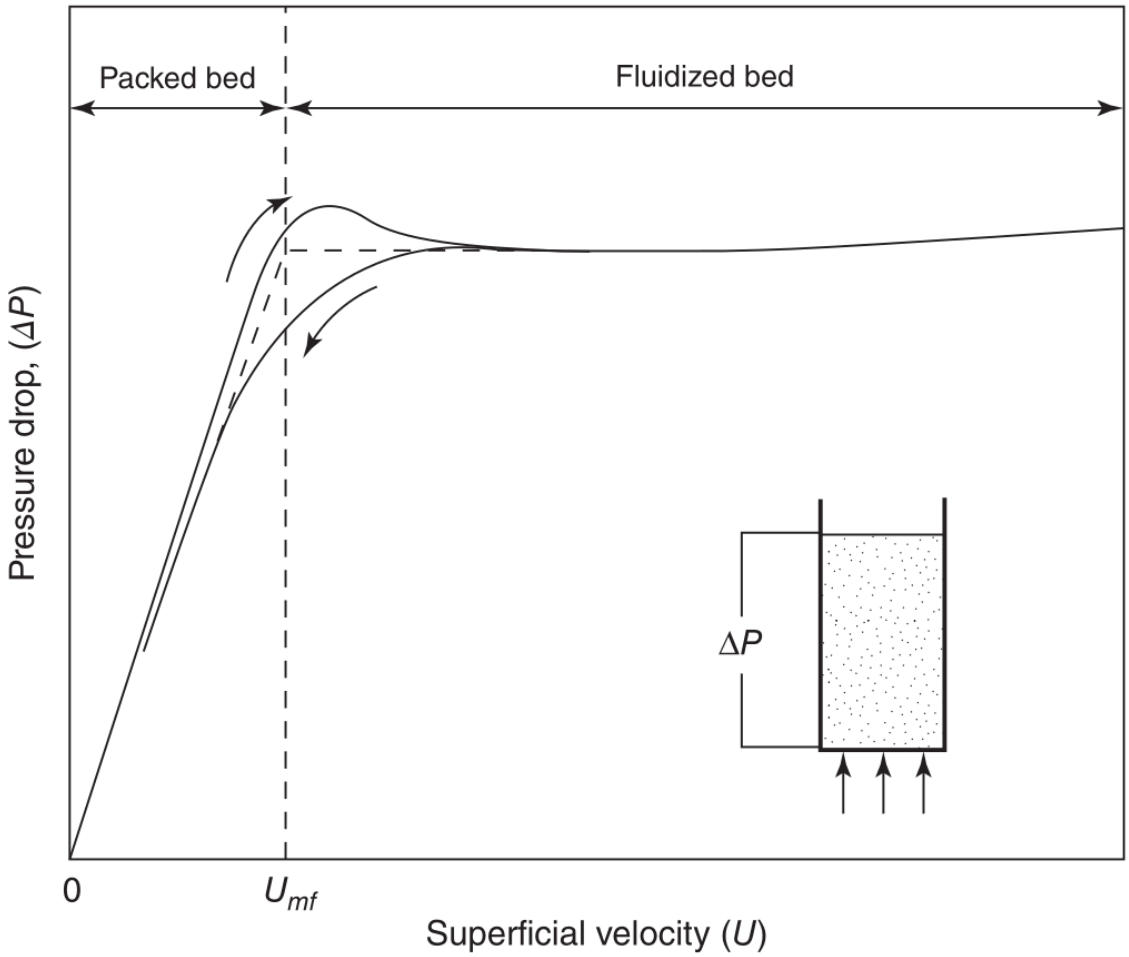


Figure 2.22: Graphical identification of the minimum fluidization velocity [37].

The resulting pressure-drop-versus-velocity graph (as shown in figure 2.22) exhibits a plateau beyond u_{mf} because, once fluidization is achieved, the weight of the particles is balanced by the drag force, and any further increase in gas velocity only enhances the agitation of the bed without increasing the pressure drop.

Other experimental methods to determine the minimum fluidization velocity are:

- An alternative approach is the sinking weight method, which involves placing a large and dense object on top of the unfluidized bed. The gas flow is then increased gradually, as in the pressure drop method, until the object begins to sink. The corresponding superficial velocity is taken as the minimum fluidization velocity. This method tends to slightly underestimate u_{mf}, as the object locally increases the gas velocity around its edges [37];
- A simpler, though less precise, technique is the visual method, applicable when the vessel is transparent. In this case, the transition from a static to a fluidized state can be determined through visual inspection. This approach works reasonably well for uniform particle systems, but it becomes less reliable when the material exhibits a broad particle size distribution or other variations in physical properties.

2.3.4.2 Theoretical Determination of the Minimum Fluidization Velocity

Most of the equations developed to describe fluidization behaviour rely on the principle that, at minimum fluidization, the net weight of the particles (i.e., the weight minus buoyancy) is balanced by the drag force exerted by the fluid. Because drag is proportional to the pressure drop through the bed, u_{mf} can be predicted by identifying the condition where the pressure drop across a fixed bed equals the weight of the bed per unit cross-sectional area.

The Ergun equation is commonly employed to describe the pressure drop through a packed bed, given its height H, voidage ε_{mf}, particle diameter d_p, sphericity ϕ, μ is the dynamic viscosity, and ρ_f the fluid density:

$$\frac{\Delta P}{H} = \frac{150 u_{mf} \mu}{(\phi d_p)^2} \frac{(1-\varepsilon_{mf})^2}{\varepsilon_{mf}^3} + \frac{1.75 \rho_f u_{mf}^2}{\phi d_p} \frac{1-\varepsilon_{mf}}{\varepsilon_{mf}^3} \tag{2.11}$$

where the first term on the right-hand side, dominant at low Reynolds numbers (Re), represents viscous forces; while the second term, dominant at high Reynolds numbers, accounts for inertial drag.

At the point of minimum fluidization, the pressure drop ΔP is equal to the effective weight of the bed, allowing u_{mf} to be determined:

$$-\Delta P = (\rho_p - \rho_f) g (1-\varepsilon_{mf}) H \tag{2.12}$$

Building upon this, Wen and Yu [41] derived an empirical correlation that eliminates the dependence on parameters such as voidage and sphericity, which are not always easily measurable:

$$u_{mf} = \frac{\mu}{\rho_f d_p} \left(\sqrt{33.7^2 + 0.0408 Ar} - 33.7 \right) \tag{2.13}$$

Here, $Ar = \rho_f g (\rho_p - \rho_f) d_p^3 / \mu^2$ refers to the Archimedes number, which expresses the ratio of gravity to viscous forces.

The accuracy of Equation 2.13 depends strongly on the Geldart group of the material: it is within ± 20% for Groups B and D, but the error increases to ±40% for Group A particles [37].

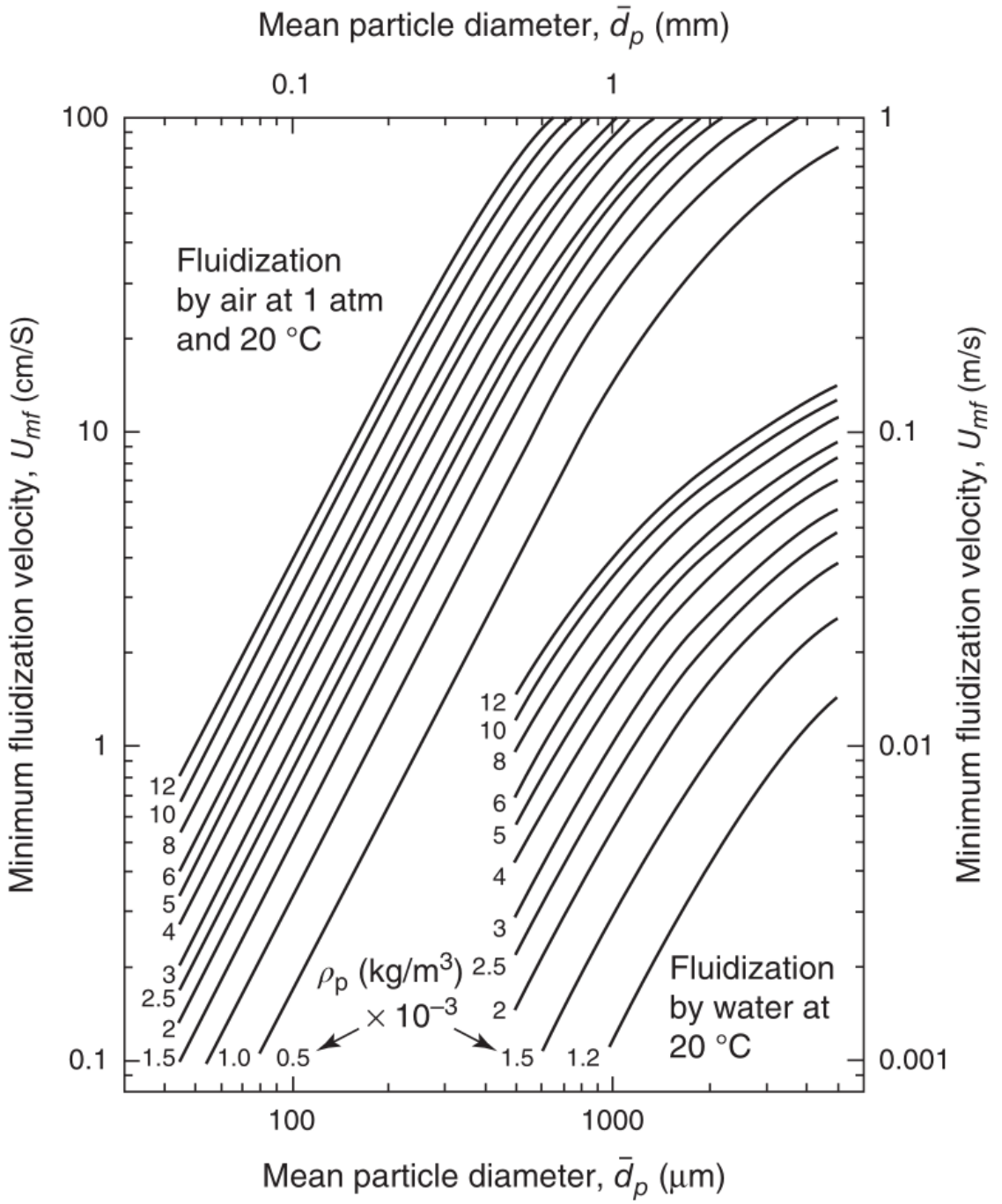


Figure 2.23: Minimum fluidization velocity, u_{mf} , for spherical particles of different densities and mean diameters in air at 20 °C and 1 atm pressure, and in water at 20 °C [37].

For small particles particles (which means low Ar), equation 2.13 approaches the limit:

$$u_{mf} = \frac{0.00061 g(\rho_p - \rho_f) d_p^2}{\mu} \tag{2.14}$$

This equation is valid for $Ar < 10^3$.

In more recent developments, Xu and Zhu [42] proposed a modified correlation that incorporates the cohesive solid bridge force into the Ergun equation by explicitly considering interparticle forces in the packed-bed force balance.

$$\left(\frac{\Delta P}{H}\right)_{\text{drag}} = \left(\frac{mg}{AH}\right)_{\text{weight}} + \left(\frac{\sigma}{H}\right)_{\text{coesion}} \tag{2.15}$$

The first term after the equal sign is the shorthand version of the terms in equation 2.13, whereas the last term is Xu and Zhu's addition, due to the tensile stress of the particle bed:

$$\left(\frac{\sigma}{H}\right)_{\text{coesion}} = \frac{1-\varepsilon_{mf}}{\varepsilon_{mf}} \frac{F_c}{d_{32}^2} \frac{1}{H} \tag{2.16}$$

In equation 2.16 F_c denotes the sum of all inter-particle cohesive forces acting between two particles in a bed and d_{32} the Sauter mean diameter. F_c is given by Kuczynski [43]:

$$F_c = \pi x^2 \sigma_{sb} \tag{2.17}$$

where σ_{sb} represents the tensile strength of the neck with radius x:

$$x = \left(\frac{56\gamma\delta^4}{kT} D_s a^3 t_c\right)^{\frac{1}{7}} \tag{2.18}$$

Here, γ stands for the surface free energy, δ the lattice spacing, k the Boltzmann constant, T the temperature, a the curvature radius of the particle (equal to $d_{32}/2$) and t_c the contact time (whose correlation to the particle size and the characteristic velocity, approximately equal to the minimum fluidization velocity u_{mf}, is given in equation 2.20). D_s is the solid state surface self-diffusion coefficient of the material, given by the Arrhenius-type equation:

$$D_s = D_{0,s} \cdot e^{-E_A/(RT)} \tag{2.19}$$

In equation 2.19 $D_{0,s}$ refers to the frequency factor, E_a the activation energy and R the universal gas constant.

The contact time t_c during fluidization is given by:

$$t_c = \frac{d_{32}}{\xi u_{mf}} \tag{2.20}$$

where ξ denotes a factor between 0 and 1 (typically $0.1 \div 0.15$). In this work $\xi = 0.125$ was used.

A short table that summarizes the values used for Xu and Zhu's correlation is given below in figure 2.24:

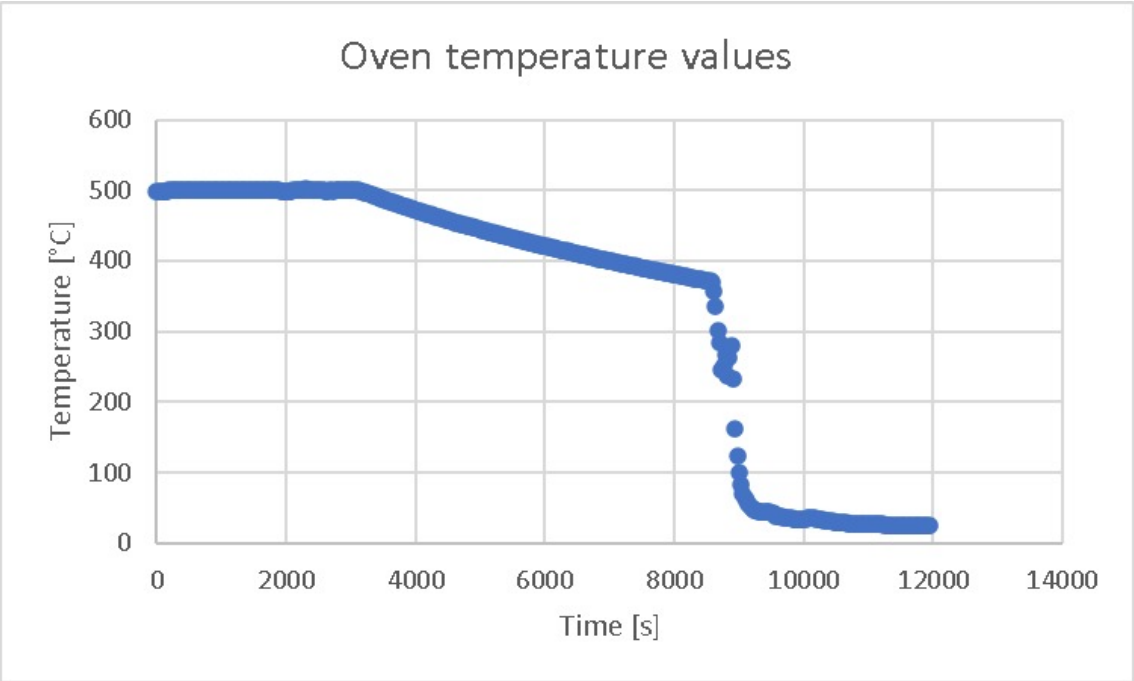
Parameter	Value	Source
Surface free energy, γ	1.44 N/m	[51]
Curvature radius, a	$\frac{1}{2}d_{32}$	[52]
Frequency factor, $D_{0,s}$	$5.2 \cdot 10^{-4}$ m^2/s	[53]
Activation energy, E_a	230 kJ/mol	[53]
Empirical factor, ξ	0.1–1	
Void fraction, ε_{mf}	0.4	
Particle density, ρ_s	4601 kg/m^3	
Sauter mean diameter, d_{32}	56.63 µm	
Gravitational constant, g	9.81 m/s^2	
Boltzmann constant, k	$1.381 \cdot 10^{-23}$ J/K	
Universal gas constant, R	8.314 J/(mol K)	

Figure 2.24: Properties used in minimum fluidization model [44]. Since the values depend on the material (iron-oxide), they can be used for a preliminary theoretical calculation.

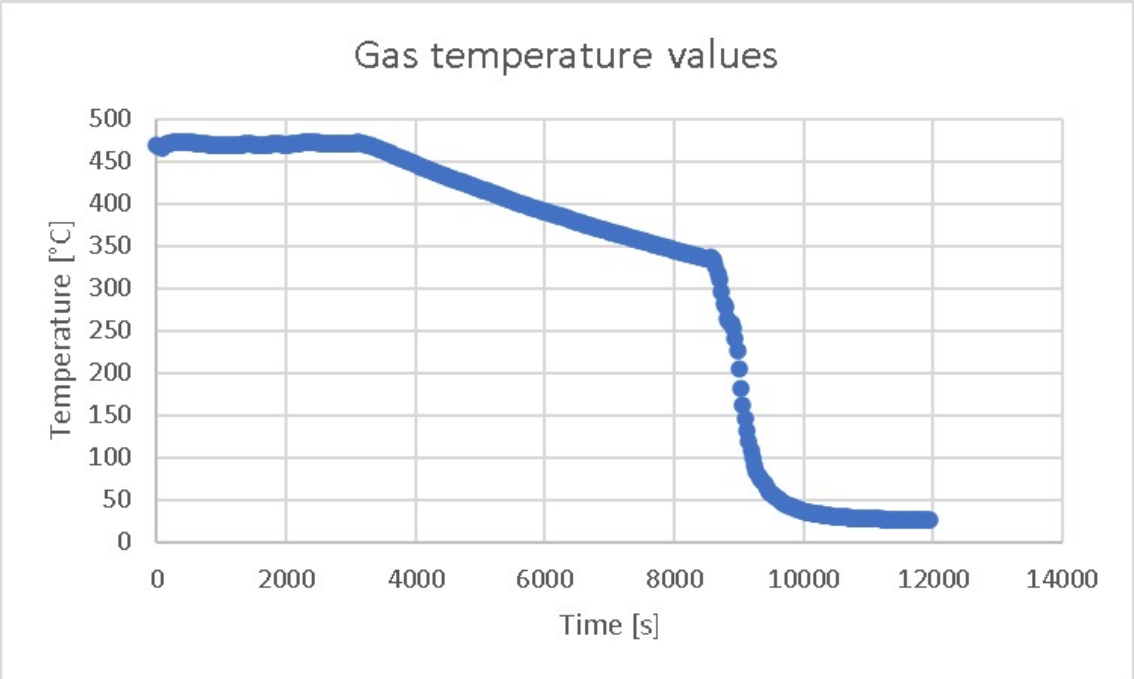
For the calculations of the minimum fluidization velocity, all three equations 2.13, 2.14 and 2.15 were used, in order to have a confront between the various correlations and the experimental results.

2.4 Cooling Time and Temperature Profiles

For each of the experiments analysed, as well as their subsequent cooling phases, two distinct cooling stages were observed. The first stage occurred with the furnace doors closed (hereafter referred to as ”closed cooling”), while the second stage involved the doors being opened (hereafter ”open cooling”). The open cooling stage was initiated once the furnace interior had reached a moderate temperature relative to that of the reaction—typically around 400-450 °C. This approach was employed to reduce the overall cooling time of the powder within the reaction chamber and to conserve nitrogen gas, as the contents of a single 300 bar, 50 L bottle were insufficient to supply both the reaction and the cooling process, given that bottle replacement during the experiments was not feasible. Additionally, maintaining nitrogen flow until the powder cooled was essential to prevent oxidation in case the powder remained hot after gas flow ceased.



(a) Oven temperature progress.



(b) Gas temperature progress.

Figure 2.25: Comparison of gas and oven temperature trends during a representative experimental run and its subsequent cooling phase. As illustrated, the gas temperature remains consistently lower than that of the oven throughout the entire process.

The gas temperature exhibits a similar general profile to that of the furnace (figure 2.25), but remains consistently lower. This occurs because the gas enters the furnace at approximately room temperature and is subsequently heated within the tubing before reaching the gas temperature sensor. Consequently, the difference between

furnace and gas temperatures is strongly influenced by both the oven temperature and the gas flow rate.

The two cooling modes, initially with the furnace doors closed and subsequently with them opened, are clearly distinguishable in the images. Since they follow different temporal trends, they are analysed separately in the following discussion.

As a first hypothesis, obtained by looking at the general profile of the curves, both curves were fitted with an exponential curve of the type $T(t) = A \cdot e^{Bt}$, in which A and B are numerical fitting constants.

For the closed cooling phase, this type of function provided an excellent fit to the experimental data, with coefficients of determination around $R^2 \approx 0.99$. A closer inspection of the obtained A coefficients revealed that they were all approximately $0.92 \div 0.98$ times the initial temperature at the beginning of the cooling phase (i.e., the reaction temperature). On this basis, a refined expression was proposed for describing the temperature evolution, in which the curve depends only on two global coefficients and the reaction temperature:

$$T(t) = T_{\text{reaction}} \cdot A' \cdot e^{Bt} \tag{2.21}$$

3. Materials and Methods

3.1 Experimental Setup

The furnace used for the reduction experiments was a ThermoLine-HEAT 1050 °C, a high-temperature furnace developed by IBT specifically for gas-solid reduction processes. It consists of an internal powder crucible (shown in figure 3.2), which is held in place by the external casing of the furnace (that can be seen in 3.1). The outer casing also functions as a thermal shield, ensuring a uniform temperature distribution and minimizing heat losses to the surroundings.

Inside the main chamber, electrical resistances provide the heat required for the reduction process. The system is connected to a dedicated electrical cabinet, which not only supplies power to the furnace but also records data from the internal sensors. Through a touch-screen interface, the user can program, control, and monitor the temperature profile of the furnace in real time.



Figure 3.1: The furnace used in the experiments, inside of the laboratory.

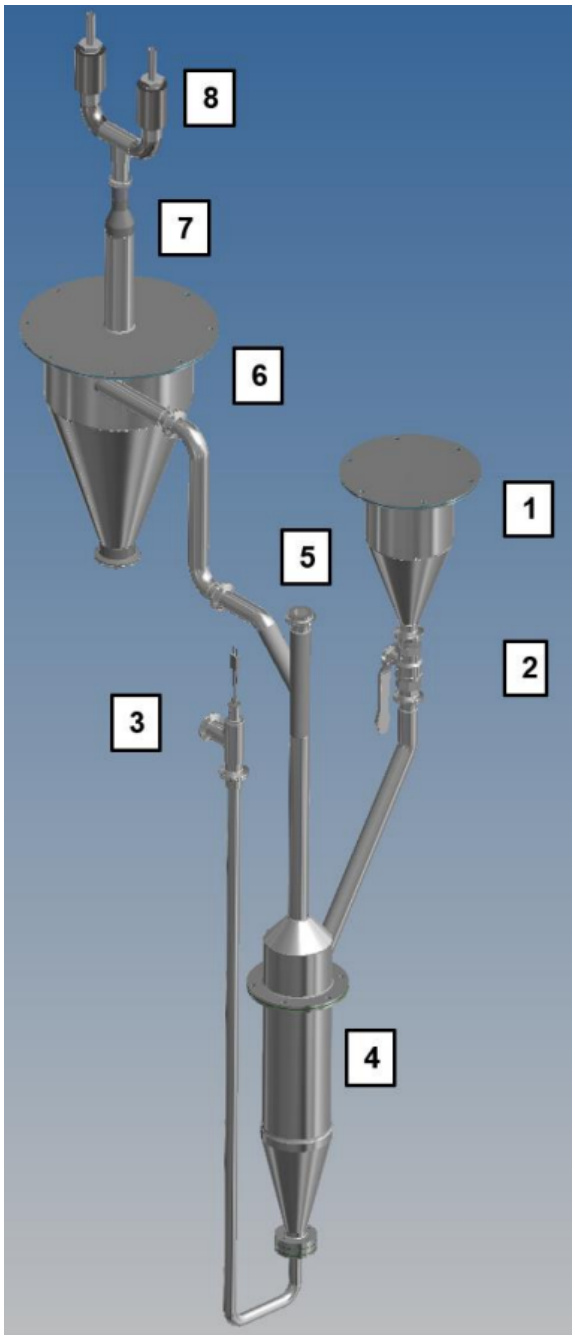


Figure 3.2: Scheme of the internal structure of the furnace. The tip of the gas temperature sensor (indicated with number 3 in the picture) is located near the first 90° bend of the gas input line when it is mounted. From IBT's manual of the furnace.

Two different temperatures were selected for the experiments: 500 and 600 °C. These temperatures were chosen because they are located below and above the stability limit of wüstite, respectively, allowing both reduction pathways to be investigated.

The program implemented in the furnace followed the same structure for each experiment:

1. Initial heating phase: the furnace was heated at a nominal rate of 15 K/min. During this phase, a low flow rate of nitrogen was introduced to purge the chamber of residual air and create an inert atmosphere;

2. First stabilization phase: the nitrogen flow rate was increased and maintained constant for approximately 5 minutes to eliminate transient effects related to the change in flow rate;

3. Introduction of the hydrogen gas: the hydrogen flow was initiated while maintaining the same total flow rate and gas ratio (H_2/N_2) that would be used during the reduction phase. This step was sustained for 5 minutes to stabilise the gas composition inside the chamber;

4. Introduction of the powder: the powder, previously loaded into the hopper (component 1 in figure 3.2), was introduced into the reaction chamber (component 4) by actuating the discharge lever (component 2). To ensure complete delivery of the powder into the chamber, gentle mechanical agitation of the hopper was occasionally required;

5. Reaction phase: the reduction reaction was allowed to proceed for 30 minutes. This duration was selected to initiate a measurable degree of reduction without achieving complete conversion, allowing comparison of the relative reactivity of different powders under identical operating conditions;

6. Cooling phase: at the end of the reaction, the hydrogen flow was stopped and the chamber was purged with nitrogen to provide a protective atmosphere. The nitrogen flow rate was gradually reduced during cooling to keep the powder slightly fluidized, thereby preventing sintering of the particles. This step was continued until the nitrogen supply was exhausted.

For safety reasons, the post-burner (component 8 in figure 3.2) was activated throughout all phases in which hydrogen was present in the furnace, ensuring complete combustion of any unreacted hydrogen before exhaust release.

The volumetric gas flow rates for both the high-temperature and cooling phases were determined from the calculations performed to estimate the expected fluidization velocity at elevated temperatures, based on the values obtained from the ambient-temperature fluidization experiments. However, since these calculations were performed after the initial set of cold-bed tests, an incorrect reference flow value of 20 l/min at ambient temperature was used. This initial error led to excessively high gas velocities at elevated temperatures, resulting in considerable particle entrainment from the bed during operation.

Furthermore, post-oxidation of the reduced powders was observed after extraction from the furnace. Two main causes are considered plausible:

- The nitrogen contained in a single gas cylinder was insufficient to maintain the protective atmosphere for the entire cooling phase. Consequently, as the nitrogen flow decreased, air likely infiltrated the furnace while the sample was still hot, leading to oxidation.

- Only the outer layer of the powder bed, directly exposed to the gas stream and reactor walls, cooled sufficiently, while the core remained at a higher temperature. Upon removal, the apparently cold outer powder masked a still-hot interior, which subsequently oxidised upon contact with air.

This post-oxidation phenomenon was not unique to the present experiments. Similar behaviour was later observed in other tests carried out by different members of the research group. This recurrence suggests that the problem may be intrinsic to the current cooling procedure or related to the insufficient gas supply during the final phase of the experiments. A more robust protocol, such as the use of larger nitrogen reservoirs, automated flow regulation during cooling, or additional insulation of the reaction chamber, could help mitigate these issues in future campaigns. The implications of these effects, together with their impact on the accuracy of the results, are analysed in detail in chapter 5.

This chapter presents the preliminary analyses conducted to support the experimental phase of this study. The main objective is to develop an understanding of the system behaviour, particle properties, and operating conditions before the execution of the experiments.

The first section focuses on the analysis of historical sensor data collected from previous tests, with the aim of identifying temperature trends and estimating cooling times within the reactor.

The subsequent section describes the determination of the minimum fluidization velocity using an Excel-based model, examining its dependence on temperature and comparing theoretical predictions with literature correlations.

This is followed by the particle characterization phase, which includes thermogravimetric (TGA) and BET analyses to provide information on thermal stability, specific surface area, and porosity. Finally, blowout tests and external particle size analyses are presented to assess powder loss mechanisms and validate particle size distributions.

Taken together, these analyses form the foundation for interpreting the experimental results discussed in later chapters and for refining the design of the fluidization system.

3.2 Analysis of Historical Sensor Data from the Furnace

The furnace, whose components, structure, and operating principles are described in section 3.1, is equipped with a set of real-time temperature sensors. These sensors allow the acquisition of detailed temperature profiles, providing a continuous record of how the temperature evolves within the furnace during operation.

This capability is particularly valuable for determining the cooling rate of the system, which in turn can be used to achieve a more controlled gas flow through the reaction chamber during the two cooling phases. In previous experimental campaigns, this process had been regulated manually and qualitatively, relying on personal assessment rather than quantitative data. The use of recorded temperature data therefore represents a significant improvement in the control and reproducibility of the operating conditions.

From previous experiments, several temperature profiles were collected, referring both to the furnace temperature and to the gas temperature. The former was measured by sensors positioned outside the reaction chamber but still within the furnace housing, while the latter was recorded by sensors located inside the gas feed line supplying the gas mixture to the chamber.

The data collected from these sensors were imported into an Excel spreadsheet to generate temperature-versus-time profiles, from which the corresponding cooling curve equations were then determined.

The dataset used for this analysis comprises 5 experimental runs carried out under different operating conditions, covering a reaction temperature range between 500 °C and ≈ 715 °C.

The expression to describe the temperature evolution, depends only on two global coefficients and the reaction temperature, as seen in 2.21.

Table 3.1 presents the average values of the two coefficients, derived from the five available experimental runs. These values were obtained by averaging the coefficients extracted from the best-fit curves of each individual run.

Coefficient	**Average**	**St. dev.**	**% st. dev.**
$A'_{\mathbf{oven}}$	0.95	$2.47 \cdot 10^{-2}$	2.59 %
$A'_{\mathbf{gas}}$	0.95	$3.01 \cdot 10^{-2}$	3.15 %
$B_{\mathbf{oven}}$	$-4.84 \cdot 10^{-5}$	$3.08 \cdot 10^{-6}$	6.37%
$B_{\mathbf{gas}}$	$-5.65 \cdot 10^{-5}$	$4.78 \cdot 10^{-6}$	8.47 %

Table 3.1: Average, standard deviation and standard deviation as a percentage of the average for the cooling coefficients.

The slightly higher precision observed for the A coefficients compared to the B coefficients can be attributed to the fact that the latter appear in the exponential term of the equation, making them inherently more sensitive to small variations or uncertainties in the experimental measurements.

This model was able to predict the actual closed cooling time of the experiments with an accuracy of approximately 1%.

In contrast, the open cooling phase, although seemingly similar in shape (albeit with a steeper slope), did not conform to any standard analytical form. Consequently, it was not possible to obtain a satisfactory interpolation equation. This deviation is attributed to the coexistence of multiple heat transfer mechanisms (radiative and convective cooling in addition to the phenomena which were already present) which act simultaneously and render the overall phenomenon considerably more complex than the primarily Newtonian-type cooling observed during the closed phase.

A practical solution was therefore implemented: the furnace was allowed to cool in the closed configuration down to a fixed temperature, after which the open cooling phase commenced. The corresponding open cooling duration was known from prior experiments, allowing for accurate determination of the total cooling time:

$$t_{\mathrm{c,total}} = t_{\mathrm{c,\ closed}} + t_{\mathrm{c,open}} \tag{3.1}$$

Here, the first term can be directly calculated using equation 2.21, while the second term represents a fixed cooling duration. The switching temperature—the point at which the furnace doors are opened—was set at 400 °C, as this temperature was considered safe for the surrounding components temporarily exposed to heat.

Moreover, in most of the analysed experiments, the furnace had already been opened at approximately this temperature.

From this point, the time required for the temperature to drop from 400 °C to 50 °C (a level at which oxidation in air becomes extremely slow) was approximately 15 minutes. However, since the measured temperature corresponds to the sensor located just above the powder bed, it most likely reflects the temperature of the upper layer of the sample. To account for this, a minimum open cooling duration of 30 minutes was adopted in all cases.

It is also important to note that during the entire cooling process, a continuous flow of nitrogen gas was maintained through the chamber. This served a dual purpose: firstly, it prevented sintering of the high-temperature particles by keeping them in a fluidized state, and secondly, it enhanced heat removal by carrying away a portion of the thermal energy.

3.3 Minimum Fluidization Velocity Determination

3.3.1 Excel Model

An Excel file was developed to provide a dynamic tool for modifying the various parameters and visualizing in real time how the fluidization velocity changes as these parameters vary within the governing equations.

The viscosity and density values for hydrogen and nitrogen were obtained from the NIST Chemistry WebBook database [45].

To determine the properties of different hydrogen-nitrogen mixtures, a dedicated input cell was created to specify the percentage of H_2 in the mixture for which the calculations were to be performed. A linked reciprocal cell for the corresponding N_2 fraction was automatically updated, ensuring that only one input value needed to be manually adjusted.

For each of the three temperature conditions considered, ambient temperature, 500 °C, and 600 °C, two additional cells were associated with these gas fractions to compute the density and viscosity of the overall mixture.

The mixture density was calculated using a weighted average of the component gas densities, while the mixture viscosity was determined using Wilke's equation [46], which accurately describes the non-linear and non-monotonic behaviour of viscosity in gas mixtures:

$$\mu = \sum_{1=1}^{N} \frac{\mu_{g,i}}{1 + \frac{1}{y_i} \sum_{j=1, j\neq i}^{N} y_j \varphi_{ij}} \tag{3.2}$$

Here, y_i represents the fraction of the i-th gas in the mixture, and since we have only two gases $N = \{1, 2\}$. The coefficients φ_{ij} are calculated as follows:

$$\varphi_{ij} = \frac{\left[1 + \sqrt{\frac{\mu_{0,1}}{\mu_{0,j}}} \cdot \sqrt[4]{\frac{M_j}{M_i}}\right]^2}{\frac{4}{\sqrt{2}} \sqrt{1 + \frac{M_i}{M_j}}} \tag{3.3}$$

In equation 3.3 M stands for the molar mass of the gas.

Using all the three main equations delineated in the previous section (equations 2.13, 2.14 and 2.15), calculations for each of the temperatures were carried out.

Since the equation for the minimum fluidization velocity developed by Xu and Zhu contains u_{mf} in both sides of the equation, the Goal Seek analysis was used in order to compute the iterative solving process. The results of the whole analysis are exposed in the following section.

3.3.2 Cold Bed Reactor

The cold fluidized bed unit depicted in figure 3.3 was used to determine the minimum fluidization velocity and to execute the blowout experiments.

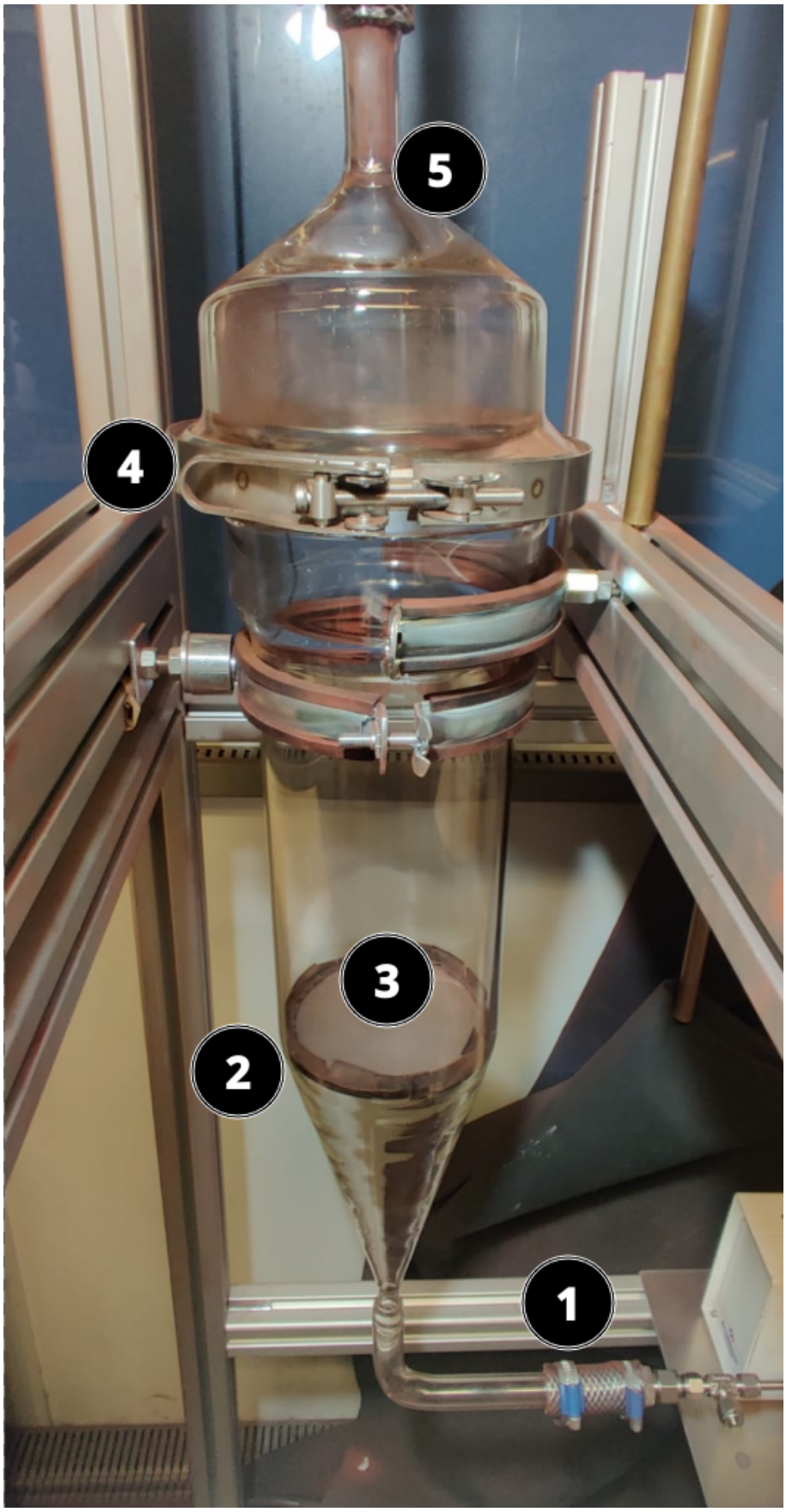


Figure 3.3: The cold bed reactor used for the experiments.

It is composed of various parts (here listed going up from the bottom):

1. Inlet: the gas enters from the inlet, and then proceeds up into the conical section of the reactor;
2. Diffuser plate: composed of different layers, it helps distribute and smooth the gas flow in the bed, helping creating a stable fluidization;
3. Powder bed: the powder sits on top of the diffuser plate, inside of the cylindrical section of the reactor;
4. Sealing lid: the connection between the bottom and top parts of the reactor. It has a flange and a seal, that allow for an air-tight closing of the reactor, while still allowing to insert the powder and clean the reactor between experiments;
5. Cover: the top-most part of the reactor, where the outlet is. From here the gas exits.

In addition to these components here, the flow was controlled with two different flow-controllers:

- Flow controller EL-FLOW F-201CV: for flows from 0 to 20 l/min;
- Flow controller EL-FLOW F-202AV: for flows greater that 20 l/min.
- Pressure drop sensor PU/PI from Halstrup Walcher: to calculate the pressure drop across bed and diffuser.

Two different controllers were employed because the F-202AV lacked precision at lower rates and exhibited slow stabilization, characterized by significant overshoot and long transients during set-point changes.

These two were themselves controlled through the use of the FlowView program, that allowed both for setting the desired output flow, and to check the actual flow in contrast to that.

In order to connect the sensors to the computer and to convert the electrical signal obtained from them to a form readable from the computer, a NI USB-6210 was used as an interface between them. A simplified scheme of the sensors and their connection is showed in figure 3.4:

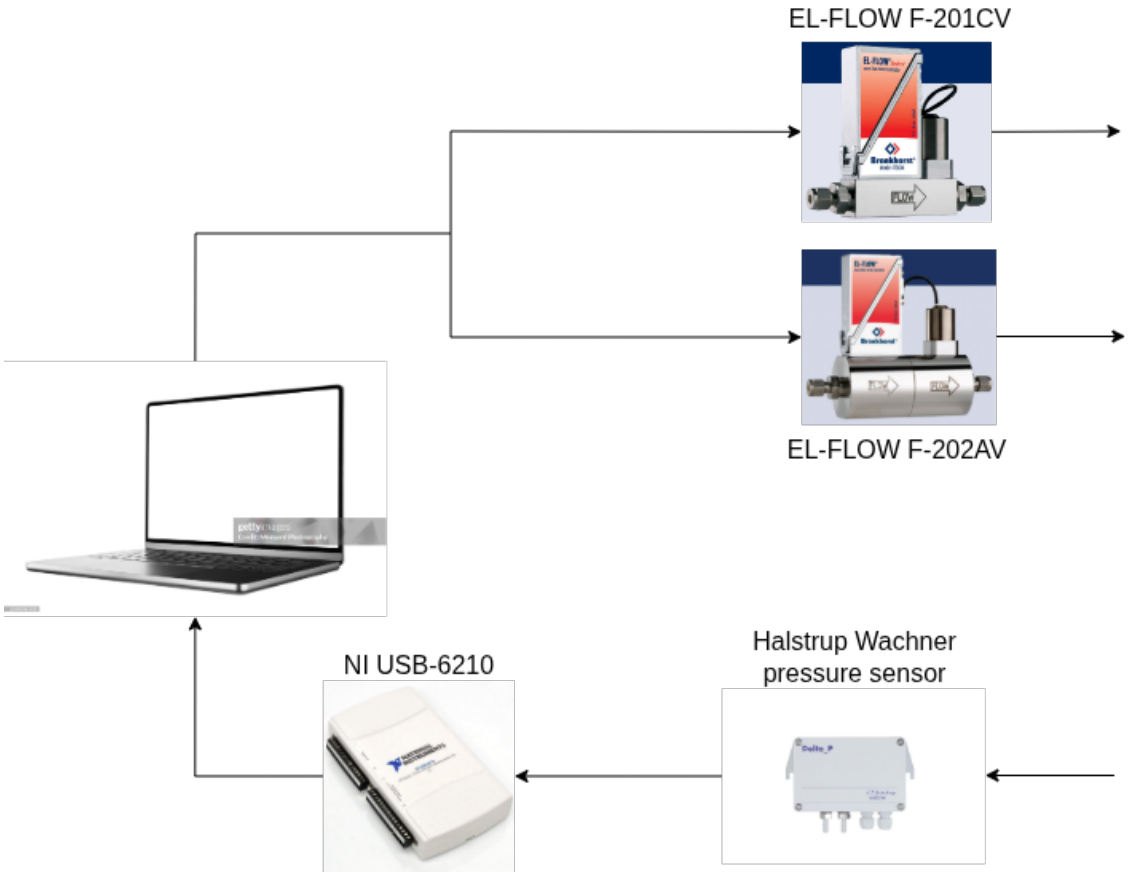


Figure 3.4: Diagram of the various connections between elements. The outputs of the flow controllers is the signal that effectively controls the amount of gas, and the input of the differential pressure sensor is the signal obtained from the pressure drop.

Another LabVIEW program (figure 3.5), developed during previous research, was used to visualize the instantaneous pressure in real time over two different time scales: the most recent 5 seconds, which allowed for precise observation of short-term fluctuations in the pressure drop, and the most recent 30 seconds, which provided a broader view of medium-term pressure variations. In addition to real-time visualization, the program also featured an automatic data logging function, which continuously saved the entire pressure drop history of each experiment in a .txt file. These files could later be imported into MATLAB or Excel for further analysis — for instance, to calculate the average pressure drop over a specific experimental period.

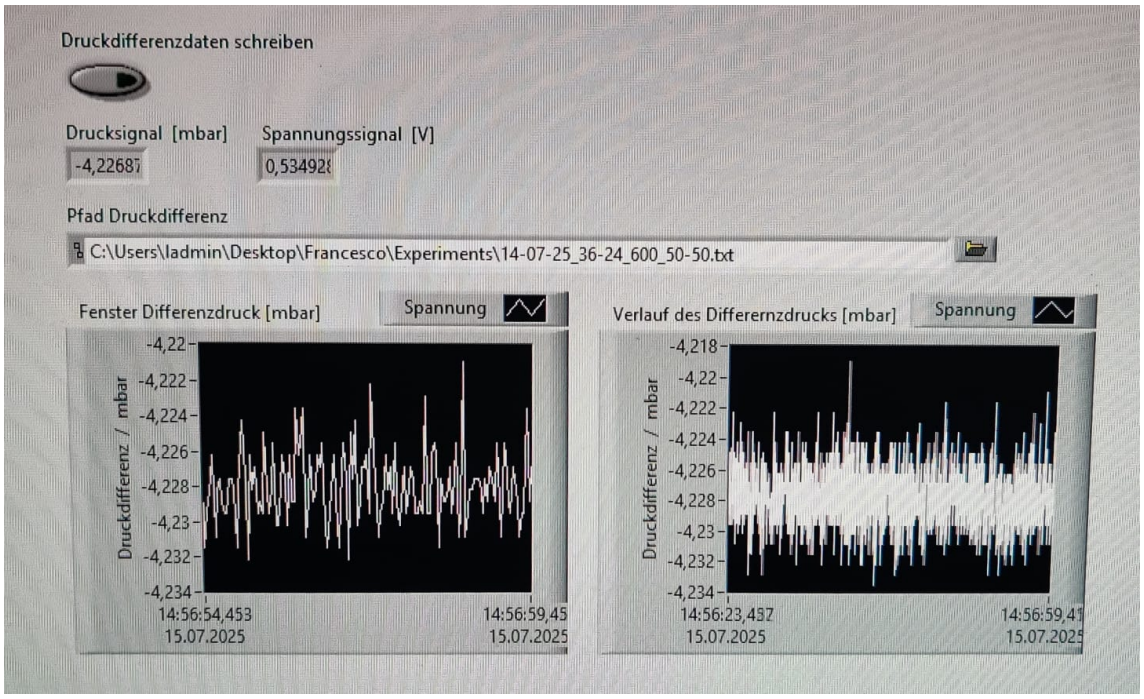


Figure 3.5: Screenshot from the LabVIEW program during use. The left graph showed the 5 s view of the pressure drop, the right one showed the 30 s view. The topmost button allowed to start and stop the recording of the data inside of the file specified in the "Pfad Druckdifferenz" field. The "Drucksignal" showed the conversion to a pressure from the instantaneous "Spannungssignal" (voltage signal) received from the Halstrup Walcher pressure difference sensor.

The pressure drop measurements were only used for the minimum fluidization velocity experiments, and not for the preliminary general tests aimed at determining whether a powder was capable of fluidizing, nor for the blowout tests.

The typical procedure followed for the preparation to a fluidization experiment is as follows:

1. Detach the connections of the glass vessel from the gas input and output pipes ;
2. Open the lid and remove the vessel from its supports;
3. Remove the powder inside of the vessel, if present, and clean everything with acetone. Let acetone vapours evaporate;
4. Replace the vessel inside of its supports, and then insert the new powder to be tested;
5. Close the lid and then re-attach all of the connections to the gas inputs and outputs.

Once the vessel was prepared, both the LabVIEW and FlowView programs were started, and a folder was created (if not already existing) to store the experimental data.

After setting a desired flow rate through the LabVIEW interface (illustrated in figure 3.6), it was necessary to wait for the flow to stabilize. This was confirmed when the "Setpoint" and "Measure" values shown in the FlowView window became identical. An additional short wait was applied to ensure full stability before starting data recording in LabVIEW.

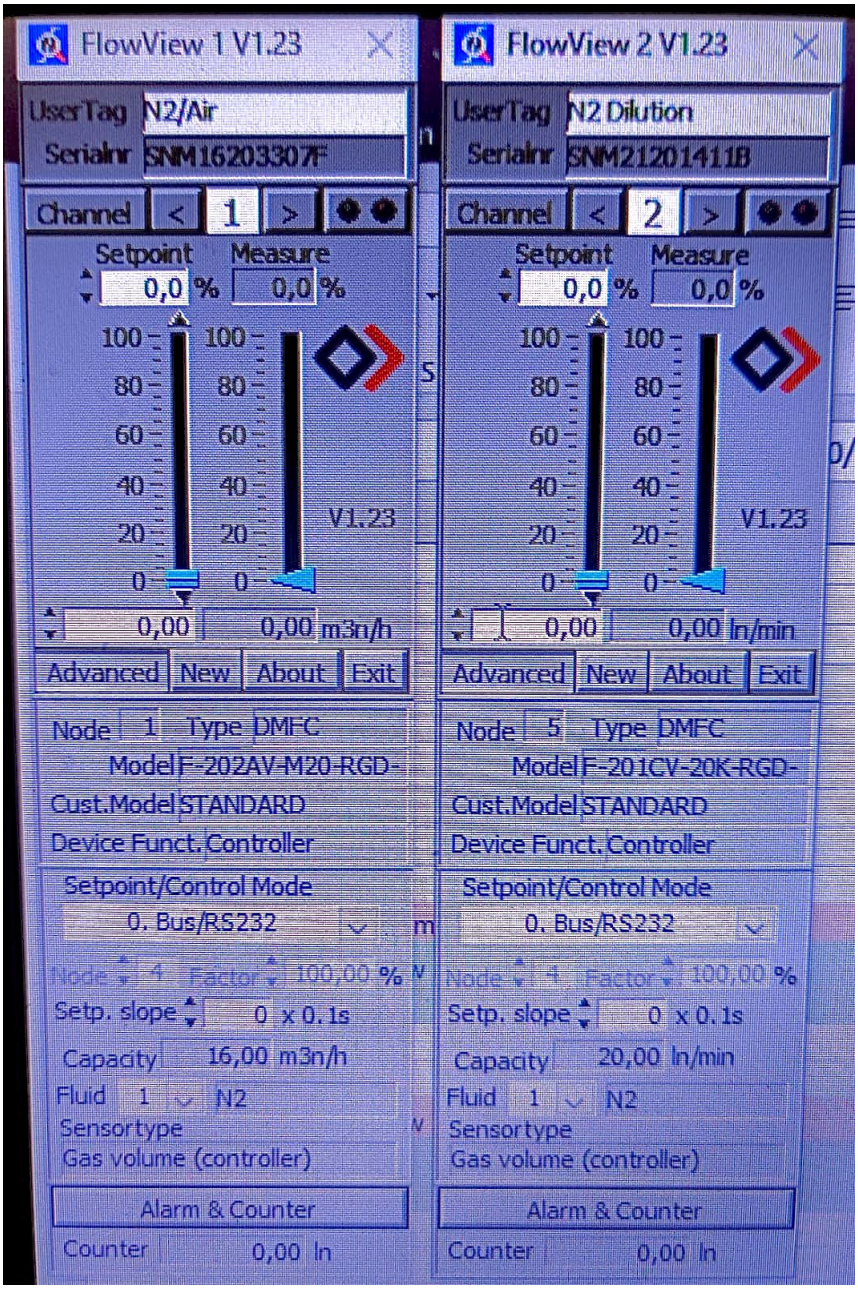


Figure 3.6: Visual of the FlowView program used to control the flow of the gas through the bed.

After waiting for a sufficient amount of time the measurement could be stopped. This was around 30-35 seconds, since this duration provides a sufficiently large dataset to capture, allowing for the calculation of a representative average pressure drop that is not altered by short-term anomalies or single bubble bursting.

The file name and flow conditions were then updated, and the procedure was repeated for the next experimental run.

Each of the files obtained was then analysed in Matlab in order to:

1. Remove eventual outliers from the measured data (due to random fluctuations in the data). This was done through the median absolute deviation (MAD) method: data points falling more than three scaled MAD from the median were identified as anomalies and substituted using linear interpolation. All of this was done through Matlab's `filloutliers` function;
2. Obtain the average value of the pressure drop for each measured flow;
3. Isolate the pressure drop of the powder bed by subtracting the baseline resistance of the diffuser plate. Since the distributor acts as a flow restrictor, it generates its own pressure drop. To account for this, a blank test (an identical run without any powder) was performed. The baseline pressure drop measured at each specific flow rate was then subtracted from the total pressure drop recorded at that exact same flow rate during the actual experiments.
4. Apply a zero-offset correction to account for sensor drift. The differential pressure sensor exhibited a baseline reading of approximately 4 mbar even in the absence of gas flow. To eliminate this and obtain the true pressure drop, this offset value was uniformly subtracted from the entire dataset.

3.4 Particle Characterization and Powder Selection

A fundamental aspect of any experimental study is a thorough understanding of the materials involved. In the present work, particular attention was devoted to characterizing the powders used during the fluidization and high-temperature reduction experiments. As previously discussed, both phenomena are highly sensitive to a wide range of particle and bulk properties, including chemical composition, surface area, crystalline structure, and the presence of impurities.

To ensure that the observed experimental behaviour could be correctly interpreted, an extensive set of analyses was carried out to determine these characteristics. Thermogravimetric analysis (TGA) was employed to investigate the thermal stability and potential mass changes of the powders during heating. The Brunauer-Emmett-Teller (BET) method was used to quantify the specific surface area, which plays a crucial role in gas-solid interactions during reduction. X-ray diffraction (XRD) analysis provided insights into the crystalline phases and internal structure of the materials, while complementary foreign element analysis allowed for the identification of possible contaminants that could influence reactivity and fluidization performance.

Additionally, specific tests were conducted to evaluate particle losses during operation and to verify the particle size distributions before and after experimentation. Together, these analyses form a comprehensive picture of the powders' physical and chemical characteristics.

The powders that were studied are 4:

1. Carl Roth Fe_2O_3: from here on out referred to as ”CR” or ”CR powder”;
2. 01/25 iron ore: it was provided by a company to be analysed. From here on out referred to as ”01/25”, ”01-25” (for compatibility with file naming best practices) or ”01/25 powder”;
3. 36/24 iron ore: it was also provided by the company. From here on out referred to as ”36/24”, ”36/24” or ”36/24 powder”;
4. MetallPulver 24 Fe_2O_3: from here ”MP24” or ”MP24 powder”.

3.4.1 Calorimetric analysis

In calorimetric analysis a sample is made to react inside a high-pressure oxygen atmosphere. The oxidation of the sample releases energy, which heats up a certain amount of water. This increase in temperature is then measured and used to determine the heat released during oxidation.

From this it is possible to obtain the reduction rate of the samples, since the more a sample was reduced, the more it can be oxidised again, therefore releasing more heat and heating the water more.

The machine used for the calorimetry analyses was the IKA C 200 (shown in figure 3.7):



Figure 3.7: The calorimetry vessel used for the analyses [47].

After each experiment was completed, the machine shows the calorific value of the sample, expressed in J/g. From these, using the calibration measurements and the theoretical value for the calorific value of pure iron ($\approx$ 7.36 kJ/g), the reduction degree of the samples is obtained. For example, if a sample shows a calorific value of about 3.7 kJ/g, we can determine that it is about 50% pure iron, so the reduction degree it is also 50%.

3.4.2 TGA Analysis

Thermogravimetric Analysis (TGA) is employed to determine the variation in sample mass over time at different temperatures during a reaction. This technique provides valuable information about phase transitions, absorption, adsorption and desorption phenomena, as well as thermal decomposition and solid-gas reactions (e.g., oxidation or reduction). In the present study, particular attention is given to the first and the last two of these processes.

A TGA machine consists of a sample holder that is lowered inside of the reaction chamber of the machine, that consists in an oven that regulates the temperature inside of the chamber. Figure 3.8 illustrates a typical configuration. A protective and/or a reactive gas can also be made to flow inside of the chamber.

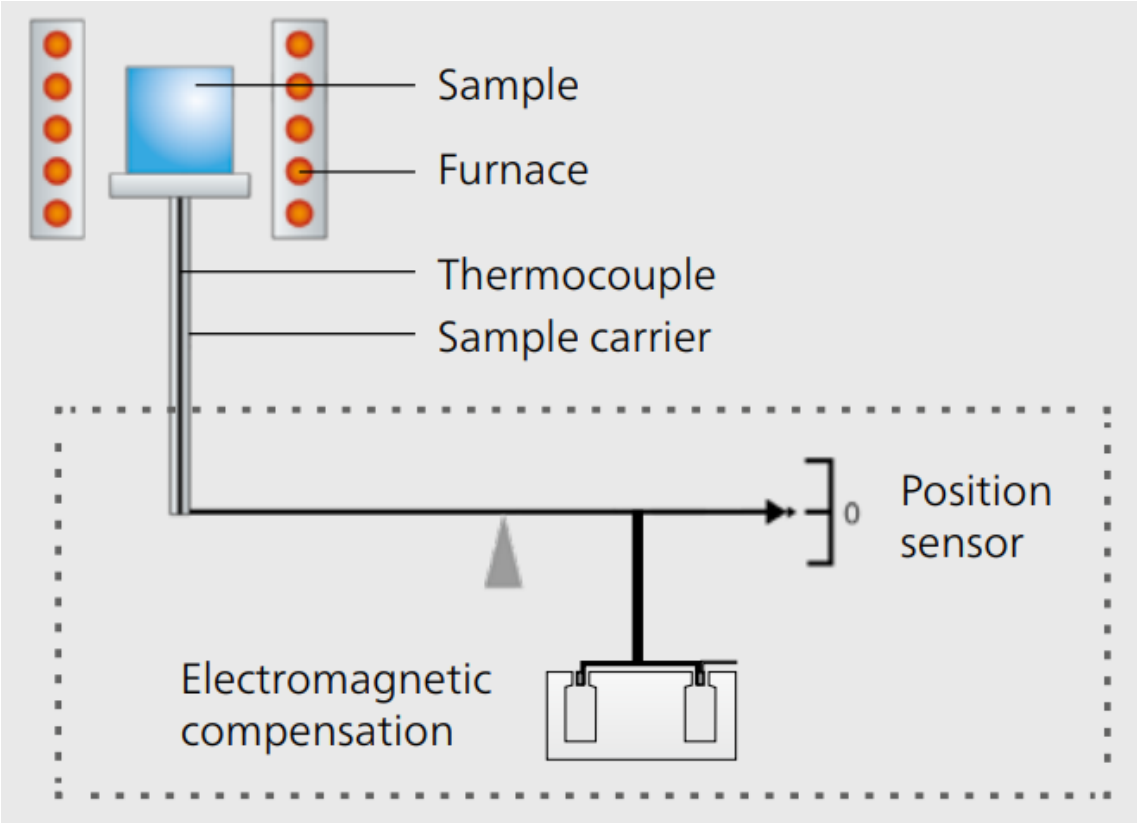


Figure 3.8: Schematics of the internal structure of the TGA machine [48].

The TGA apparatus in figure 3.9 that was used for the experiments is a NETZSCH TG 209 F1 Libra, equipped with an aluminum oxide (Al_2O_3) sample holder. The device is capable of operating up to 1100 °C, with a maximum heating rate of 200 K/min, a resolution of 0.1 μg, and the ability to introduce up to three different gases simultaneously into the reaction chamber.



Figure 3.9: The TGA machine used for the analyses.

Only the three powders provided by the company (namely, the 01/25,36/24, and 39/24 samples) were analysed in this work, since the CR powder had already been characterized in previous studies.

Each powder sample underwent testing at a variety of temperatures: 400, 500, 560, 570, 580, 600, 700, and 800 °C. The test structure remained consistent throughout: the temperature was ramped up to the reaction chamber at a heating rate of 15 K/min. During heating, the chamber was purged with 180 ml/min of N_2 gas. Once the target temperature was achieved, it was maintained constant for the reaction duration (5 hours). Concurrently, 20 ml/min of H_2 gas was introduced into the chamber, while the nitrogen gas flow was sustained.

The subsequent evaluation of the results enabled the calculation of the sample's mass loss, measured from the initiation of hydrogen gas flow into the chamber to the completion of the reaction. Additionally, the t_{10} and t_{90} times, depicting when the sample experienced 10% and 90% of the total mass loss since the reduction reaction began, were determined. These times were then analysed in conjunction with the BET analysis outcomes to investigate potential correlations between the reaction times and the particles' morphological properties.

3.4.3 BET Analysis

The Brunauer-Emmett-Teller (BET) theory seeks to explain the physical adsorption of gas molecules onto a solid surface and is employed to determine the specific surface area, facilitating the calculation of other morphological properties of the material, such as pore volume and pore diameter.

BET theory applies to multilayer adsorption systems that usually utilize a probing gas (called the adsorbate, in this case nitrogen) that does not react chemically with the adsorptive (the material upon which the gas attaches to, in our case the powder's surface) to quantify specific surface area. We use the BET equation to determine the monolayer volume of adsorbed gas, from which we can calculate the surface are of adsorbent. Figure 3.10 depicts a scheme of the increasing layers of adsorbate on the surface of the adsorptive:

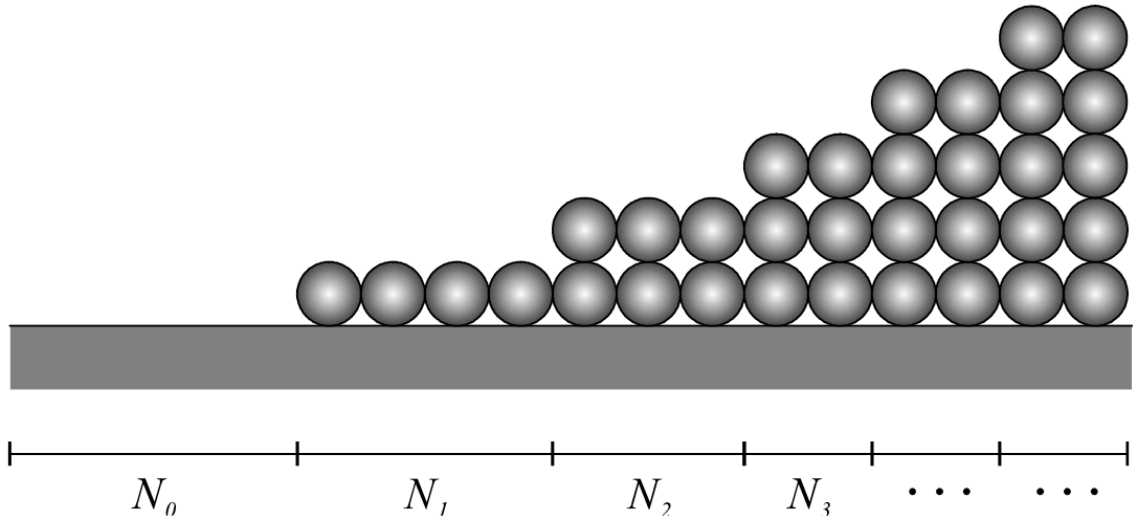


Figure 3.10: The BET adsorption model. N_i represents the adsorption sites that are covered by i layers of adsorbed molecules. At adsorption equilibrium N_i must remain constant, for every value of i [49].

The BET machine used in the experiments is a BELSORP-mini II (figure 3.11), equipped with two sample measurement ports and a third port for the reference sample. It can measure specific surface area from 0.01 m^2/g, pore sized from 0.35 nm with a resolution of 0.025 μL [50].



Figure 3.11: The BET machine used for the analyses.

The raw adsorption-desorption data collected during the experiments were analysed using the BELMaster software provided by BELSORP. The program applies several models, including the Brunauer-Emmett-Teller (BET) theory, the Barrett-Joyner-Halenda (BJH) method, and the t-plot approach, to compute a range of structural and surface parameters. From these calculations, the following quantities are obtained:

- From the BET plot:

  - V_m: monolayer adsorption capacity, representing the volume of gas required to form a single molecular layer over the sample surface. Measured in (cm^3/g);
  - C: BET constant (adimensional), related to the energy of adsorption. Higher C values indicate stronger adsorbate-adsorbent interactions;
  - d_{pores}: average pore diameter, usually derived from the pore volume and surface area. Measured in (nm);
  - $a_{s,\text{BET}}$: specific surface area calculated from the BET equation. Measured in (m^2/g);
  - V_{pores}: total pore volume, evaluated at a relative pressure $P/P_0 = 0.931$. Measured in (cm^3/g).

- From mesopore analysis. There are various methods used (BJH, CI, DH and INNES), which vary based on the assumptions used to calculate the various mesopore parameters:
  - V_p: cumulative pore volume. Measured in (cm^3/g);
  - a_p: pore surface area. Measured in (m^2/g);
  - $r_{p,\text{peak}}$: pore radius corresponding to the peak of the pore size distribution. Measured in (nm).

- From micropore analysis:
  - a_1: external surface area (non-microporous contribution), determined from the t-plot method. Measured in (m^2/g);
  - a_2: micropore surface area, derived from the difference between total and external surface areas. Measured in (m^2/g);
  - V_p: micropore volume calculated using the t-plot method. Measured in (cm^3/g);
  - $d_{p,\text{peak}}$: pore diameter at the maximum of the pore size distribution (measured in nm), with $d_{p,\text{peak}} = 2r_{p,\text{peak}}$.

3.4.4 XRD Analysis

X-Ray diffraction (XRD) analysis is an analytical technique that reveals information about the crystal structure, chemical composition, and physical properties of materials. The technique is based on observing the scattered intensity of an X-ray beam hitting a sample as a function of incident and scattered angle, polarization, and wavelength or energy [51]. An exemplary graph is shown in figure 3.12)

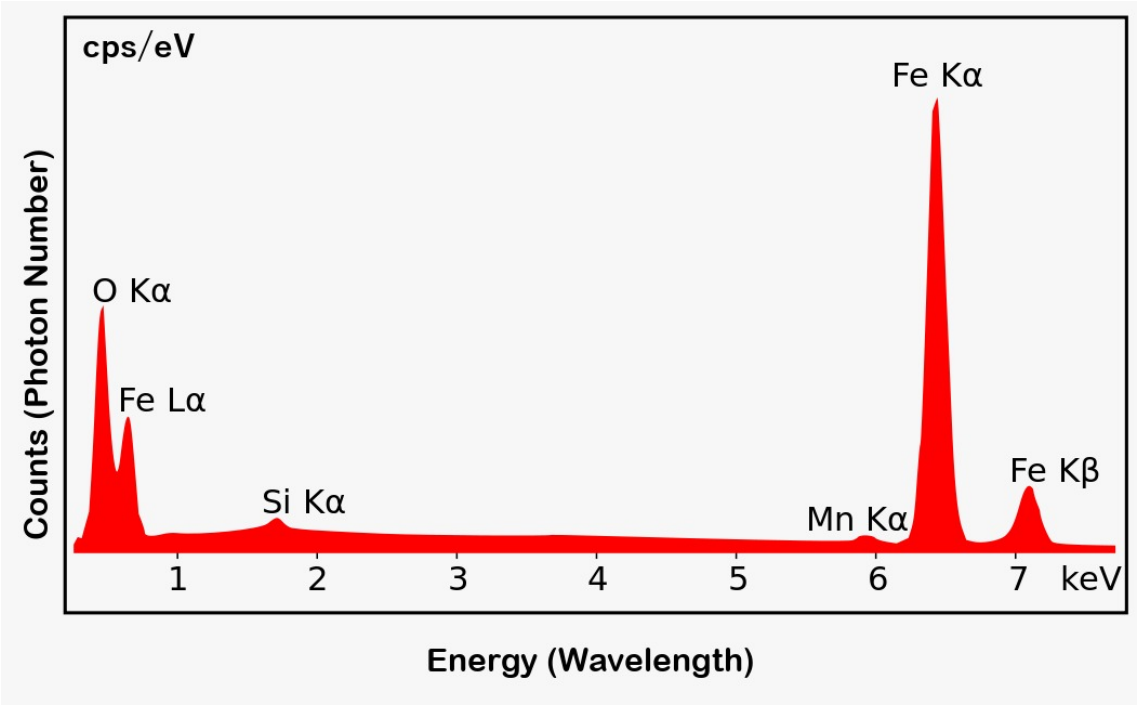


Figure 3.12: A typical XRD graph for an iron oxide sample. The peaks correspond to the various elements present in the sample [52].

This technique was used in the present work to obtain visual informations on the internal structure of the various powders and first informations on the elemental content of them.

3.4.5 Foreign Element Analysis

Two different analyses were used to determine the elemental content of the powders. The first is spectroscopy imaging, done in tandem with the XRD analysis of which we talked about in the last section. This was used to gain more information on how the various elements are positioned inside of the particles, giving an idea if different phases (that have different concentrations of elements) are present and how they are distributed throughout the particles. This was done only for the 01/25, 36/24 and MP24 powders.

The second was done with Inductively Coupled Plasma Optical Emission spectroscopy (ICP-OES), an analytical technique used to determine how much of certain elements are in a sample. The ICP-OES principle uses the fact that atoms and ions can absorb energy to move electrons from the ground state to an excited state. In ICP-OES, the source of that energy is heat from an argon plasma that operates at 10,000 kelvin. The ICP-OES principle relies on those excited atoms releasing light at specific wavelengths as they transition to a lower energy level. The amount of light released at each wavelength is proportional to the number of atoms or ions making the transition. The Beer Lambert law describes the relationship between light intensity and concentration of the element.

3.4.6 External Analysis of Particle Size Distribution

The particle size distribution analysis was carried out at a specialized laboratory within another department of the university, using a parallel beam laser diffraction machine.

The provided cumulative particle size distribution diagram in figure 3.13 illustrates the physical characteristic of the three iron ore powders from the company and the CR powder. The chart plots the cumulative percentage of particles (Verteilungssumme Q3 in %) as a function of their equivalent diameter (x in μm). This Q3 value represents the percentage of the total sample volume (or mass, assuming constant density) composed of particles smaller than the corresponding diameter on the x-axis. A steeper curve indicates a narrower size distribution, while a curve shifted further to the right signifies a coarser material.

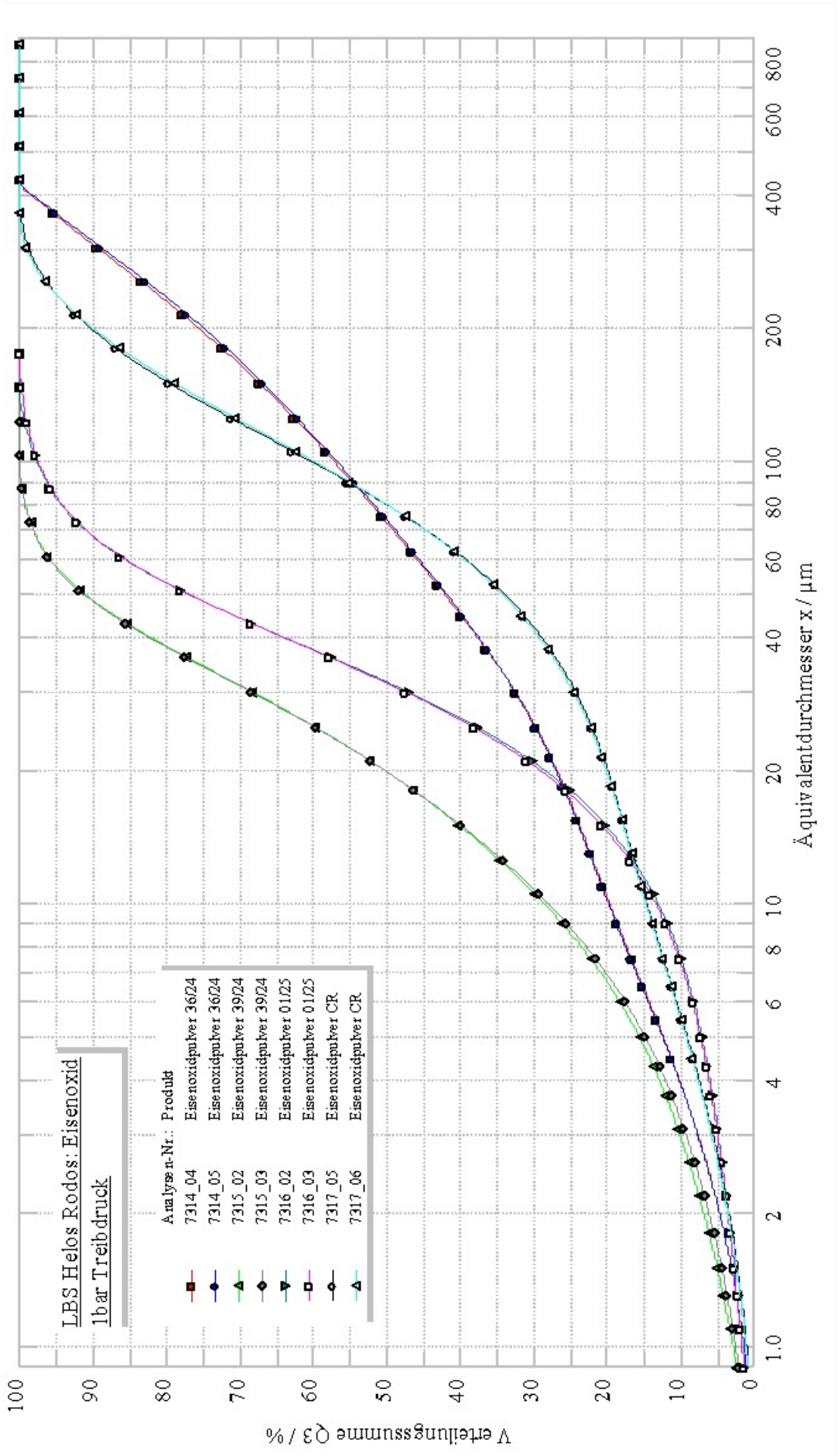


Figure 3.13: Particle size distribution of the different powders.

There are various key diameters to keep in mind when reading a particle size distribution graph:

- d_{10}: the size below which 10% of the material lies. This fraction is highly susceptible to elutriation (being carried out of the bed) and contributes to cohesive forces in the bed. It is also referred to as "fines";
- d_{50}: the size below which 50% of the material lies. It is the median size. It represents the "average" particle size and is the dominant factor in determining the minimum fluidization velocity and overall;
- d_{90}: the size below which 90% of the material lies. This fraction of large, heavy particles is prone to segregation and is the primary driver for a high u_{mf} and poor fluid-solid contact.

4. Results

4.1 Characterization Results

4.1.1 TGA Results

The isothermal reduction profiles for the three iron oxide powders are presented in the subsequent figures. These graphs plot the normalized mass percentage against time, in order to show the progression of the reduction reaction at each temperature. An examination of these curves can be used to determine the behaviour of each powder.

For a comprehensive analysis, the reduction profiles are presented in two distinct formats. The initial subsection features a series of plots wherein all reduction curves for a single powder are displayed on one graph, with temperature as the variable parameter. This format allows for a clear observation of the activation temperature and kinetic progression for each specific material. The following subsection then provides a cross-comparison through plots where the curves for all three powders are overlaid at identical temperatures. This arrangement facilitates a direct assessment of their relative reduction rates and efficiencies under standardized conditions.

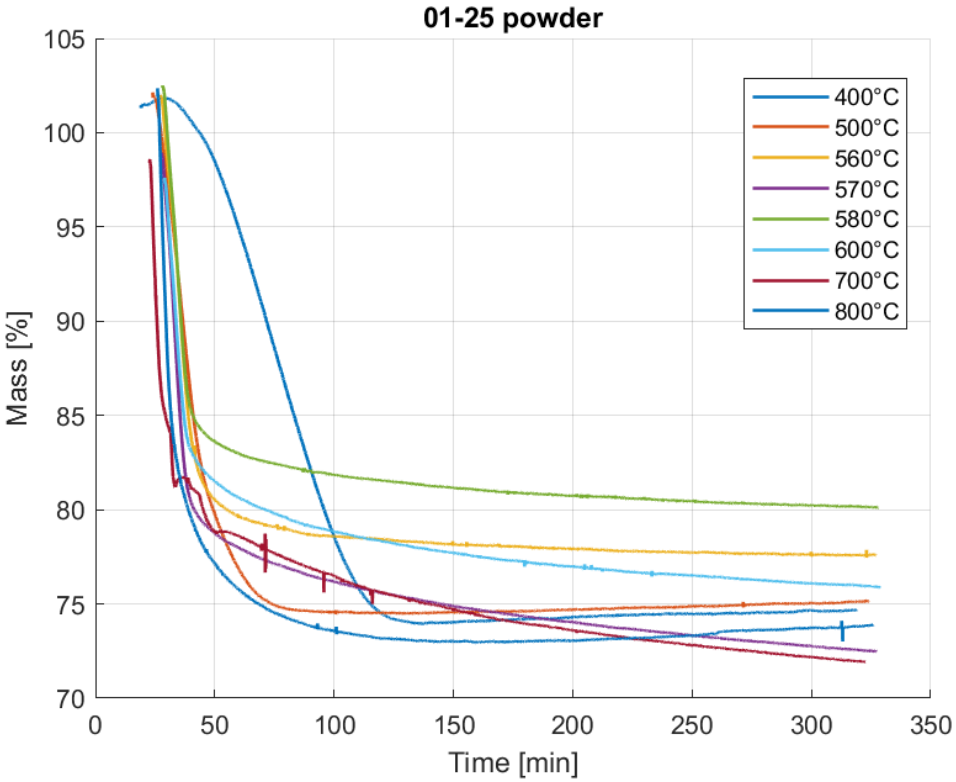


Figure 4.1: TGA plots for the 01/25 powder.

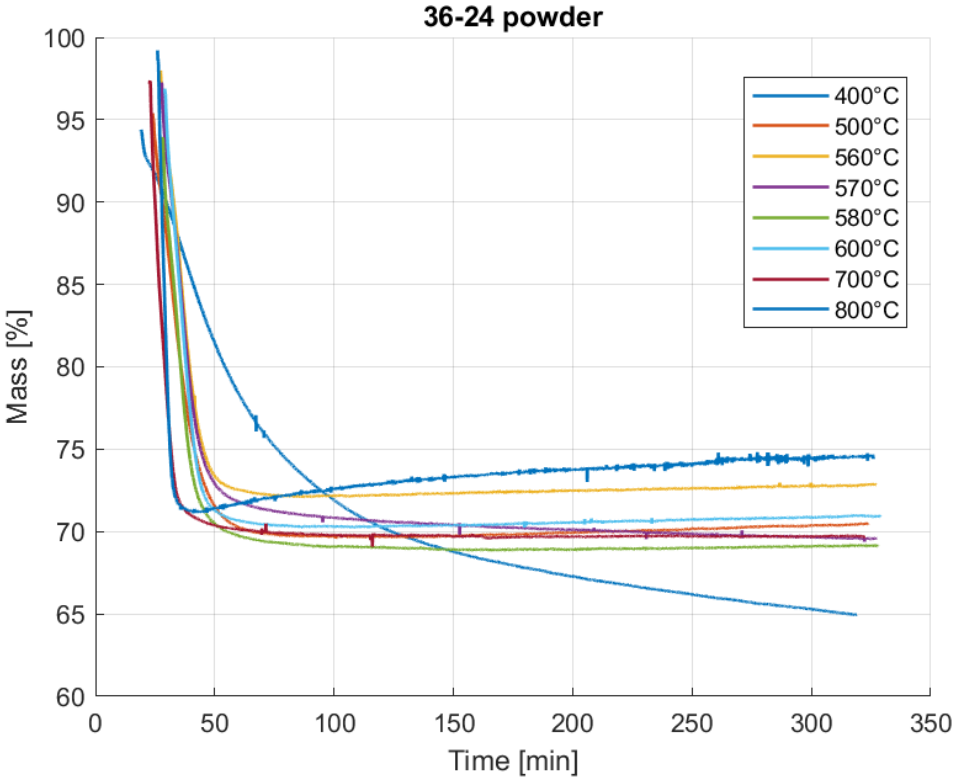


Figure 4.2: TGA plots for the 36/24 powder.

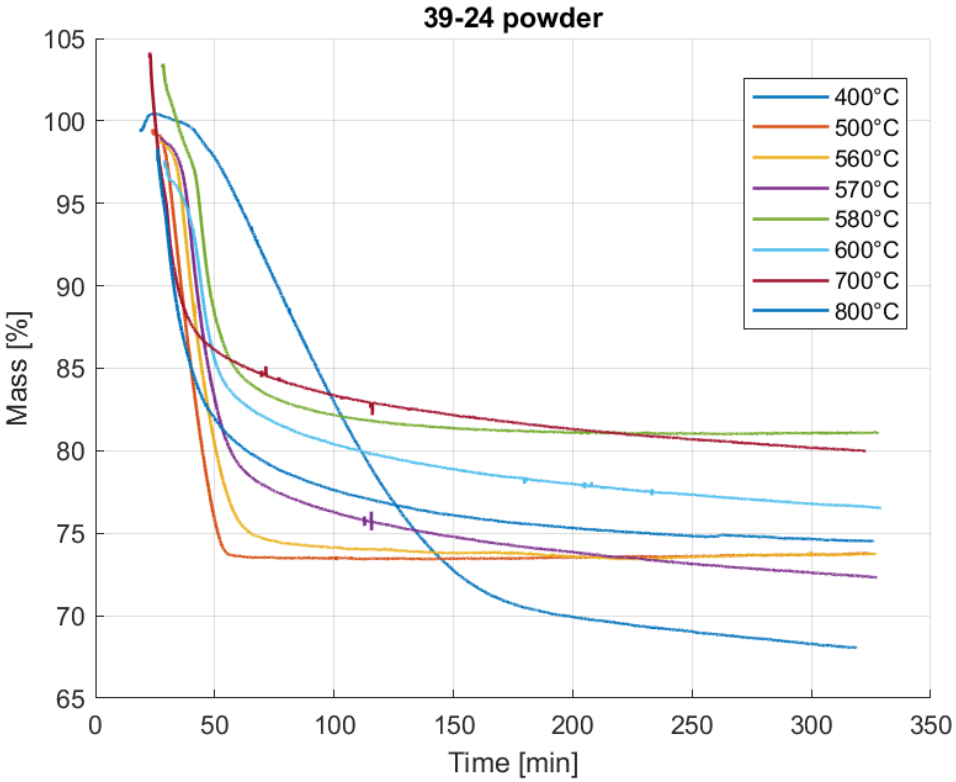


Figure 4.3: TGA plots for the 39/24 powder.

The results of the analysis for the mass loss and the t_{10} and t_{90} times are summarised in the next tables:

Temperature [°C]	**01-25** [%]	**36/24** [%]	**39-24** [%]
400	31.10	29.43	31.27
500	26.98	24.91	25.71
560	24.32	25.08	25.07
570	26.46	27.63	26.67
580	22.38	24.82	22.16
600	21.74	25.97	21.06
700	26.48	27.51	23.83
800	28.47	24.76	23.79
Average	25.99	26.26	24.94
St. dev.	3.11	1.74	3.14
% st. dev.	11.96%	6.61%	12.58%

Table 4.1: Mass loss of the samples, expressed as a percentile value of the initial mass.

Temperature [°C]	**01-25** [min]	**36/24** [min]	**39-24** [min]
400	30.25	6.7	37
500	4.4	1.45	6.5
560	2.35	1.3	11.2
570	2.05	4.25	9.65
580	1.85	0.75	4
600	1.5	0.95	7.05
700	1.2	0.9	1.4
800	0.9	0.7	1.6

Table 4.2: t_{10} times for the various powders at different temperatures, in minutes.

Temperature [°C]	**01-25** [min]	**36/24** [min]	**39-24** [min]
400	95.95	157.75	147.6
500	32	21.35	25.1
560	28.05	17.6	34.25
570	112.15	28.85	111.65
580	49.6	16.3	45.6
600	102.05	14.1	130.1
700	131.2	11.1	116.1
800	26.4	4.6	93.45

Table 4.3: t_{90} times for the various powders at different temperatures, in minutes.

While the TGA graphs may at first appear to indicate a variable weight loss among the samples, the corresponding calculations show that the mass loss remains relatively stable across the different experiments, including those conducted at reduced temperatures. This apparent discrepancy can be attributed primarily to the very small sample masses involved. Under such conditions, even minor variations arising from buoyant or aerodynamic forces can introduce measurable deviations in the recorded mass. Additionally, slight inconsistencies or intrinsic errors in the gas-flow control of the instrument may also contribute to a systematic offset when compared with the blank measurement. These combined effects likely account for the divergence between the visual impression provided by the graphs and the more stable results obtained through direct calculation.

The calculations indicate that the iron oxide undergoes complete oxidation, as the measured mass losses closely match the theoretical maximum expected for full conversion. By examining the average mass losses across the experiments, it can be inferred that the three investigated iron ores consist predominantly of magnetite (Fe_3O_4), which is characterized by a theoretical mass loss of approximately 27 %. The observed deviations from this value are likely attributable to the presence of foreign elements within the ores that may interfere with or partially hinder the reaction process. A detailed discussion of the nature and potential effects of these additional elements is provided in Chapter 3.4.5.

4.1.2 BET Results

Various models were employed to analyse the data and extract various types of information: the BET equation provided overall details about particle surfaces, while

mesopore characteristics (pores with diameters from 2 to 50 nm) were determined by averaging results from four distinct methods. Lastly, micropore analysis was conducted to gather information about pores with diameters below 2 nm.

Parameter	**01/25**	**36/24**	**39/24**
V_m [$cm^3(STP)g^{-1}$]	0.17815	1.206	0.1685
C [-]	140.06	49.167	119.39
d_{pores} [nm]	8.03695	7.95535	8.66805
$a_{s,BET}$ [m^2/g]	0.77539	5.2541	0.733395
V_{pores} [cm^3/g]	0.00155785	0.0104395	0.00158945

Table 4.4: Results from the BET plot anlysis.

V_p [cm^3/g]	0.001406063	0.01005875	0.001501613
a_p [m^2/g]	0.6656375	5.1503625	0.6103
r_p, peak [nm]	1.9675	2.9775	5.19625

Table 4.5: Results from the mesopores analysis, obtained by averaging the results from the BJH, CI, DH and INNES plots.

a_1 [m^2/g]	0.3918	2.9049	0.38495
a_2 [m^2/g]	1.3363	11.704	1.5346
V_p [cm^2/g]	-0.000474315	-0.00542735	-0.000726055
d_p, peak [nm]	0.9	0.9	0.9

Table 4.6: Results from the micropores analysis.

The adsorption/desorption analyses reveal clear and consistent differences between the three samples. The main outcomes are:

- the 36/24 powder has a substantially larger accessible surface area (by roughly one order of magnitude) than the other two samples;
- The lower C of 36/24 suggests weaker adsorbate-adsorbent interaction energy compared with the 01/25 and 39/24 powders, despite its larger surface area.
- Again,36/24 is much more porous in terms of accessible pore volume;
- The 39/24 powder has larger mesopores compared to the other two powders.

Taken together, the BET and mesopore results clearly identify the 36/24 powder as the most porous and highest surface area material among the three: it exhibits a significantly larger monolayer capacity, greater BET surface area and an order-of-magnitude higher mesopore volume and surface area. Physically, this implies that the 36/24 powder provides a larger gas-solid contact area per unit mass and more internal pore volume for gas transport and adsorption. Consequently, it is expected to display faster gas-solid reaction rates (per unit mass) and different mass-transfer

behaviour in reduction experiments relative to the other samples. The fact that the 36/24 powder tends toward larger mesopores and the others toward smaller mesopores, can influence diffusion resistances and capillary condensation phenomena.

The the micropore analysis present an internal inconsistency: the reported micropore surface area a_2 is non-negligible (notably large for the 36/24 powder), while the corresponding micropore volumes returned by the t-plot are slightly negative. Negative micropore volumes are typically an artifact that arises when the chosen reference isotherm or the t-curve is not perfectly appropriate for the sample, or when experimental noise and baseline corrections dominate the small micropore signal. Therefore, the t-plot outputs in the present dataset should be interpreted with caution since they do not provide rigorous evidence of substantial microporosity.

Because of this contradiction, one should not claim significant microporosity on the basis of these t-plot numbers alone.

Given its higher surface area and pore volume, the 36/24 powder is the sample most likely to show enhanced reactivity during hydrogen reduction. The increased surface area and internal porosity of the 36/24 powder may increase the effective interparticle contact area and the likelihood of cohesive behaviour (or higher entrainment of fines), potentially explaining anomalous fluidization characteristics observed for this powder. Larger internal pore volume and mesoporous structure will modify diffusion paths and could either facilitate or hinder overall gas transport depending on connectivity.

The CR powder was already analysed before the work for this thesis was done, but only the $a_{s,\mathrm{BET}}$ value was saved. It is equal to: 3.16185 m^2/g.

In addition to these results relative to the reduction behaviour of the powders, it is also possible to correlate the BET data with the minimum fluidization velocities of the powders.

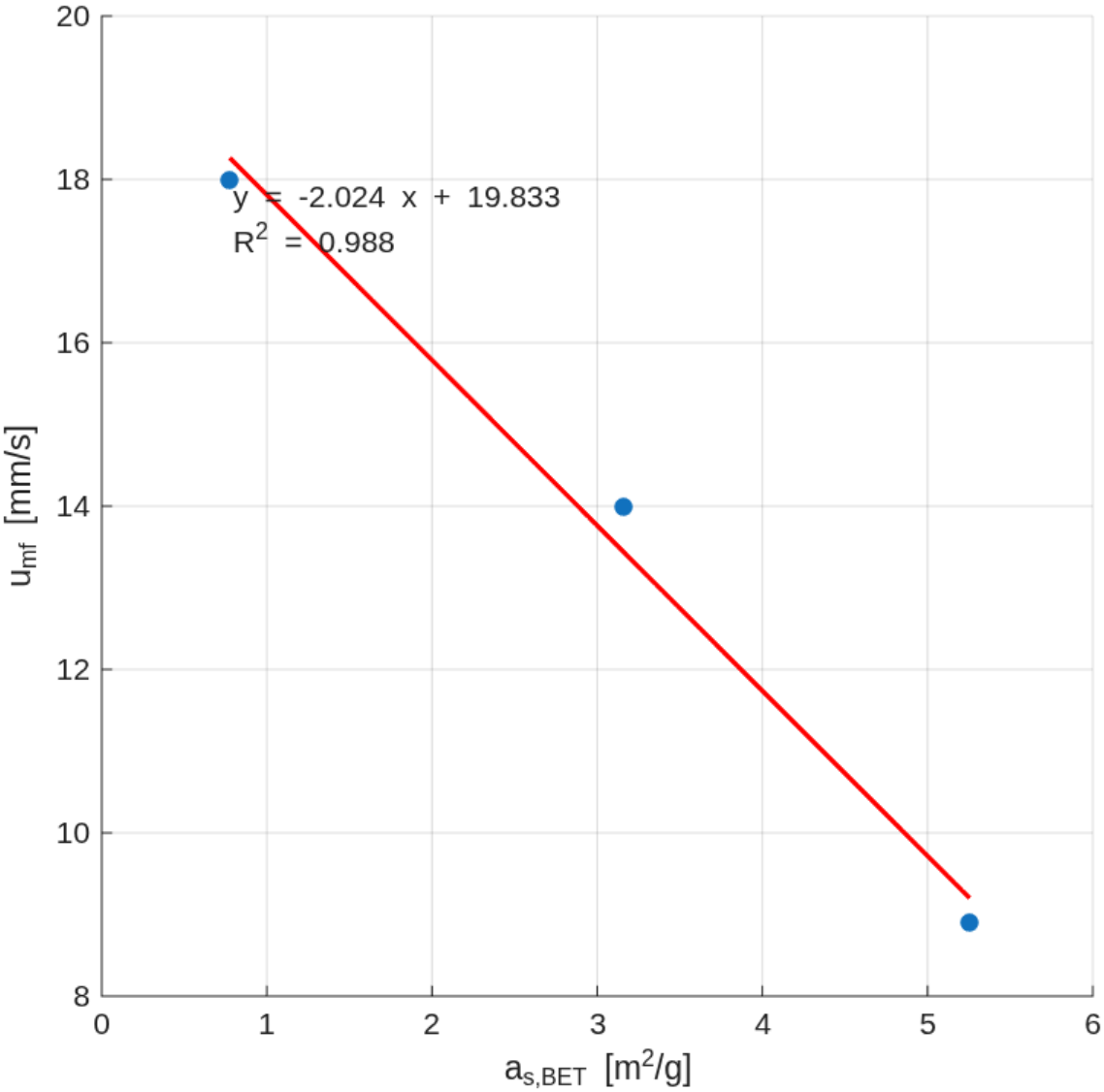


Figure 4.4: Correlation between the minimum fluidization velocity and the BET specific surface area

As we can see, there is a clear correlation between the two data sets: as the surface area increases, the minimum fluidization velocity decreases. This might be because more porous particles have a higher drag-to-weight ratio, meaning that the gas velocity needed to fluidise the particles is lower.

It is worthy to remember that with only three data points, even if the correlation seems good, it might just be an artifact, so more tests would be needed to create a clearer picture.

4.1.3 TGA compared to BET Results

The results obtained from the t_{10} analysis and the BET measurements were compared in order to investigate whether any of the BET-derived parameters could be used to predict the reduction behaviour of the particles. Since, from previous work conducted within the research group, both the t_{10} values from the 400 °C reductions in the TGA and the corresponding $a_{s,\mathrm{BET}}$ had already been determined, the newly acquired data were added to this existing dataset.

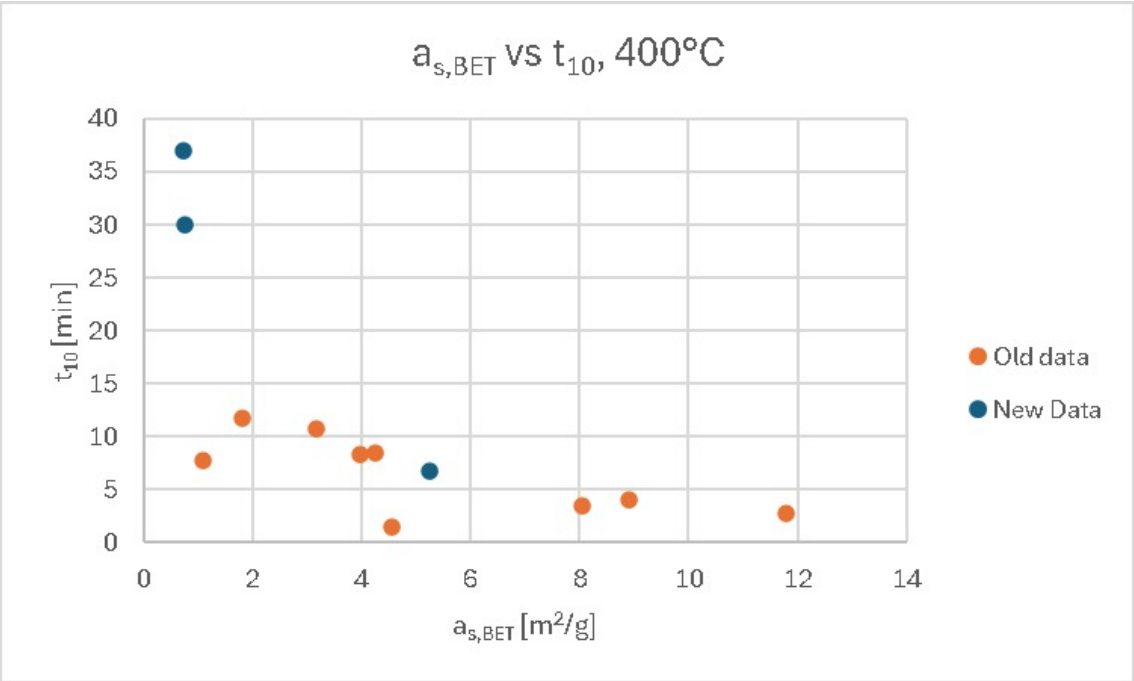


Figure 4.5: The new data is shown in blue, whereas the data from the previous research is in orange. Every point corresponds to a different material.

Among the new data, the point corresponding to the 36/24 powder aligns most closely with the previously obtained trend. As discussed earlier, this powder exhibits a higher specific surface area, whereas the 01/25 and 39/24 powders, which have a significantly lower $a_{s,\mathrm{BET}}$, show correspondingly longer reaction times.

When evaluating the previously studied laboratory-grade oxides in isolation, t_{10} appears to be largely independent of the specific surface area, showing no clear trend. Conversely, if only the newly tested iron ores are considered, a clear inverse relationship emerges, suggesting an exponential-type decay where a higher surface area drastically reduces the initial reaction time.

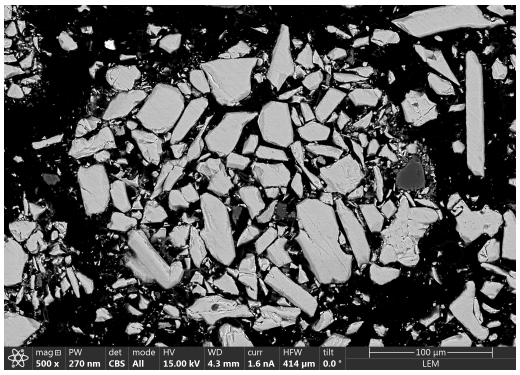
While both of these group-specific trends may be physically valid for their respective material categories, combining the datasets reveals that no single, universal correlation exists. This discrepancy clearly demonstrates that the reduction behaviour of an iron oxide sample cannot be universally predicted by relying solely on a single morphological parameter derived from BET analysis. It further confirms that other intrinsic factors must play a decisive role in the reaction kinetics.

Furthermore, attempting to fit a single exponential decay curve across all data points would be statistically misleading. This is clearly demonstrated by observing the behavior of the materials at very low specific surface areas. At these values, the high-purity laboratory oxides exhibit t_{10} times of approximately 10 minutes, whereas the raw iron ores take more than 30 minutes to reach the same reduction degree. Such a difference in reaction times for materials with similar surface areas proves that $a_{s,BET}$ is not a governing parameter in the reduction of iron oxides.

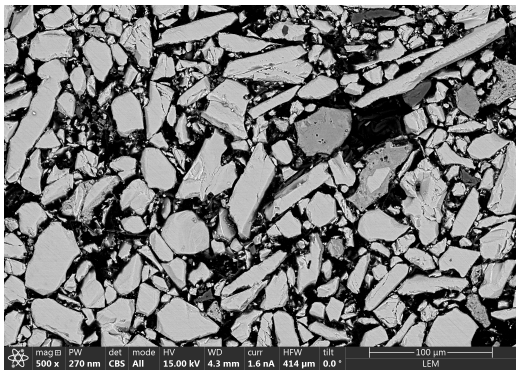
The BET data will instead be used as reference values to assess how the morphological properties of the particles evolve during high-temperature reduction in the furnace.

4.1.4 XRD Results

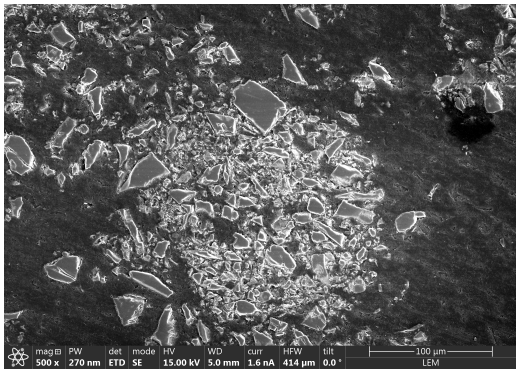
All the three iron ore powders from the company and the MP24 powder were studied using XRD. The photos that show the internal structure of the powders are shown below:



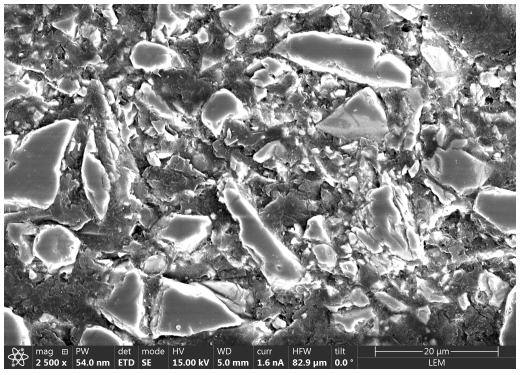
(a) 01/25 at 500x.



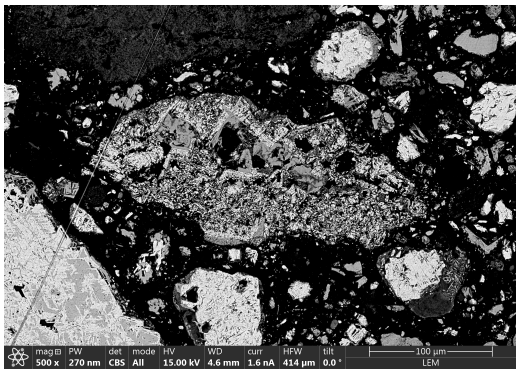
(b) 01/25 at 2500x.



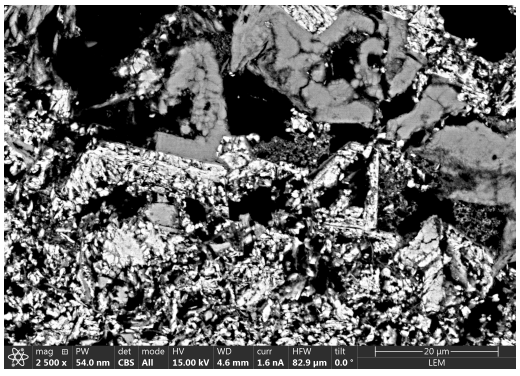
(c) 39/24 at 500x.



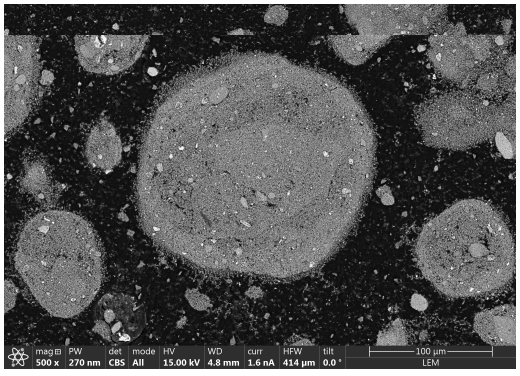
(d) 39/24 at 2500x.



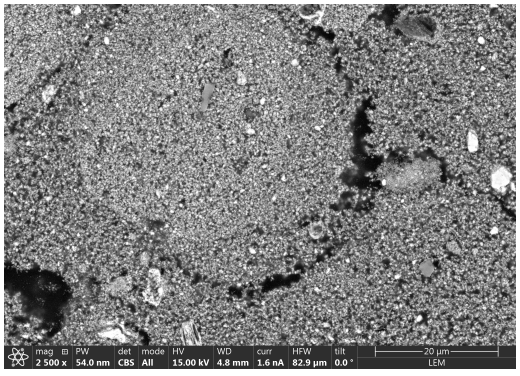
(e) 36/24 at 500x.



(f) 36/24 at 2500x.



(g) MP24 at 500x.



(h) MP24 at 2500x.

Figure 4.6: Comparison of images at 500x and 2500x of the various powders.

Figure 4.6 provides a visual record of the microstructural state of the various powders. The differences between them are key to diagnosing the success or failure of the reduction process and the quality of fluidization.

- Powder 01/25: the particles are formed by irregular and jagged structures, that are relatively big compared to those of the other powders shown here. We can see that the particles themselves do not present cavities inside. These characteristics are linked to the poor fluidization behaviour of the powder compared to the other ones (it was the one with the highest u_{mf});
- Powder 39/24: similarly to powder 01/25 it is a filled particle, with an irregular appearance, but the irregularities themselves are smaller compared to those of the 01/25 powder;
- Powder 36/24: the microstructure of the powder reflects accurately the results found with the BET analysis. The highly porous structure is visible. Different shades of gray are visible, which may indicate different phases inside of each particle. This aspect is explored more in depth in the section where the spectroscopy images are shown;
- MP24: the powder is formed by very round particles, that could not show much porosity, if at all. "Whiskers" are present on the surface of the particle, which might explain why the fluidization behaviour of this particle was not very good: these formations might act as hooks and get tangled with each other, increasing the gas flow necessary to obtain stable fluidization.

As discussed previously, powder 39/24 did not exhibit any fluidization behaviour. If only the XRD images had been considered, one might have inferred that powders 39/24 and 01/25 would display similar fluidization characteristics, which is clearly not the case. This observation highlights that, although X-ray diffraction is a valuable technique for obtaining preliminary insights into the microstructure of the particles, it should be regarded primarily as a qualitative visualization tool rather than a quantitative or predictive method for assessing fluidization behaviour.

4.1.5 Particle Size Distribution Results

By carefully reading the x-axis values at 10%, 50%, and 90% cumulative volume, we can tabulate the critical parameters:

	36/24	**39/24**	**01/25**	**CR**
x_{10} [μm]	4.09	3.18	7.61	5.7
x_{50} [μm]	73.615	19.925	31.65	79.955
x_{90} [μm]	312.215	48.825	68.64	200.72

Table 4.7: Diameters of the particles corresponding to the respective cumulative volume, in μm.

Since the diameter is directly correlated to the minimum fluidization velocity, we would expect the 39/24 powder to have the lowest fluidization velocity, followed

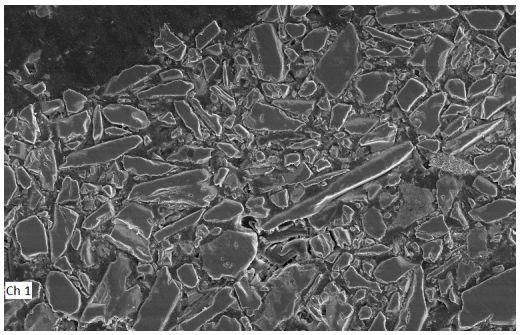
by the 01/25 and then the 36/24 and CR powders in the end. As we have said previously the 39/24 powder was not able to fluidize at all, and the 01/25 powder has the highest minimum fluidization velocity. the 36/24 and CR powders show a similar fluidization velocity, as we might have expected, but it is lower compared to the 01/25 powder. Several factors can account for these discrepancies.

Particle size alone does not completely determine u_{mf}: particle density, shape (through sphericity), surface roughness and internal porosity all influence the effective drag and the apparent weight of the particles and hence the fluidization threshold. In particular, a larger bulk (or tapped) density for the same bed volume increases the bed mass and the required pressure drop, leading to higher u_{mf}. Cohesive forces and a high fines fraction can also raise the apparent minimum fluidization velocity or even prevent fluidization by forming agglomerates or by clogging interstitial pores: a plausible explanation for the non-fluidizing behaviour of the 39/24 powder. Other contributing effects include non-uniform packing or wall interactions (local compaction, channeling), imperfect gas distribution at the distributor, and experimental artefacts (such as residual moisture and electrostatic charging).

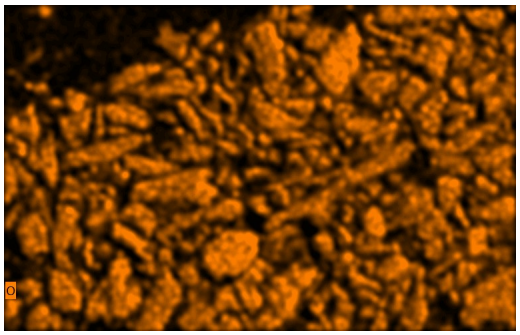
From a practical viewpoint, the similarity between36/24 and CR suggests these materials are mutually comparable for subsequent reduction tests. Conversely, the anomalous behaviour of 39/24 and the unexpectedly large u_{mf} of 01/25 indicate that granulometry alone is insufficient to set reliable operating flows.

4.1.6 Electron Spectroscopy Imaging

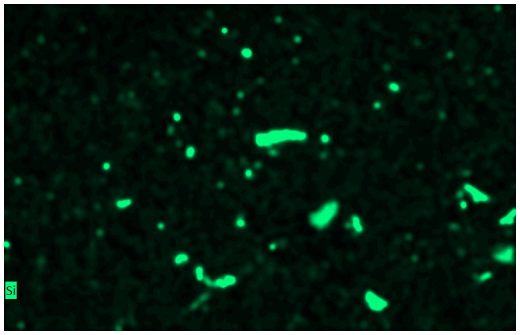
The images that show the different elements in the various powders are shown below in figure 4.7.



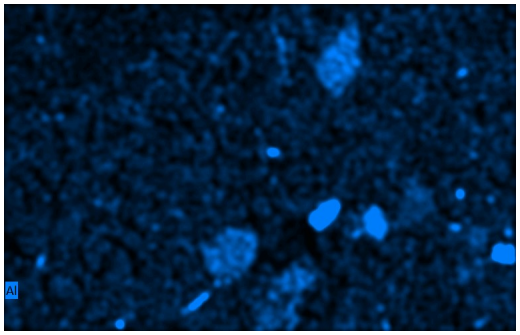
(a) Detail of one 01/25 particle.



(b) Oxygen content.



(c) Silicon content.



(d) Aluminum content.

Figure 4.7: Pictures for the 01/25 powder.

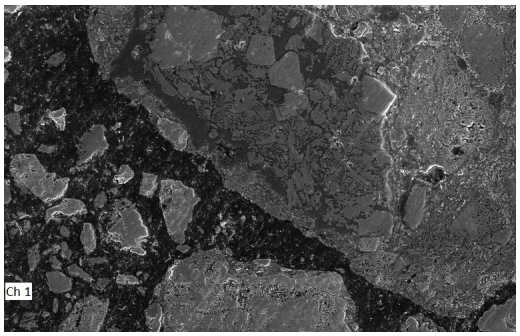
We can see from the pictures how the oxygen is not evenly distributed between the various parts of the particle. This indicates that more than one phase of iron oxide might be present, or that various other trace elements are not evenly distributed throughout the particles.

We can also see how silicon appears to be very segregated, as it appears to be very localised. This might be due to contaminations from the machines that interacted with the particles before coming to the lab (like crushing and sieving).

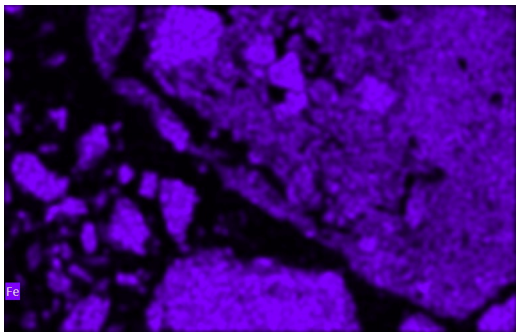
Aluminum is more spread out throughout the sample compared to the silicon, but it is also localised and more concentrated in some structures compared to others. This might be from the presence of alumina (Al_2O_3), a mineral that might still be present from the mining of the ore.

A more in-depth analysis of the possible origins of various elements and minerals is given in chapter 4.1.8.

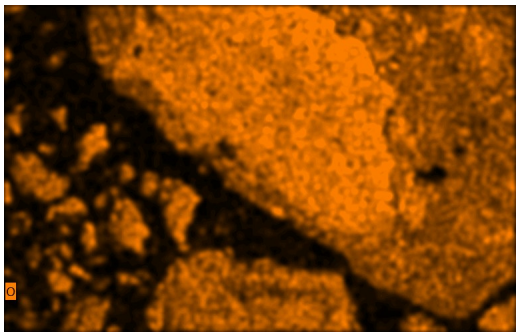
Concerning powder 36/24, the results are depicted in figure 4.8.



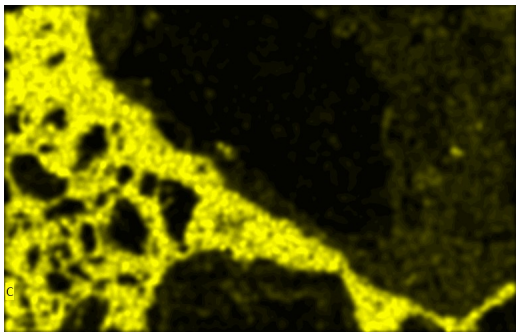
(a) Detail of 36/24 powder.



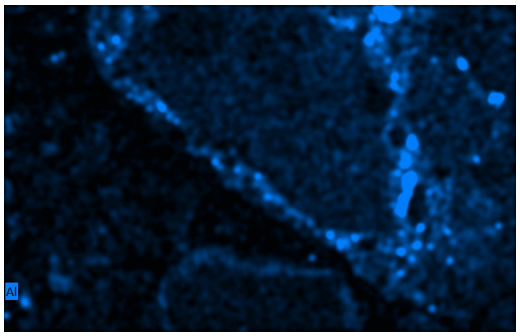
(b) Iron content.



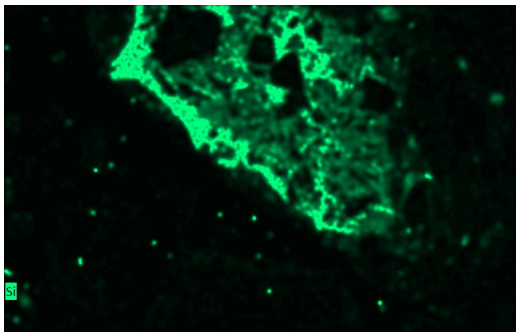
(c) Oxygen content



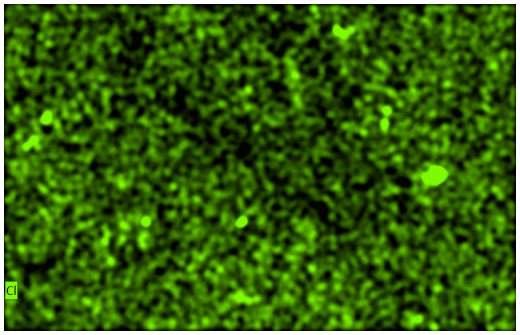
(d) Carbon content



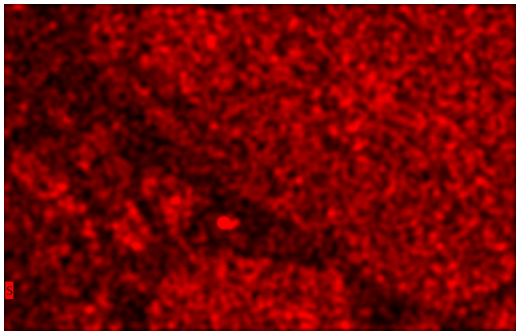
(e) Aluminum content



(f) Silicon content.



(g) Chlorine content.



(h) Sulphur content.

Figure 4.8: Pictures for the 36/24 powder.

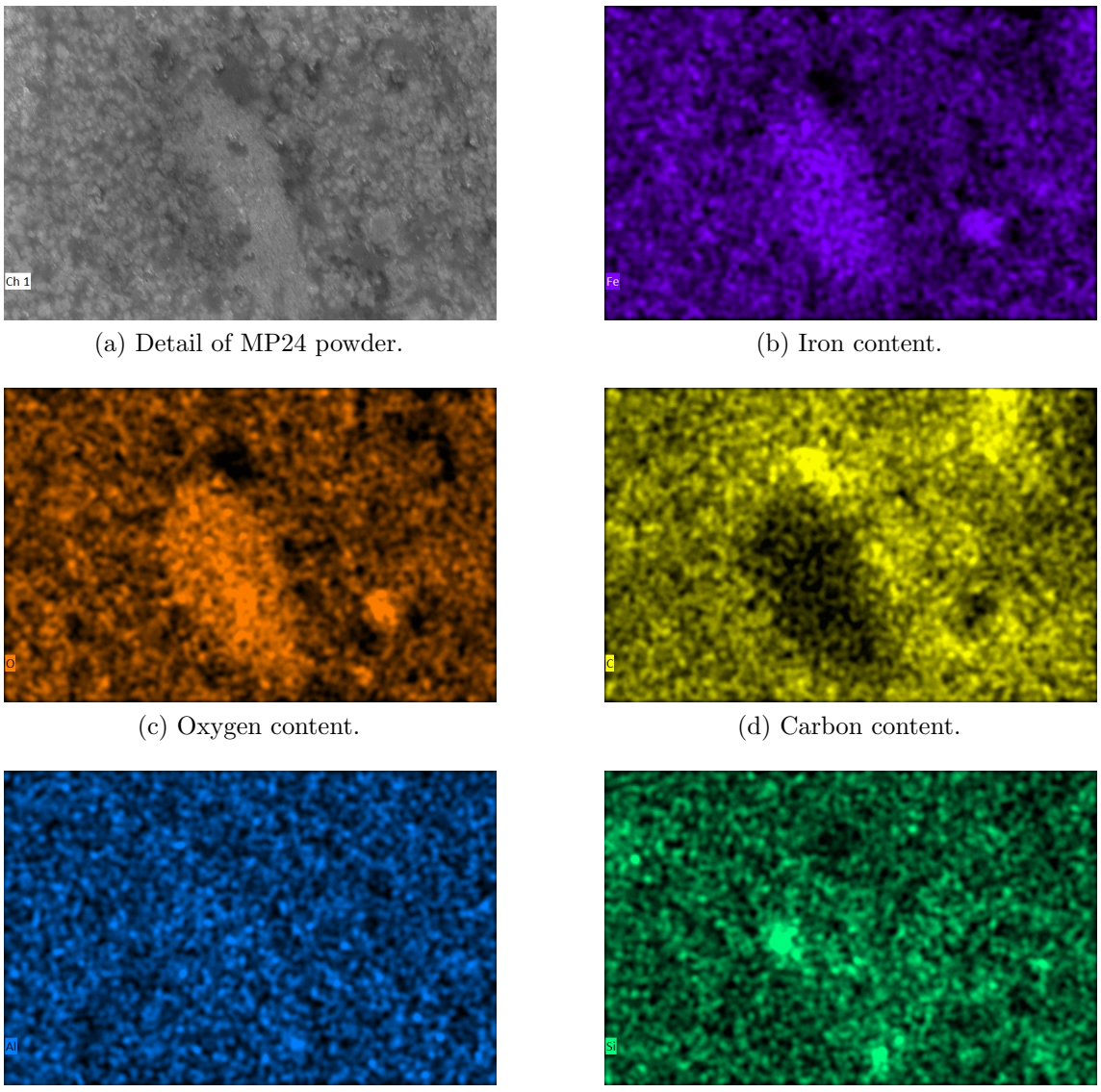
As we can see from the Fe and O images, we probably have different iron oxide phases in this powder too. In the carbon image we can see that, while a lot of carbon is present in the matrix that holds the particle during the imaging, some carbon is

also present in the particles themselves, and, like iron and oxygen, it is not uniformly distributed.

Like for the 01/25 powder, for the 36/24 powder there are also trace presences of aluminum and silicon, again probably from the mining manufacturing of the powders themselves.

Lastly, small traces of chlorine and sulphur are present.

The last powder is the MP24 powder, whose results are depicted in figure 4.9.



(a) Detail of MP24 powder.

(b) Iron content.

(c) Oxygen content.

(d) Carbon content.

(e) Aluminum content.

(f) Silicon content.

Figure 4.9: Pictures for the MP24 powder.

Compared to the previously analysed powders, the iron content appears to be more uniformly distributed; however, localized regions with higher concentrations of iron and oxygen are still visible. This could be attributed to the presence of different phases, but it may also result from artifacts related to image acquisition. As suggested by the carbon distribution map, which highlights the areas where the

substrate supporting the particles is exposed, the regions where carbon is visible coincide with those where iron oxide is absent.

4.1.7 Optical Emission Spectroscopy

The optical emission spectroscopy (OES) analysis was carried out externally; therefore, only the results are presented in figure 4.10. The analysis was performed exclusively on the three iron ore powders supplied by the company.

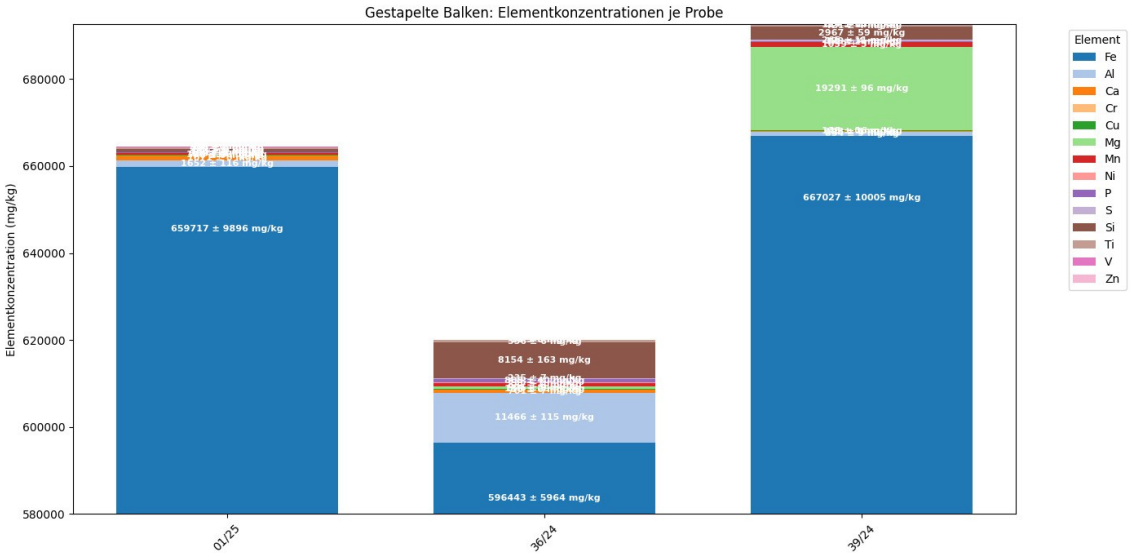


Figure 4.10: Concentration of elements inside of the three iron ores.

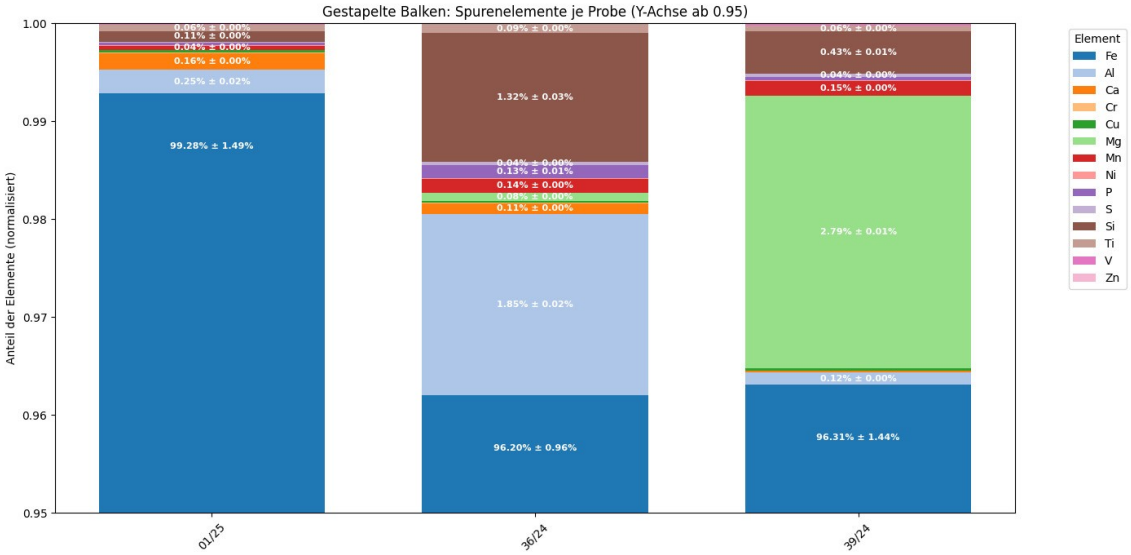


Figure 4.11: Percentages of elements inside of the three iron ores, con asse y dal 95%.

While figures 4.10 and 4.11 provides an immediate visual representation of the overall composition, the formatting of the externally provided graph makes it difficult to extract precise numerical values. To ensure clarity, the exact mass concentrations of the most relevant elements have been extracted and tabulated. Tables 4.8 and 4.9

summarizes these values, highlighting the primary compositional differences among the three iron ore samples.

Element	01/25 [mg/kg]	36/24 [mg/kg]	39/24 [mg/kg]
Fe	659717 ± 9896	596443 ± 5964	667027 ± 10005
Al	1652 ± 116	11466 ± 115	Traces
Si	Traces	8154 ± 163	2967 ± 59
Mg	Traces	Traces	19291 ± 96

Table 4.8: Concentrations of the main elements obtained from the ICP-OES analysis. Due to the limited legibility of the labels in the externally provided graph (Figure 4.10), the exact numerical values for the most relevant species are reported here.

Element	01/25 [%]	36/24 [%]	39/24 [%]
Fe	99.28 ± 1.49	96.20 ± 0.96	96.31 ± 1.44
Al	0.25 ± 0.02	1.85 ± 0.02	0.12 ± 0.00
Si	0.11 ± 0.00	1.32 ± 0.03	0.43 ± 0.01
Mg	Traces	0.08 ± 0.00	2.79 ± 0.01
Ca	0.16 ± 0.00	0.11 ± 0.00	Traces
Mn	Traces	0.14 ± 0.00	0.15 ± 0.00

Table 4.9: Percentages of the main elements obtained from the ICP-OES analysis.

The two charts provide complementary perspectives: figure 4.10 reports the absolute concentrations, whereas figure 4.11 highlights the relative proportions. The elemental composition of the powders is dominated by iron, as expected for iron ores, accompanied by smaller quantities of other major and trace elements.

The 01/25 and 39/24 powders exhibit the highest and nearly identical iron content by weight, approximately 660 g/kg, while the 36/24 powder shows a slightly lower value ($\approx$ 590 g/kg). When considering the foreign elements, the 36/24 and 39/24 powders display notably higher levels compared to the 01/25 powder. Specifically, 36/24 contains detectable amounts of silicon and Aluminum, consistent with the EDS results discussed in the previous section, whereas 39/24 presents a relatively large amount of magnesium. This discrepancy with the prior analysis can be explained by two possible factors:

- The magnesium peak in the EDS spectrum, while it could have still showed up in the analysis, may have been overlapped or masked by other elemental peaks, leading to its omission during analysis;
- The localised nature of EDS means that the analysed region might not have contained magnesium, even though it is present elsewhere in the sample.

These findings highlight the importance of employing multiple complementary analytical techniques, both to validate results and to identify potential inconsistencies between methods.

Finally, the normalized data in Figure 4.11 reveals that the 01/25 powder is considerably purer than the other two, with trace elements accounting for less than 1 % of the total composition.

The 36/24 powder once again exhibits non-negligible concentrations of Aluminum and silicon, confirming the results obtained both from the weight concentration data and from the previous electron spectroscopy analyses. The consistent detection of these two elements across different analytical techniques reinforces the hypothesis that they are not surface contaminants but are instead structurally incorporated within the mineral matrix of the ore. Their presence is particularly relevant, as Aluminum and silicon oxides are known to form complex silicate or aluminosilicate phases with iron oxides, which can influence both the reduction kinetics and the mechanical stability of the particles during high-temperature processing.

The 39/24 powder, on the other hand, contains minor traces of silicon and a significant magnesium content of nearly 3%. The appearance of magnesium, which was not clearly detected in the previous electron microscopy analyses, suggests that it may be distributed heterogeneously within the sample, possibly concentrated in specific mineral inclusions or phases.

4.1.8 Foreign Elements in the Powders

The presence of foreign elements in iron ores can significantly influence their reduction behaviour, fluidization characteristics, and overall performance in high-temperature processes. The elemental analyses conducted via ICP-OES and electron spectroscopy (see sections 4.1.6 and 4.1.7) confirmed that the three iron ore powders supplied by the company contain not only iron but also detectable amounts of Aluminum (Al), silicon (Si), magnesium (Mg), and manganese (Mn), among other trace elements.

The origin of these elements can be attributed to both natural and processing-related sources.

4.1.8.1 Aluminum

Aluminum is often found substituted within the crystal structure of iron oxides such as hematite and goethite, or present in gangue minerals like aluminosilicates (e.g., kaolinite). In commercial iron ores, the Al_2O_3 content is typically kept below 4% [53]. Its presence in the analysed powders, particularly in the 36/24 sample, is consistent with natural incorporation during ore formation, though contamination from refractory materials during processing cannot be entirely ruled out.

The repeated detection of Aluminum and silicon in sample 36/24 (and, to a lesser extent, in sample 01/25) suggests that these elements are structurally incorporated within the material rather than being present merely as superficial contaminants. Aluminum can form corundum phases (crystalline Al_2O_3) inside of iron oxides [54], that form spinel-like structures during their reduction [55], which can affect the reduction behaviour of the particles. Such structural modifications may account for the slightly shorter t_{10} and t_{90} times observed for these powders when compared with sample 39/24.

However, this correlation does not fully account for all results obtained from the TGA experiments (for example, the longer t_{90} time recorded for the 36/24 powder at

400 °C). This clearly indicates that, if the incorporation of these elements is indeed influencing the reduction behaviour, additional effects must also be contributing to the observed trends.

4.1.8.2 Silicon

Silicon is commonly associated with quartz and other silicate minerals that constitute the gangue material in iron ore deposits. It may appear as discrete inclusions or finely dispersed within the ore matrix. During beneficiation (any process that improves the economic value of the ore by removing the gangue), a portion of silica is removed, but residual amounts often persist. The SiO_2 content in commercial ores is generally limited to less than 6% [53], which aligns with the moderate levels detected in the 36/24 and 39/24 powders.

Silicon, when added to iron ores, has been shown to produce high purity Fe domains surrounded by a slag matrix [56]. Similar effects may also have occurred during the reduction experiments performed in this work. However, it remains unclear whether such effects would be beneficial or detrimental to the overall reduction behaviour. If a slag phase is present (and particularly if it forms in combination with other elements or interacts with the additional effects discussed previously) it could either impede or facilitate further reduction. Moreover, the presence of such a phase could likewise influence the fluidisation properties of the powder, again in ways that are not straightforward to predict. Consequently, while the formation of these phases cannot be ruled out, their net impact on the system remains uncertain.

4.1.8.3 Magnesium

Magnesium was notably present in the 39/24 powder, likely originating from silicate minerals such as serpentine or carbonates like magnesite. In some iron-making processes, MgO is intentionally added to improve slag fluidity and desulphurisation in blast furnaces [17]. Its heterogeneous distribution, as suggested by the discrepancy between EDS and ICP-OES results, indicates localized mineral inclusions rather than uniform contamination.

These local inclusions can decrease local particle density (since the density of Mg is approximately one fifth that of iron oxide, and the density of MgO is about two thirds of it) and might affect the local fluidization ability of the particles, which could explain the inability of the powder to fluidise.

A research ([57]) has additionally showed how the inclusion of magnesium in iron oxides can help prevent sintering at higher temperatures (by reducing the surface viscosity of the particles during reduction), meaning that if the inability of this powder to fluidize could be solved it could prove valuable in further experiments.

4.1.8.4 Manganese

Manganese was detected in minor amounts, likely as an impurity within the iron oxide matrix or as part of manganiferous mineral phases naturally occurring in the ore deposit.

4.1.8.5 Other effects

In some cases, elements such as Al and Fe can combine to form complex spinel structures like hercynite ($FeAl_2O_4$), which may influence the reducibility and sintering behaviour of the ore at high temperatures [58][59].

The observed elemental profiles are consistent with typical iron ore compositions reported in the literature. For instance, studies on magnetite-hematite ores from the Mikhaillovskoye deposit show similar ranges of Si and Al content in iron oxides (see Table 3 in [60]), supporting the conclusion that these elements are intrinsic to the ore rather than solely the result of external contamination.

Understanding the source and distribution of these foreign elements is essential for interpreting the reduction kinetics and fluidization performance of the powders, as they can alter phase stability, pore structure development, and interparticle forces during processing.

4.2 Fluidization Results

4.2.1 Theoretical Results

The following table summarizes the results obtained from the minimum fluidization velocity theoretical calculations performed using different correlations and cumulative particle size distributions. For each powder and operating temperature, the table reports the predicted minimum fluidization velocities, their average values, standard deviations, and corresponding percentage errors. This comparison allows for the evaluation of the consistency among the different models and provides insight into how temperature and particle characteristics influence the onset of fluidization.

Powder	**Temperature** [°C]	**Particle size**	**Eq. 2.15** [m/s]	**Eq. 2.13** [m/s]	**Eq. 2.14** [m/s]	**Average**	**St. dev.**	**% st. dev.**
01/25	20	x_{10}	$8.25 \cdot 10^{-5}$	$1.03 \cdot 10^{-4}$	$1.04 \cdot 10^{-4}$	$9.62 \cdot 10^{-5}$	$9.74 \cdot 10^{-6}$	10.12%
		x_{50}	$1.43 \cdot 10^{-3}$	$1.78 \cdot 10^{-3}$	$1.79 \cdot 10^{-3}$	$1.66 \cdot 10^{-3}$	$1.68 \cdot 10^{-4}$	10.12%
		x_{90}	$6.71 \cdot 10^{-3}$	$8.35 \cdot 10^{-3}$	$8.42 \cdot 10^{-3}$	$7.83 \cdot 10^{-3}$	$7.93 \cdot 10^{-4}$	10.13%
	500	x_{10}	$1.13 \cdot 10^{-3}$	$9.10 \cdot 10^{-5}$	$9.17 \cdot 10^{-5}$	$4.37 \cdot 10^{-4}$	$4.89 \cdot 10^{-4}$	111.87%
		x_{50}	$4.82 \cdot 10^{-3}$	$1.57 \cdot 10^{-3}$	$1.59 \cdot 10^{-3}$	$2.66 \cdot 10^{-3}$	$1.53 \cdot 10^{-3}$	57.41%
		x_{90}	$1.25 \cdot 10^{-2}$	$7.40 \cdot 10^{-3}$	$7.46 \cdot 10^{-3}$	$9.12 \cdot 10^{-3}$	$2.39 \cdot 10^{-3}$	26.20%
	600	x_{10}	$2.20 \cdot 10^{-3}$	$8.39 \cdot 10^{-5}$	$8.45 \cdot 10^{-5}$	$7.90 \cdot 10^{-4}$	$9.98 \cdot 10^{-4}$	126.35%
		x_{50}	$8.55 \cdot 10^{-3}$	$1.45 \cdot 10^{-3}$	$1.46 \cdot 10^{-3}$	$3.82 \cdot 10^{-3}$	$3.34 \cdot 10^{-3}$	87.53%
		x_{90}	$1.96 \cdot 10^{-2}$	$6.82 \cdot 10^{-3}$	$6.87 \cdot 10^{-3}$	$1.11 \cdot 10^{-2}$	$6.01 \cdot 10^{-3}$	54.14%
36/24	20	x_{10}	$2.38 \cdot 10^{-5}$	$2.97 \cdot 10^{-5}$	$2.99 \cdot 10^{-5}$	$2.78 \cdot 10^{-5}$	$2.81 \cdot 10^{-6}$	10.12%
		x_{50}	$7.71 \cdot 10^{-3}$	$9.61 \cdot 10^{-3}$	$9.69 \cdot 10^{-3}$	$9.00 \cdot 10^{-3}$	$9.12 \cdot 10^{-4}$	10.13%
		x_{90}	$1.32 \cdot 10^{-1}$	$1.65 \cdot 10^{-1}$	$1.74 \cdot 10^{-1}$	$1.57 \cdot 10^{-1}$	$1.80 \cdot 10^{-2}$	11.44%
	500	x_{10}	$6.33 \cdot 10^{-4}$	$2.63 \cdot 10^{-5}$	$2.65 \cdot 10^{-5}$	$2.29 \cdot 10^{-4}$	$2.86 \cdot 10^{-4}$	125.11%
		x_{50}	$1.37 \cdot 10^{-2}$	$8.51 \cdot 10^{-3}$	$8.58 \cdot 10^{-3}$	$1.03 \cdot 10^{-2}$	$2.45 \cdot 10^{-3}$	23.85%
		x_{90}	$1.40 \cdot 10^{-1}$	$1.52 \cdot 10^{-1}$	$1.54 \cdot 10^{-1}$	$1.49 \cdot 10^{-1}$	$1.66 \cdot 10^{-4}$	4.14%
	600	x_{10}	$1.25 \cdot 10^{-3}$	$2.42 \cdot 10^{-5}$	$2.44 \cdot 10^{-5}$	$4.348 \cdot 10^{-4}$	$5.79 \cdot 10^{-4}$	133.50%
		x_{50}	$2.12 \cdot 10^{-2}$	$7.85 \cdot 10^{-3}$	$7.91 \cdot 10^{-3}$	$1.23 \cdot 10^{-2}$	$6.30 \cdot 10^{-3}$	51.08%
		x_{90}	$1.56 \cdot 10^{-1}$	$1.40 \cdot 10^{-1}$	$1.42 \cdot 10^{-1}$	$1.46 \cdot 10^{-1}$	$7.02 \cdot 10^{-3}$	4.80%
CR	20	x_{10}	$4.63 \cdot 10^{-5}$	$5.76 \cdot 10^{-5}$	$5.81 \cdot 10^{-5}$	$5.40 \cdot 10^{-5}$	$5.46 \cdot 10^{-6}$	10.12%
		x_{50}	$9.10 \cdot 10^{-3}$	$1.13 \cdot 10^{-2}$	$1.14 \cdot 10^{-2}$	$1.06 \cdot 10^{-2}$	$1.08 \cdot 10^{-3}$	10.14%
		x_{90}	$5.66 \cdot 10^{-2}$	$7.05 \cdot 10^{-2}$	$7.20 \cdot 10^{-2}$	$6.64 \cdot 10^{-2}$	$6.93 \cdot 10^{-3}$	10.45%
	500	x_{10}	$8.61 \cdot 10^{-4}$	$5.10 \cdot 10^{-5}$	$5.14 \cdot 10^{-5}$	$3.21 \cdot 10^{-4}$	$3.82 \cdot 10^{-4}$	118.85%
		x_{50}	$1.54 \cdot 10^{-2}$	$1.00 \cdot 10^{-2}$	$1.01 \cdot 10^{-2}$	$1.19 \cdot 10^{-2}$	$2.51 \cdot 10^{-3}$	21.20%
		x_{90}	$6.46 \cdot 10^{-2}$	$6.31 \cdot 10^{-2}$	$6.38 \cdot 10^{-2}$	$6.38 \cdot 10^{-2}$	$5.99 \cdot 10^{-4}$	0.94%
	600	x_{10}	$1.69 \cdot 10^{-3}$	$4.70 \cdot 10^{-5}$	$4.74 \cdot 10^{-5}$	$5.95 \cdot 10^{-4}$	$7.75 \cdot 10^{-4}$	130.21%
		x_{50}	$2.34 \cdot 10^{-2}$	$9.26 \cdot 10^{-3}$	$9.33 \cdot 10^{-3}$	$1.40 \cdot 10^{-2}$	$6.654 \cdot 10^{-3}$	47.52%
		x_{90}	$7.89 \cdot 10^{-2}$	$5.82 \cdot 10^{-2}$	$5.88 \cdot 10^{-2}$	$6.53 \cdot 10^{-2}$	$9.63 \cdot 10^{-3}$	14.74%

Table 4.10: Predicted minimum fluidization velocities based on the different theoretical equations, with the average, the standard deviation and the standard deviation as a percentage of the average for the calculated velocities.

The parameter x_y denotes the characteristic particle diameter corresponding to the y-th percentile of the cumulative particle size distribution, i.e. the diameter below which $y\%$ of the particles in the sample are smaller. This representation provides a standardized way to compare the particle size characteristics of different powders and is discussed more in depth in chapter 3.4.6.

At ambient temperature, the predicted minimum fluidization velocities obtained from the different correlations show excellent agreement across all particle size classes, and this level of consistency remains nearly constant for the various diameters considered.

As the temperature increases, the agreement between correlations decreases: results at 500 °C show smaller relative deviations compared to those at 600 °C, but are in both cases higher compared to the ambient temperature. Moreover, in both temperature conditions, an increase in the particle diameter corresponds to a reduction in the normalized standard deviation, indicating a more stable prediction for coarser particles.

The best overall agreement among correlations is observed at 500 °C for the x_{90} particle class. It can also be noted that the correlations from equations 2.13 and 2.14 yield very similar results, consistent with the fact that the latter is an approximation of the former, whereas the predictions from equation 2.15 deviate more significantly from the other two.

It is important to note that these results originate from a purely theoretical comparison of the selected correlations, without direct experimental validation. Consequently, the observed trends should not be interpreted as evidence of actual physical behaviour, but rather as mathematical outcomes of how each correlation is formulated. The higher consistency observed for larger particle diameters or intermediate temperatures likely arises from the structure of the equations themselves, such as the way dimensionless parameters like the Reynolds and Archimedes numbers enter the correlations. Similarly, the increased deviation at higher temperatures could be the result of compounded numerical effects rather than genuine thermophysical phenomena.

Nonetheless, these findings are still valuable, as they highlight the range of applicability and internal coherence of the different models. The close agreement between the models at low temperature suggest they might have all been derived from low-temperature studies on the fluidization of various systems, whereas the very good agreement at higher diameters and temperatures is probably only due to a purely mathematical and coincidental convergence of the various models.

Overall, this theoretical comparison provides a useful reference for assessing which correlations yield consistent predictions under the specific conditions relevant to this study, before moving on to experimental validation.

4.2.2 Experimental Results

Initially, the various powders were tested to determine whether or not they could fluidize. These preliminary tests did not include pressure-drop measurements, as their sole purpose was to assess fluidization capability.

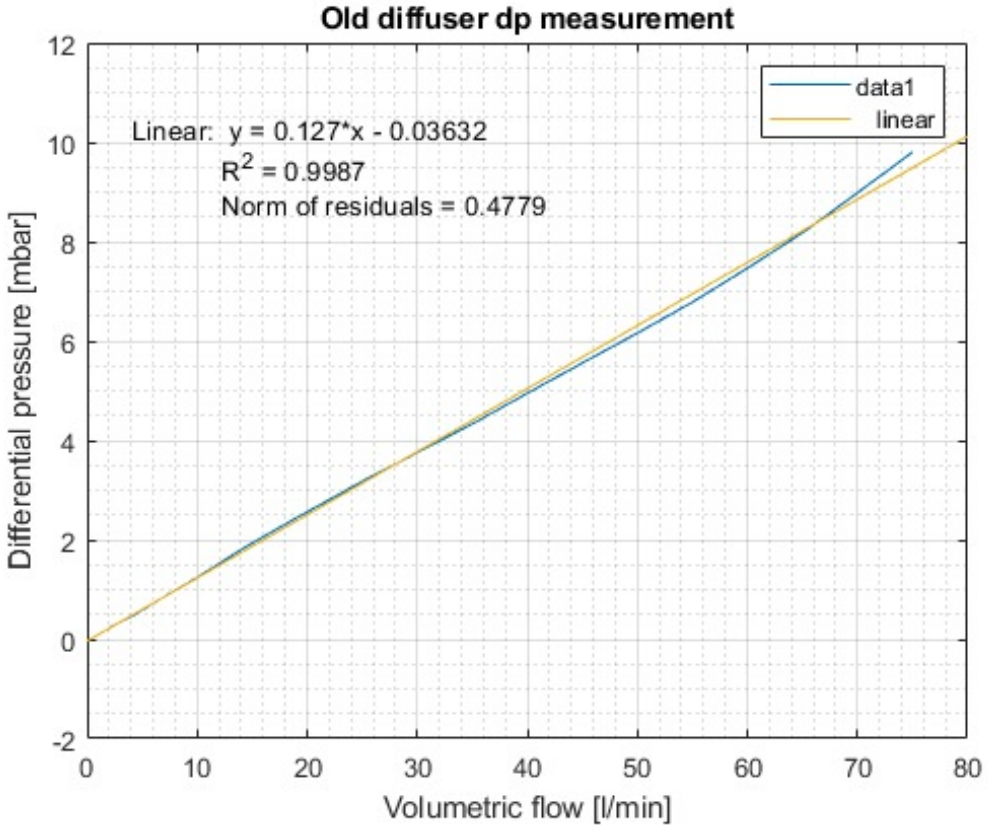
While the MP24 powder was able to fluidize, it exhibited poor fluidization quality: bubbles remained small and the minimum fluidization velocity was comparatively

higher. For this reason, it was not used in the differential pressure measurements or the high-temperature experiments.

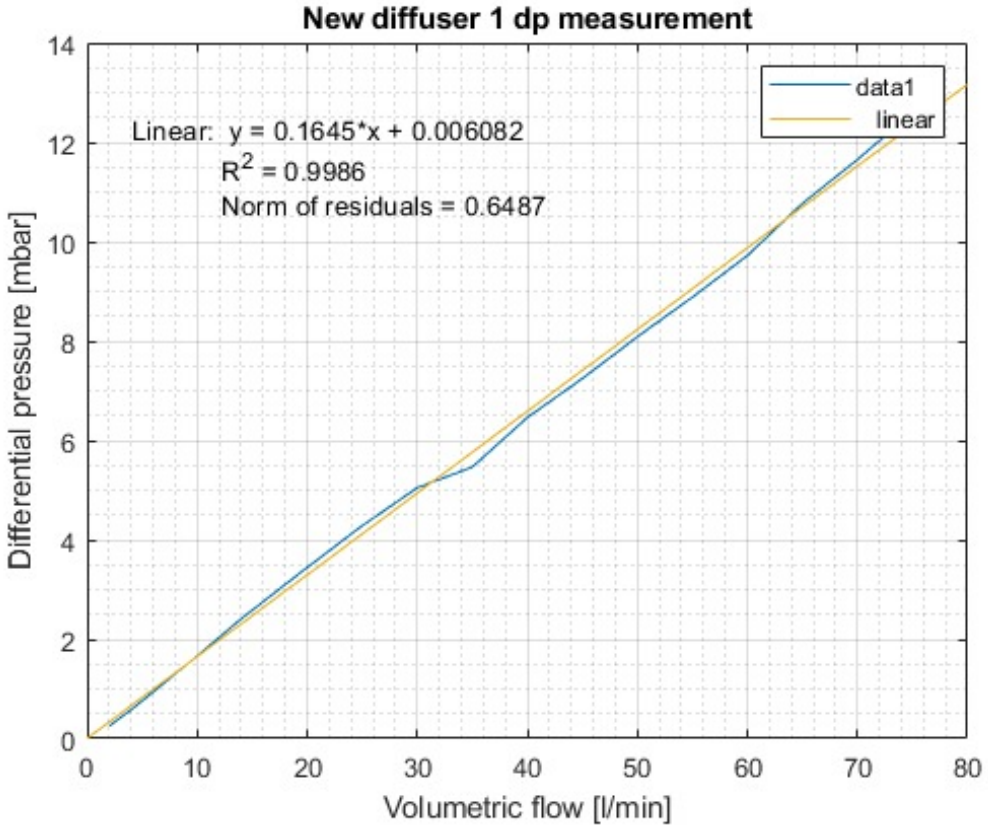
Two types of modifications from the unsuccessful tests described in the Appendix A were tested:

- Increased powder volumes: 500 and 750 ml of powder were used to raise the bed pressure drop while keeping the same diffuser plate as before, thereby varying only one experimental parameter;
- Alternative diffuser designs: new diffuser plates with different geometries were tested to identify configurations that would yield a lower pressure drop, potentially enabling the use of smaller powder volumes.

For this second test series, only the F-202AV flow controller was employed, to eliminate the step effect observed previously. Although it responded more slowly at lower flow rates, this was considered acceptable due to the improved measurement accuracy. The original diffuser plate was also re-tested under these conditions for direct comparison. The results are shown below:

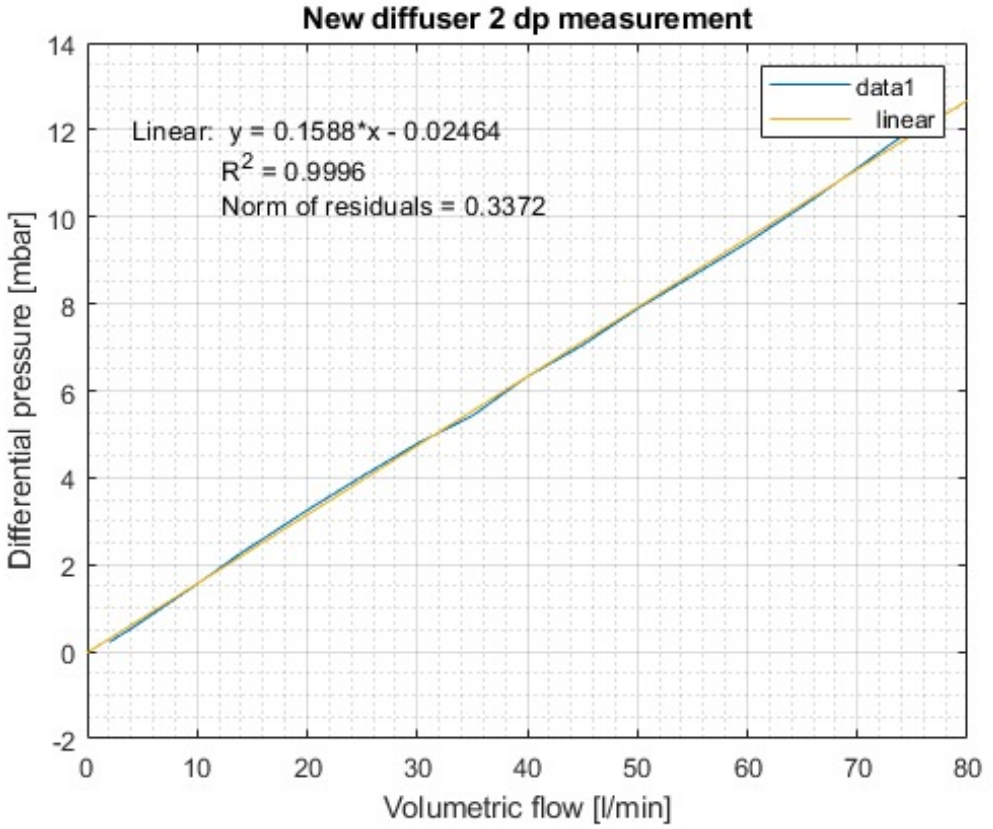


(a) Pressure drop through the old diffuser plate.



(b) Pressure drop through the first new design for the diffuser.

Figure 4.12

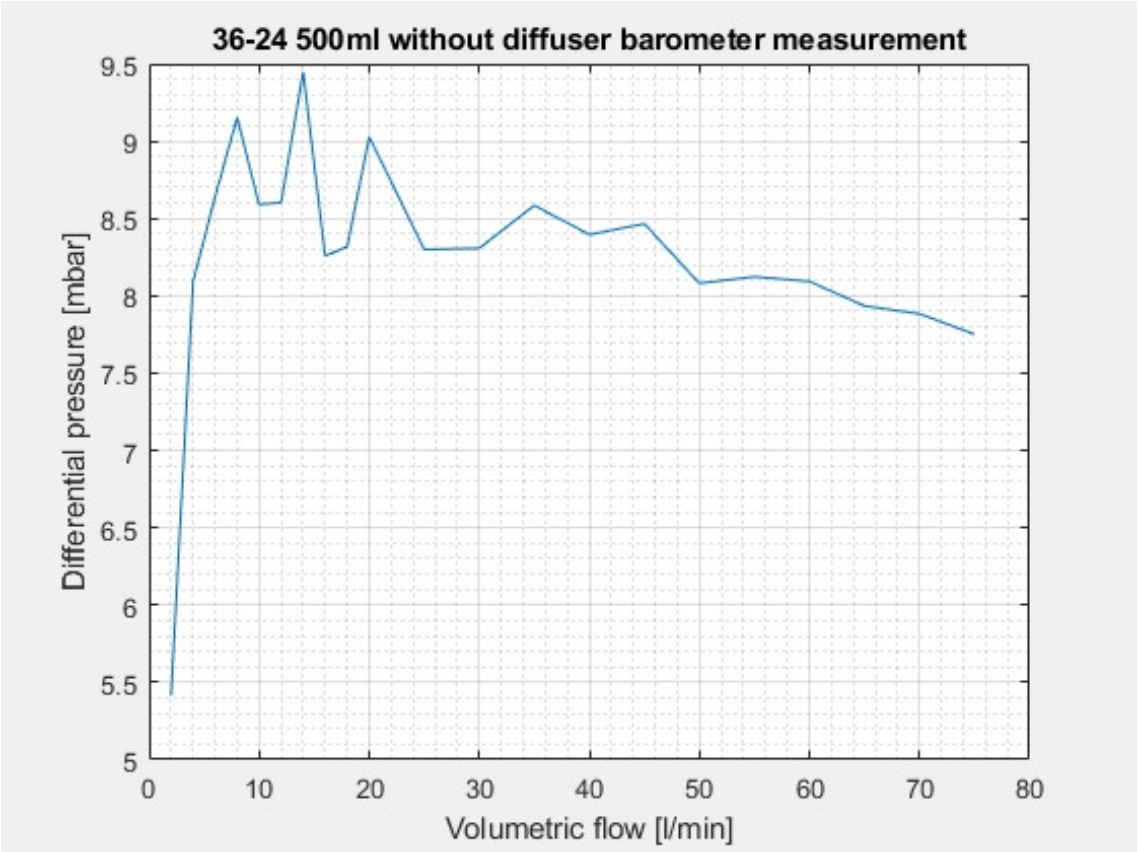


(c) Pressure drop through the second new design for the diffuser.

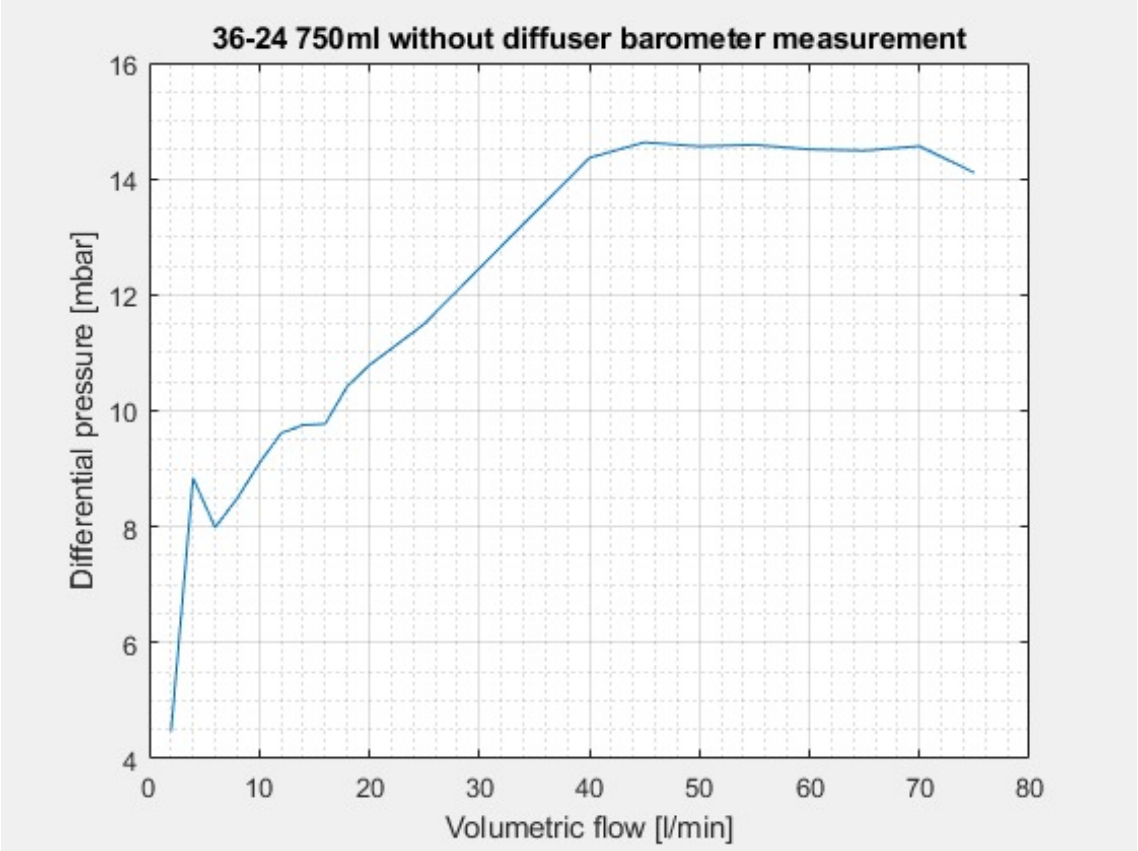
Figure 4.12: The graphs obtained in the second experimental run for the pressure drop of the various diffuser plate designs.

A linear interpolation line was added to each graph, and the corresponding R^2 value was reported. The results clearly indicate that not only did the pressure drop not decrease, but it was slightly higher for both new diffuser designs. Since no alternative meshes were available at the time, additional configurations could not be tested. However, if new meshes compatible with the tested powders (i.e., with openings smaller than the particle diameters) become available, further tests using smaller powder volumes (around 250 ml) should be feasible.

Additional tests were also carried out with increased powder volumes. After post-processing (outlier removal, averaging for each flow level, and correction for diffuser plate influence), the following results were obtained:

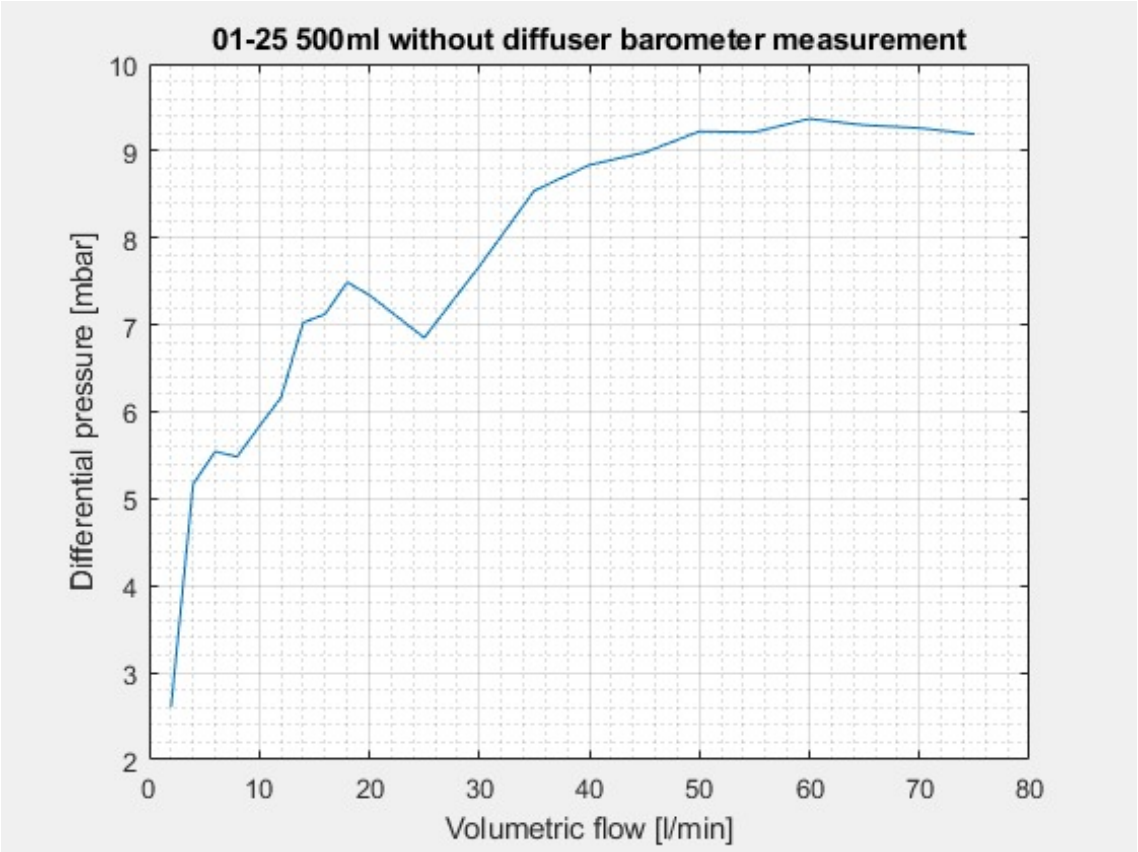


(a) Graph for 500 ml of 36/24 powder.

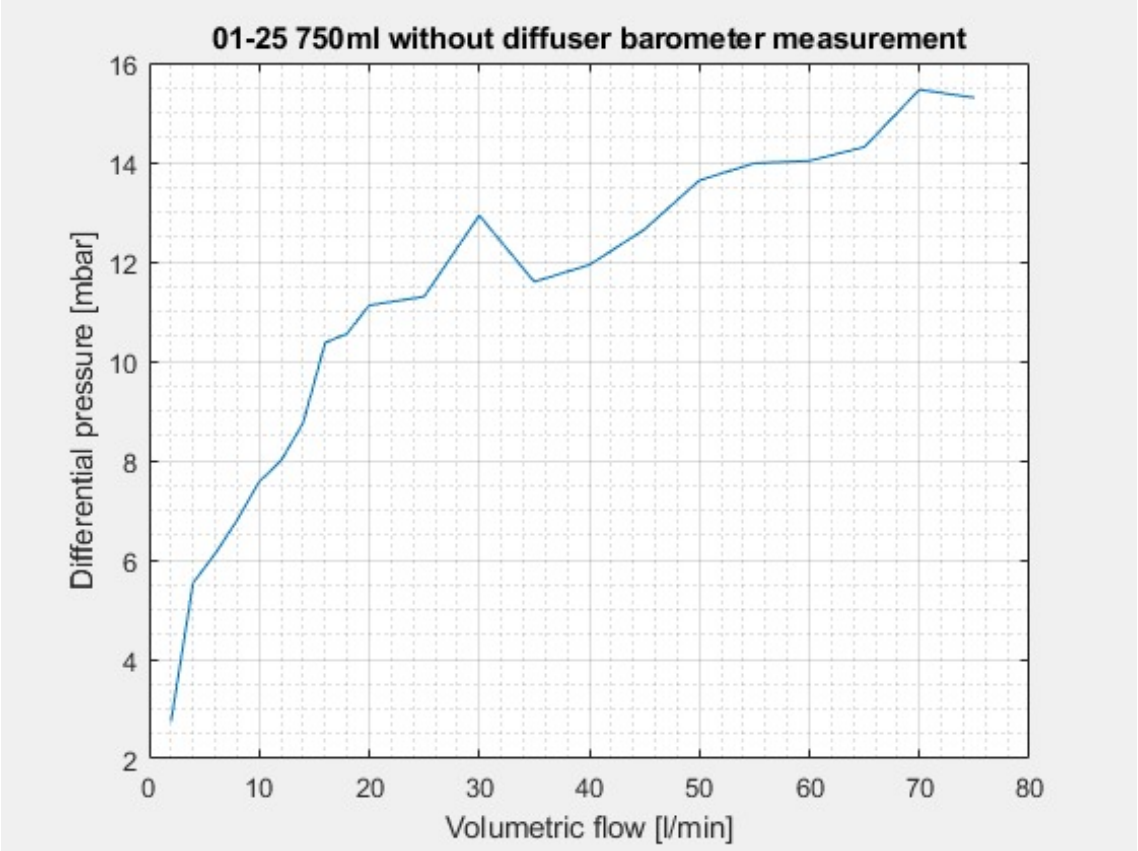


(b) Graph for 750 ml of 36/24 powder.

Figure 4.13

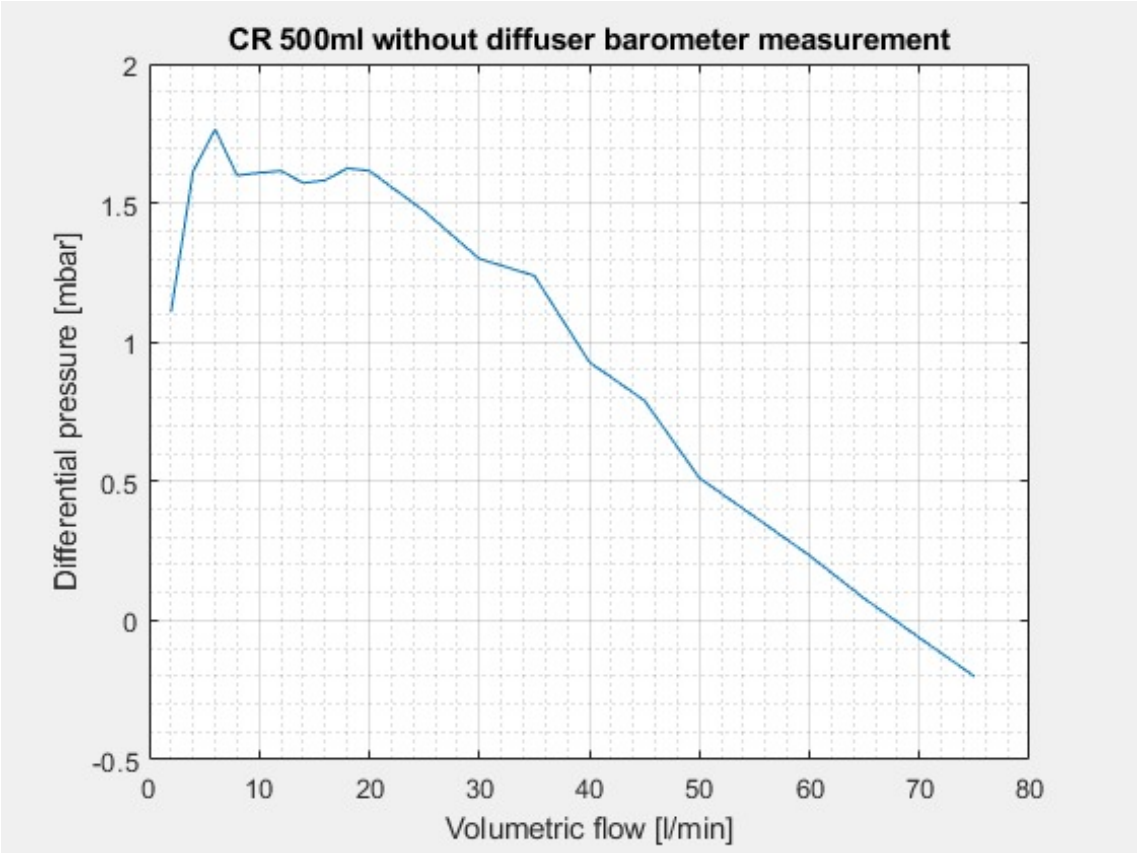


(c) Graph for 500 ml of 01/25 powder.

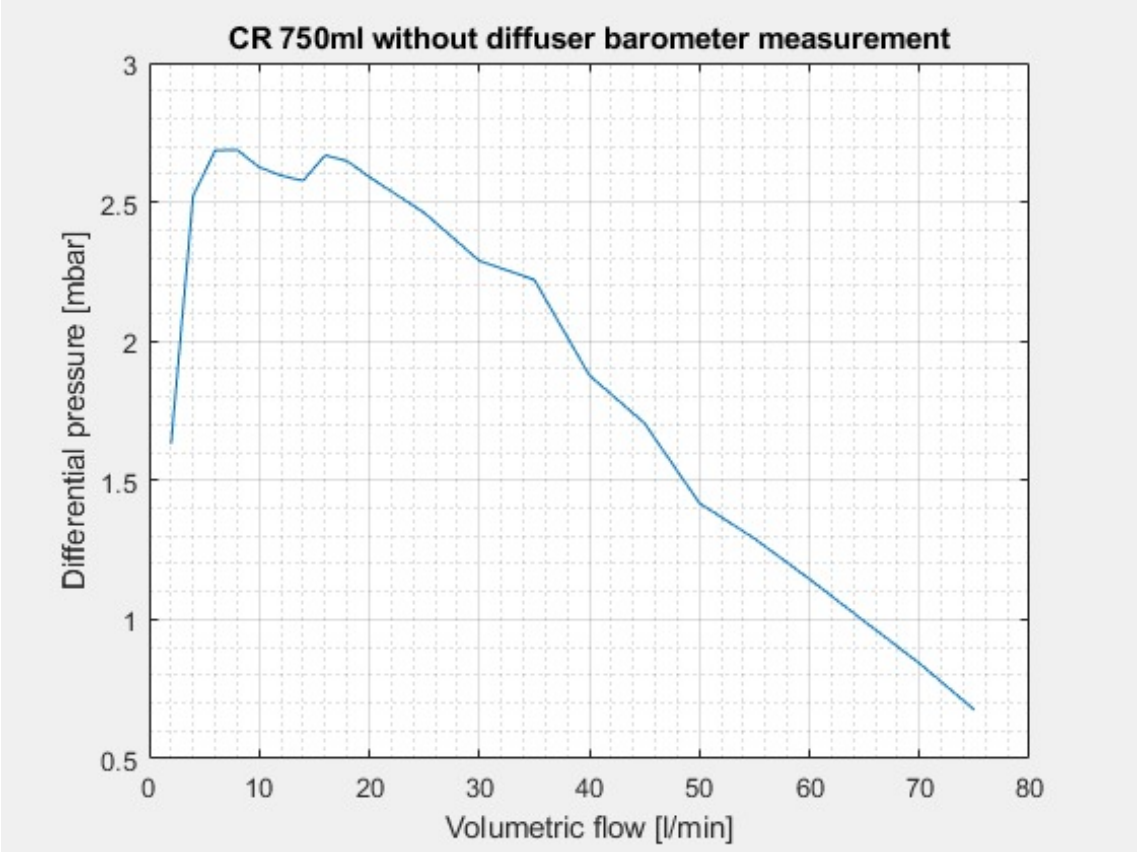


(d) Graph for 750 ml of 01/25 powder.

Figure 4.13



(e) Graph for 500 ml of CR powder.



(f) Graph for 750 ml of CR powder.

Figure 4.13: Comparisons between different volumes of powder for the new fluidization tests.

A few key observations can be made:

- Increasing the volume of the 36/24 powder produced the desired results: at 750 ml it is evident that the minimum fluidization velocity u_{mf} is at 40 l/min.
- The 01/25 powder displayed inconsistent behavior: even though a fluidization plateau is visible for the 500 ml experiment, it disappeared for the 750 ml one. Several factors may explain this:
  - The two powders belong to different Geldart groups, meaning that increasing the bed height may have stabilized one system but destabilized the other;
  - The change in mass and bed geometry may have introduced instabilities not present at lower volumes.
- The CR powder continued to show unusual behaviour similar to that of the first tests. This is likely due to its low bulk density, which results in a smaller bed weight for the same volume and thus a lower required drag force (and corresponding pressure drop) to initiate fluidization. Consequently, its measured pressure drop remained low compared to that of the diffuser plate.

The gas flow rates applied during the high-temperature reduction tests in the furnace were derived directly from the first round of cold-bed fluidization experiments, as the fluidization behaviour was deemed reliable at the time, even though initial pressure-drop curves also showed unusual shapes. It was only during the execution of the reduction experiments, where significant particle entrainment and unexpected bed behaviour were observed, that the inaccuracies of these preliminary cold tests became apparent. This prompted the execution of the second series of fluidization tests to try and determine the true minimum fluidization velocities and to understand the root cause of the initial anomalies. Consequently, it must be noted that the high-temperature reduction tests were conducted using flow rates that were significantly higher than the optimal values.

Nonetheless, this experience provided valuable insight into the sensitivity of the system and informed the later refinement of the experimental procedure.

4.2.3 Comparison of Theoretical and Experimental Results

Since the results obtained from the experiments carried out for this thesis did not exhibit a fully consistent behaviour, the corresponding data from other members of the research group, obtained under identical experimental conditions, were used as a reference. Their results showed to be more coherent, despite the procedures and instrumentation being nominally the same. The fluidization velocities they calculated are:

- 36/24 powder: fluidization starts at 5 l/min, which means that $u_{mf} \approx 8.9$ mm/s;
- 01/25 powder: fluidization starts at approximately 10 l/min, so $u_{mf} \approx 18$ mm/s;

- CR powder: this powder was not analysed by them, so the value of 8 l/min was used (from the analysis done with 500 ml of powder this was the value at which a small plateau was present), which corresponds to a $u_{mf} \approx 14$ mm/s.

By comparing these experimental results with the theoretical values calculated at 20 °C (see table 4.10), it can be observed that the theoretical models provide their best agreement with the 01/25 powder. For this material, the average theoretical fluidization velocity (calculated over the various particle diameters) differed by only about 15 % from the experimentally determined value.

In contrast, the other two powders exhibited significant deviations: for the CR powder, the average theoretical value was approximately 1.5 times higher than the experimental one, while for the 36/24 powder it was more than five times greater.

This behaviour is believed to be strongly influenced by the intrinsic characteristics of the powders, particularly their internal structure and surface morphology. As will be discussed in detail in Chapter 3.4.4, the XRD and related analyses provide valuable insights into the crystalline and microstructural features of the particles, which may help explain the observed discrepancies between theoretical predictions and experimental results.

It should be noted that the theoretical correlations commonly used for fluidization calculations do not account for particle porosity, irregular shapes, or complex surface textures. Consequently, materials with such characteristics, like the powders analysed here, tend to deviate from the behaviour predicted by classical models originally derived for non-porous, spherical materials such as sands or glass beads.

4.3 High Temperature Reduction Results

This chapter describes the analytical techniques used to interpret and validate the results of the high-temperature reduction experiments. A combination of methods is employed to characterise the reacted powders:

- Calorimetric analysis: to determine the reduction degree of the powders;
- TGA analysis: to offer the complementary information from calorimetric analysis about the oxidation degree of the powders;
- BET analysis: to determine changes in surface area and morphology compared to the unreacted powders.

For each method the measurement protocol, data processing procedures, and the specific parameters extracted for comparison with the experimental campaign (e.g. degree of reduction, surface area change, pore evolution, and evidence of post-oxidation) will be presented.

4.3.1 Calorimetric Analysis

The values obtained from the experiments are:

01/25$_{500}$ [J/g]	5476
01/25$_{600}$ [J/g]	6549
36/24$_{500}$ [J/g]	3342
36/24$_{600}$ [J/g]	4521
CR$_{500}$ [J/g]	8174
CR$_{600}$ [J/g]	2254

Table 4.11: Calorimetric values in J/g for the different powders.

Some of the values are higher compared to the theoretical calorific value of the pure iron because the calibration used in the machine gives results that are scaled by a constant (which is known from calibration measurements) compared the real values. After adjusting the values and calculating for the reduction degree the following results are obtained:

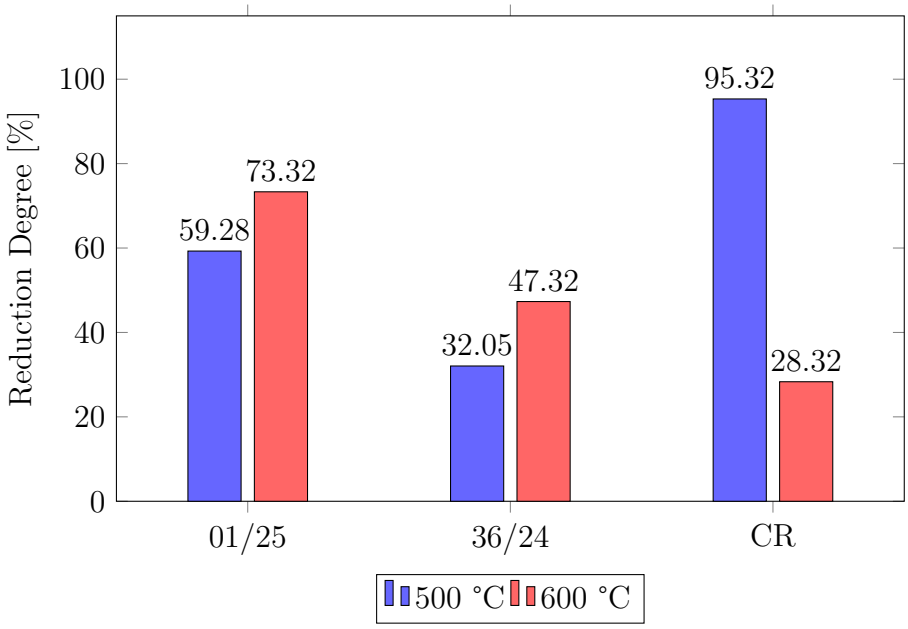
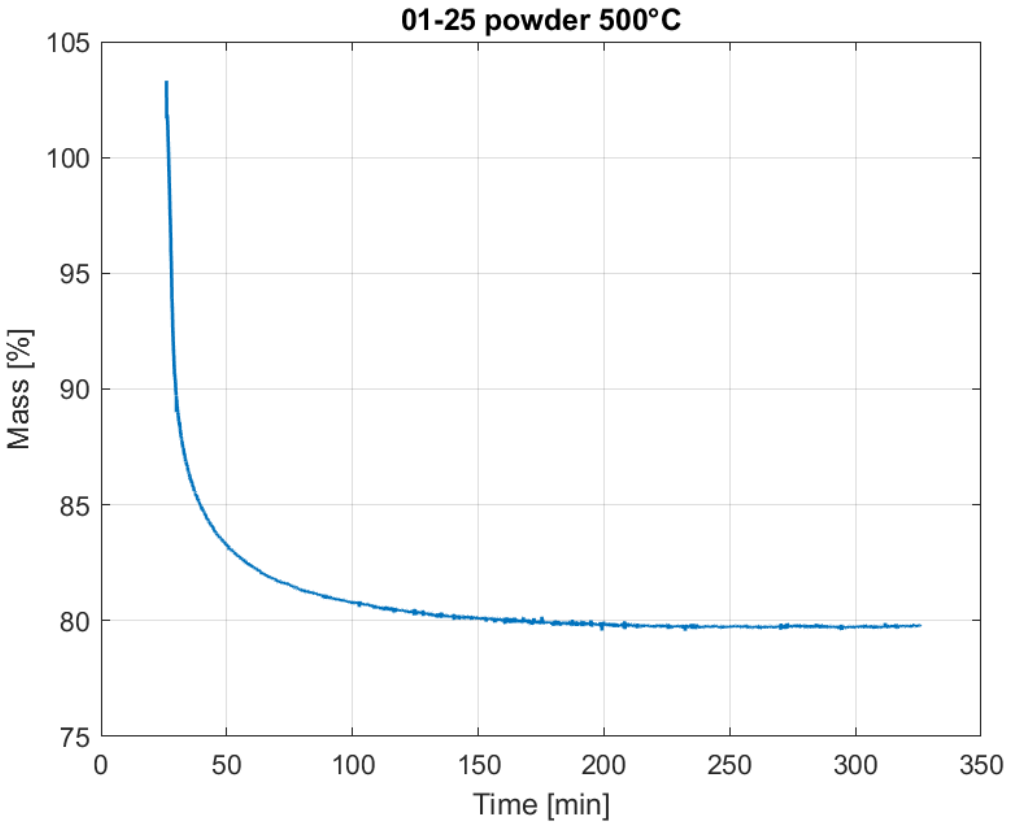


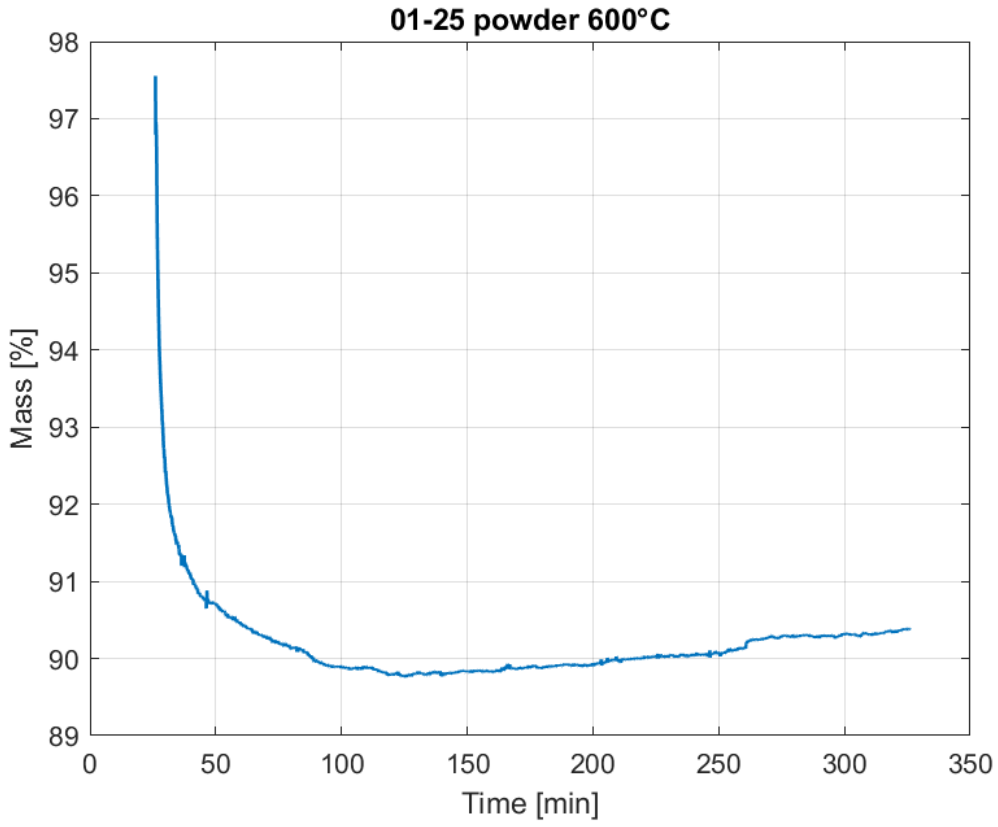
Figure 4.14: Reduction degrees calculated for each powder at 500 °C and 600 °C.

4.3.2 TGA Analysis

In order to validate the results obtained from the calorimetry tests, a series of additional TGA reduction experiments was performed using the combusted powder samples. In these experiments, the measured mass loss is directly proportional to the oxygen content remaining within the material. This relationship enables a quantitative assessment of the post-oxidation state of the powders. Consequently, the TGA measurements provide an independent means of confirming the oxidation degree inferred from the calorimetric analysis and thus serve as a complementary validation of the previously obtained results.

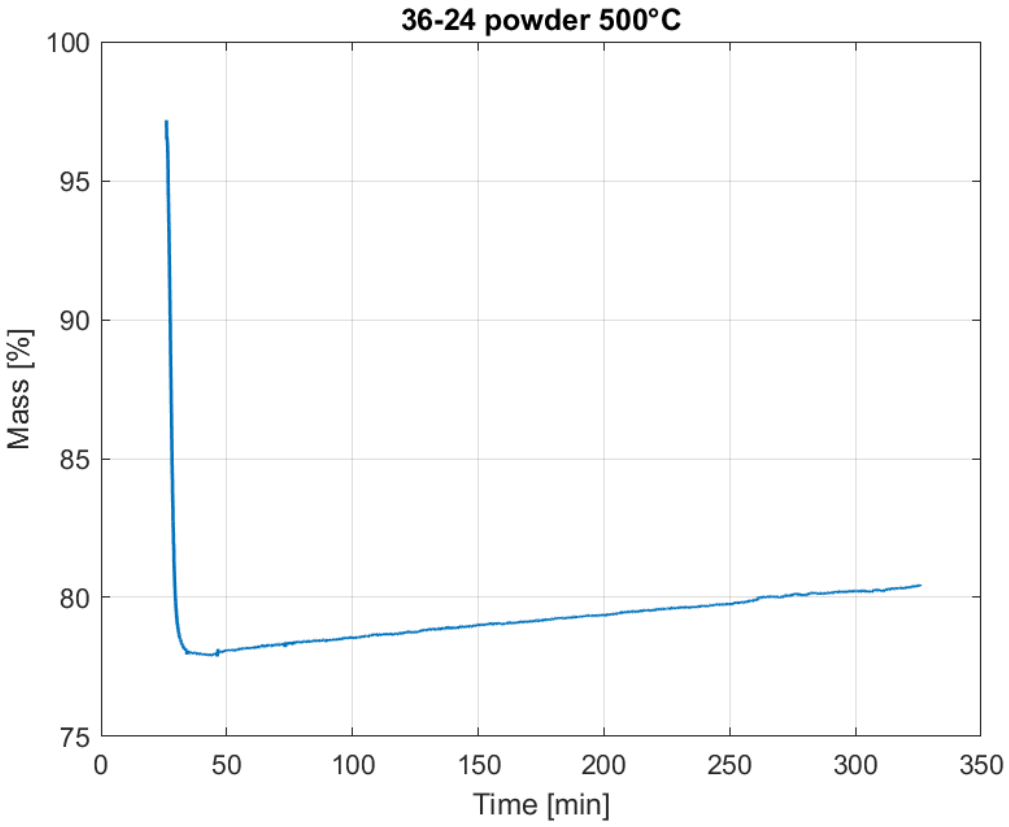


(a) 01/25 at 500°C.

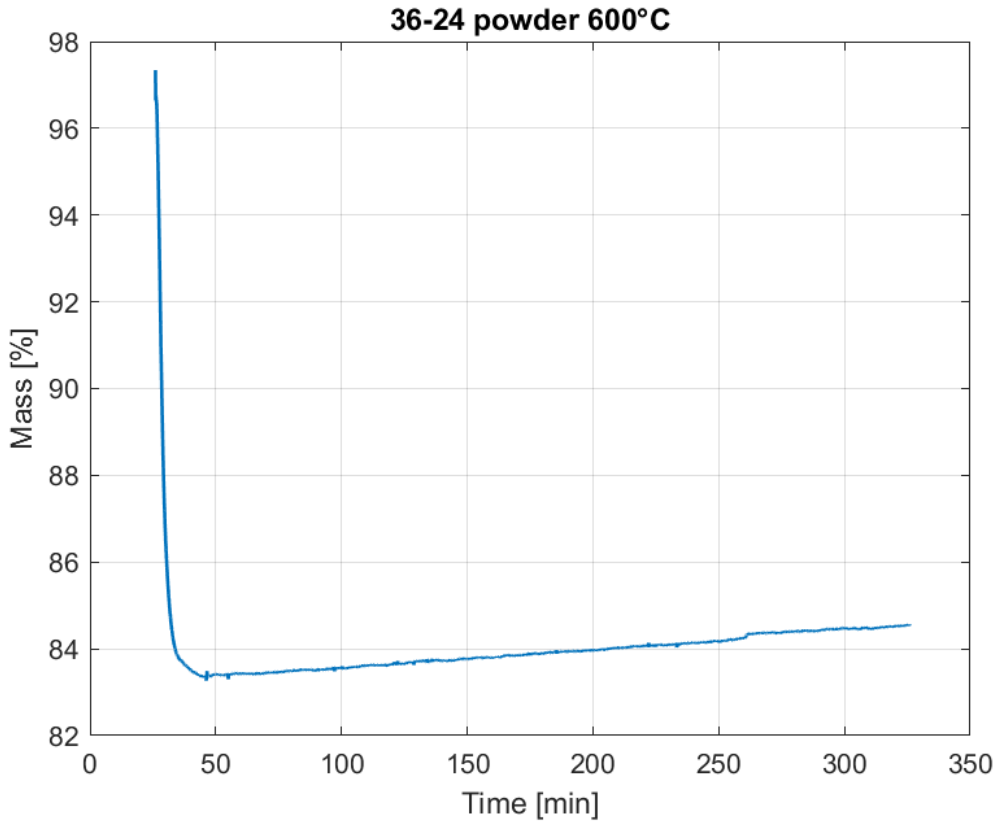


(b) 01/25 at 600°C.

Figure 4.15

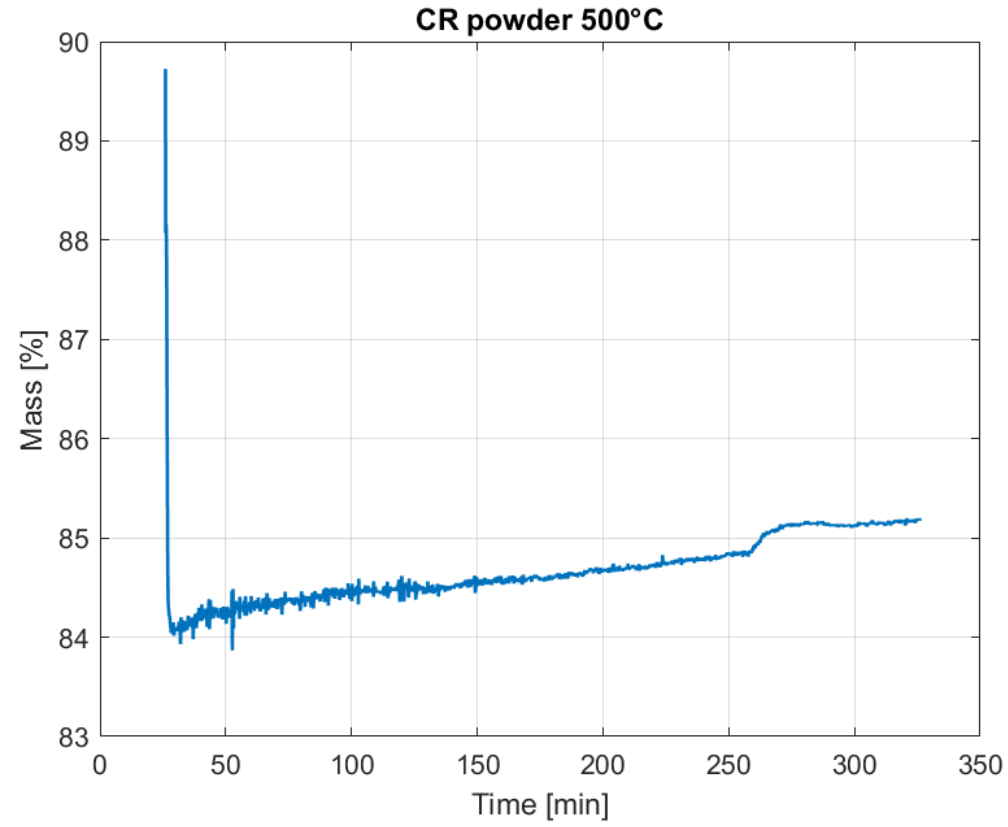


(c) 36/24 at 500°C.

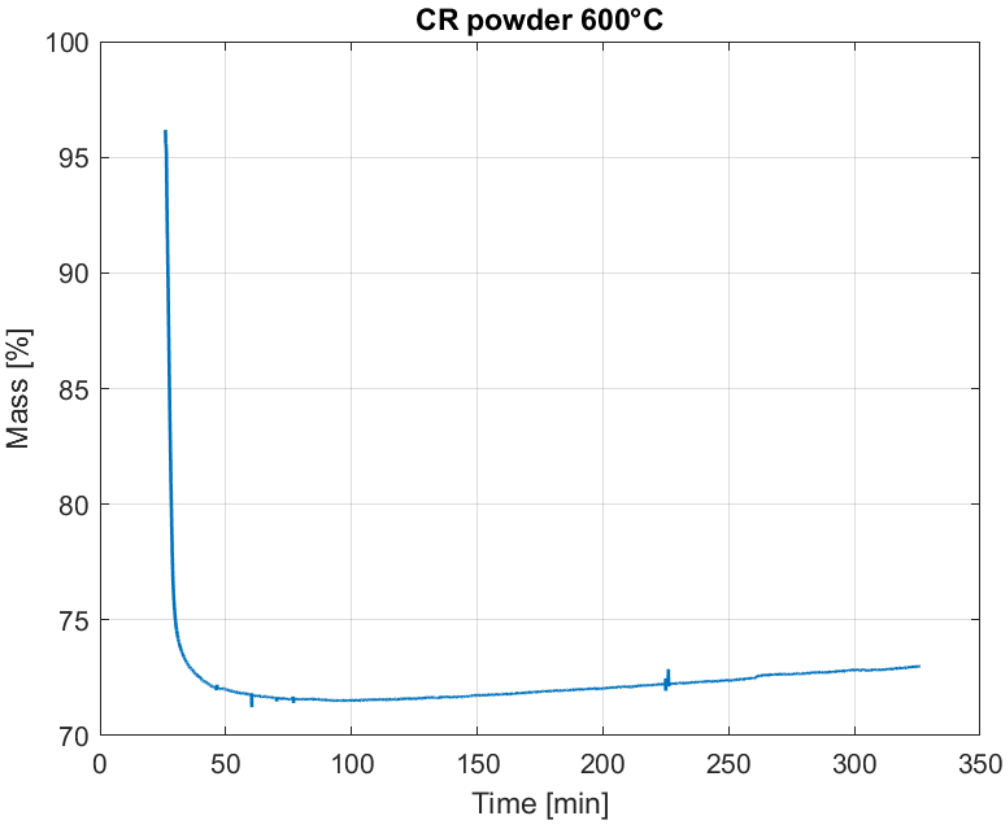


(d) 36/24 at 600°C.

Figure 4.15



(e) CR at 500°C.



(f) CR at 600°C.

Figure 4.15: Graphs of the TGA experiments on the combusted powders.

As shown in the graphs, the powders exhibiting a higher post-oxidation degree also display a correspondingly higher mass loss in the TGA measurements, which is consistent with expectations.

However, the obtained results do not replicate the trend observed in the calorimetry experiments with complete accuracy. This discrepancy can be readily attributed to the substantially smaller sample quantities used in the TGA tests compared with those employed in the calorimetry measurements. In addition, because the reduction reaction proceeds very rapidly, owing to the reduced amount of oxide present in the combusted powders. a small deviation in the measured mass can lead to disproportionately large effects on the final results. Together, these factors provide a clear explanation for the observed divergence between the two experimental techniques.

Despite the presence of this measurement variability, the overall outcome of the TGA analysis remains consistent with the conclusions drawn from the calorimetry experiments. Although the trends do not align perfectly in quantitative terms, the qualitative agreement between the two methods supports the validity of the calorimetric results. In particular, the correspondence between higher post-oxidation degrees and increased mass losses reinforces the reliability of the initial findings. Therefore, even considering the inherent limitations of the TGA measurements, the combined evidence confirms that the conclusions derived from the calorimetry tests are both sound and robust.

4.3.3 BET Analysis

The results obtained from the BET analysis of the samples that went through the reduction reaction in the furnace are shown below. It is important to notice that, because of the heavy entrainment due to the incorrect gas flow inside of the chamber, only the biggest particles remained to be analysed.

Parameter	**01-25**	**36/24**	**CR**
$\mathbf{V}_m$ [cm^3/g]	0.65	5.51	0.59
C [−]	437.62	105.02	83.00
$\mathbf{d}_{pores}$ [nm]	2.76	7.14	7.49
$\mathbf{a}_{s,BET}$ [m^2/g]	2.81	23.98	2.55
$\mathbf{V}_{pores}$ [cm^3/g]	$1.94 \cdot 10^{-3}$	$4.28 \cdot 10^{-2}$	$4.18 \cdot 10^{-3}$
$\mathbf{V}_p$ [cm^3/g]	$1.00 \cdot 10^{-3}$	$4.04 \cdot 10^{-2}$	$6.25 \cdot 10^{-3}$
$\mathbf{a}_p$ [m^2/g]	$9.15 \cdot 10^{-1}$	22.80	3.56
$\mathbf{r}_{p,peak}$ [nm]	1.47	2.43	1.47
$\mathbf{a}_1$ [m^2/g]	2.03	18.15	1.54
$\mathbf{a}_2$ [m^2/g]	0.50	39.94	6.49
$\mathbf{V}_p$ [cm^3/g]	$1.37 \cdot 10^{-3}$	$-1.05 \cdot 10^{-2}$	$-2.08 \cdot 10^{-3}$
$\mathbf{d}_{p,peak}$ [nm]	0.9	1.8	0.9

Table 4.12: BET results for the powders that reacted at 500 °C.

Parameter	01-25	36/24	CR
$\mathbf{V}_m$ [cm^3/g]	0.83	3.51	2.87
C [−]	179.73	87.50	276.05
$\mathbf{d}_{pores}$ [nm]	4.35	8.56	2.66
$\mathbf{a}_{s,BET}$ [m^2/g]	3.61	15.29	12.48
$\mathbf{V}_{pores}$ [cm^3/g]	$3.93 \cdot 10^{-3}$	$3.27 \cdot 10^{-2}$	$8.31 \cdot 10^{-3}$
$\mathbf{V}_p$ [cm^3/g]	$3.17 \cdot 10^{-3}$	$3.13 \cdot 10^{-2}$	$4.30 \cdot 10^{-3}$
$\mathbf{a}_p$ [m^2/g]	2.16	14.26	3.92
$\mathbf{r}_{p,peak}$ [nm]	1.47	5.09	1.47
$\mathbf{a}_1$ [m^2/g]	2.38	10.06	8.45
$\mathbf{a}_2$ [m^2/g]	2.41	39.22	2.39
$\mathbf{V}_p$ [cm^3/g]	$7.21 \cdot 10^{-4}$	$-2.07 \cdot 10^{-2}$	$5.50 \cdot 10^{-3}$
$\mathbf{d}_{p,peak}$ [nm]	0.9	0.9	0.9

Table 4.13: BET results for the powders that reacted at 600 °C.

The unreacted powders had very low BET areas and tiny pore volumes (from figure 4.4). After the reaction the materials generally developed substantially more accessible surface and mesoporosity, especially at 500 °C (with the largest relative gains for sample36/24), with total pore volumes and mesopore volumes rising markedly. At 600 °C the response became sample-dependent: some powders (e.g. 36/24) lose part of the 500 °C gain (consistent with sintering or coarsening), while others (notably 39/24) show dramatic area and pore-volume increases at the higher temperature. Mean pore diameters tend to shift toward smaller values in several cases (indicating creation of many small pores), but the micropore fits are unstable and not reliable. Finally, because significant entrainment removed fines during the fluidized reaction, the BET results reflect mainly the retained coarse fraction and likely underestimate (or at least do not precisely represent) the true bulk properties of the entire reacted product. This effect will be talked about with more precision inside of chapter 5

4.4 Summary of Powder Characteristics

The individual analytical techniques discussed in the previous sections provide valuable but isolated insights into the physical, chemical, and morphological features of the investigated powders. However, as demonstrated, no single parameter is sufficient to predict the macroscopic performance of the particles inside the reactor. To better understand how these distinct traits interact and ultimately dictate the fluidization quality and reduction kinetics of the materials, a holistic cross-comparison is essential.

Property	**01/25**	**36/24**	**39/24**	**CR**
Morphology	Jagged, dense	Highly porous	Compact, irregular	-
x_{50}	31.65 μm	73.62 μm	19.93 μm	79.96 μm
$a_{s,BET}$	0.78 m^2/g	5.25 m^2/g	0.73 m^2/g	3.16 m^2/g
Impurities	Traces (<1%)	Al, Si	Mg ($\approx$ 3%)	Pure Fe_2O_3
u_{mf}	$\approx$ 18 mm/s	$\approx$ 8.9 mm/s	Does not fluidize	$\approx$ 14mm/s
t_{10} **(500 °C)**	4.40 min	1.45 min	6.50 min	-

Table 4.14: Summary of the main physical, chemical, and behavioral properties of the tested iron-oxide powders.

As summarized in table 4.14, the macroscopic behavior of the powders is strongly dictated by their microstructural and chemical properties. For instance, despite having the largest median size (x_{50}), the 36/24 powder exhibits the best fluidization properties (the minimum fluidization velocity u_{mf}) and the fastest reduction kinetics (the t_{10} time) due to its highly porous structure and massive surface area ($a_{s,BET}$). Conversely, the 39/24 powder, while having the smallest particle size, fails to fluidize and reduces slowly, a behavior likely caused by its dense, irregular morphology (as seem in the XRD analysis) and the significant presence of magnesium impurities. The 01/25 powder represents an intermediate case, where high chemical purity is counterbalanced by a jagged, dense morphology that requires high gas velocities to fluidize.

5. Discussion

As we talked about in the previous chapters, two main errors during the experimental campaign happened:

1. Entrainment of fines during furnace experiments caused by an incorrect fluidization velocity assumption at room temperature;
2. Partial post-oxidation during cooling after reduction.

The first one caused a probable shift of the morphological properties found for the subsequent BET analysis of the powders that underwent high temperature reduction (whose results are shown in chapter 4.3.3), since the particles that remained were those that couldn't entrain at those high flows, meaning the larger ones.

The post-oxidation cannot let us know the real reduction degree obtained by the powders during the reduction reaction, but since one of the powders shown in table 4.11 (specifically the CR powder that reacted at 500 °C) achieved an almost complete reduction, an analysis of the possible original reduction degree of the powders is possible through the assumption that that sample didn't undergo any post-oxidation and through the assumptions that the reduction degree is at least partially correlated with the BET properties for the baseline particles shown in tables 4.4, 4.5 and 4.6 (even though we know that not only those parameters change during the reaction, but that the correlation is not ideal).

5.1 Changes in BET Data

When the powders were reacted in the high-temperature fluidized reduction, the BET and pore parameters changed substantially, but in a way that depends on sample and temperature.

Large increases in BET area and pore volume after reaction. At 500 °C the specific surface area (a_s, BET) rises compared to the unreacted by roughly:

- 01-25: $\approx$+262% (0.78 $\rightarrow$ 2.81 m^2/g);

- 36/24: ≈+356% (5.25 → 23.98 m^2/g), the biggest absolute and relative jump;
- 39/24: ≈+248% (0.73 → 2.55 m^2/g).

At 600 °C the picture is mixed:

- 01-25 continues to increase (≈+366% compared to unreacted: 0.78 → 3.61 m^2/g);
- 36/24 falls back relative to the 500 °C value (23.98 → 15.29 m^2/g) but remains well above the unreacted value (+≈191% compared to unreacted);
- 39/24 shows a very large rise by 600 °C (≈+1600% compared to unreacted: 0.73 → 12.48 m^2/g).

Pore volume (mesopore / total pore) generally increases. For example: sample 36/24 V_{pores} (total pore volume from BET) goes from ≈0.01 cm^3/g (unreacted) → 0.04 (500 °C, +∼310%) → 0.033 (600 °C, +∼214% unreacted). For 39/24 the V_{pores} increases massively at 600 °C (≈1.59 $\cdot 10^{-3}$ → 8.31 $\cdot 10^{-3} cm^3/g$, +≈423%).

Pore size changes are heterogeneous. Some samples show pore narrowing (e.g. 01-25 d_{pores}: 8.04 nm → 2.76 nm at 500 °C, then to 4.35 nm at 600 °C), others show little change or slight increases (36/24 stays ∼8 nm), while 39/24 collapses to very small average diameters at 600 °C (8.67 → 2.66 nm). These shifts indicate competing mechanisms (pore creation vs. coarsening/sintering or collapse) that are highly sample and temperature-dependent.

Mesopore peak radius and mesopore volume fits change ($r_{p,\text{peak}}$ and V_p in the mesopore fits), consistent with formation of new mesoporosity for some samples (36/24 at 500 °C) and with coarsening/sintering for others (36/24 partial loss of area at 600 °C compared with 500 °C).

The micropore volume entries include tiny negative numbers in some fits. This is a classic indicator that the micropore model is not robust for these samples (they simply do not have a measurable micropore contribution and the fit noise produces small negative values). The micropore values are to be treated as unreliable because of this.

The increase in BET area and pore volume after reduction likely arises from chemical reduction (oxide → metal) and associated solid-state reorganization: reduction can produce internal stresses, phase changes, and fissuring that open up mesopores and increase accessible surface area. For some formulations (36/24), the reaction at 500 °C appears to produce a lot of new mesoporosity (large jumps in mesopore volume and BET area).

At higher temperature (600 °C) there is evidence of competitive sintering/coarsening for at least one sample (36/24): a_s drops from 23.98 → 15.29 m^2/g between 500 and 600 °C, consistent with partial neck growth and loss of fine porosity at the higher temperature. Conversely, 39/24 shows a dramatic increase at 600 °C that indicates sample-specific composition and morphology control whether the dominant effect is pore creation or collapse.

The shifts in pore diameter (both decreases and increases) are consistent with either formation of many small pores (shift to smaller mean pore diameter but higher volume) or with coarsening (larger pores, lower area). Which dominates depends on the starting microstructure and chemical transformations during reduction.

Significant entrainment occurred during the fluidized reaction and the powders analysed afterwards represent only the non-entrained (relatively large) particles that remained in the reactor. This produces a sampling bias.

Entrainment preferentially removes the finer fraction (small particles and fragments). The fines typically have higher surface area per unit mass (from the cube-squared law). This means that not only they are lighter and therefore a lower drag force is needed to lift them, but since drag force is proportional to the area of the particles, they are also comparatively more affected by the drag force. A factor to consider is that not only the smaller particles that were initially present in the sample were lost, but if any small particles were created during reaction (for example by cracking of existing larger particles), these would be lost too, and with them also information on how the average structure of the particles changes during reaction.

We can put some numbers on how large this bias could be using a two-fraction mass model. Let:

- r be the mass fraction remaining (the fraction that was analysed),
- X_{means} be the measured quantity on remaining fraction (what is in the table),
- $X_{\text{entrained}}$ be the value of the entrained (lost) fraction.

The true bulk average would be

$$X_{\text{bulk}} = r \cdot X_{\text{means}} + (1 - r) \cdot X_{\text{entrained}} \tag{5.1}$$

We can compute a conservative scenario where the entrained material retained its unreacted BET values. This gives a lower bound on how large the reacted bulk average could be if the entrained fraction were less altered than the retained fraction, since we have seen that the BET values usually increased.

Using two realistic remaining fractions (since from visual observations the 36/24 powder seemed to lose only about half of its initial volume, and the other two powders were mostly entrained) $r = 0.5$ and $r = 0.1$ (i.e., only 30-50% of the original mass was left to measure), the corrected bulk estimates (for the $a_{s,\text{BET}}$ parameter) become:

- 36/24 powder:
  - 500 °C:
    - $r = 0.5$: $a_{s,\text{BET,bulk}} = 0.5 \cdot 23.98 + (1 - 0.5) \cdot 5.25 = 14.62$ m^2/g;
    - $r = 0.1$: $a_{s,\text{BET,bulk}} = 0.1 \cdot 23.98 + (1 - 0.1) \cdot 5.25 = 7.13$ m^2/g .
  - 600 °C:
    - $r = 0.5$: $a_{s,\text{BET,bulk}} = 0.5 \cdot 15.29 + (1 - 0.5) \cdot 5.25 = 10.27$ m^2/g;

    * $r = 0.1$: $a_{s,\mathrm{BET,bulk}} = 0.1 \cdot 15.29 + (1 - 0.1) \cdot 5.25 = 6.26\ \mathrm{m^2/g}$.

- 01/25 powder:
  - 500 °C:
    * $r = 0.5$: $a_{s,\mathrm{BET,bulk}} = 0.5 \cdot 2.81 + (1 - 0.5) \cdot 0.78 = 1.79\ \mathrm{m^2/g}$;
    * $r = 0.1$: $a_{s,\mathrm{BET,bulk}} = 0.1 \cdot 2.81 + (1 - 0.1) \cdot 0.78 = 0.98\ \mathrm{m^2/g}$.
  - 600 °C:
    * $r = 0.5$: $a_{s,\mathrm{BET,bulk}} = 0.5 \cdot 3.61 + (1 - 0.5) \cdot 0.78 = 2.19\ \mathrm{m^2/g}$;
    * $r = 0.1$: $a_{s,\mathrm{BET,bulk}} = 0.1 \cdot 3.61 + (1 - 0.1) \cdot 0.78 = 1.06\ \mathrm{m^2/g}$.
- CR powder:
  - 500 °C:
    * $r = 0.5$: $a_{s,\mathrm{BET,bulk}} = 0.5 \cdot 2.55 + (1 - 0.5) \cdot 3.16 = 2.86\ \mathrm{m^2/g}$;
    * $r = 0.1$: $a_{s,\mathrm{BET,bulk}} = 0.5 \cdot 2.55 + (1 - 0.5) \cdot 3.16 = 3.10\ \mathrm{m^2/g}$.
  - 600 °C:
    * $r = 0.5$: $a_{s,\mathrm{BET,bulk}} = 0.5 \cdot 12.48 + (1 - 0.5) \cdot 3.16 = 7.82\ \mathrm{m^2/g}$;
    * $r = 0.1$: $a_{s,\mathrm{BET,bulk}} = 0.5 \cdot 12.48 + (1 - 0.5) \cdot 3.16 = 4.09\ \mathrm{m^2/g}$.

While these calculations provide a reasonable lower bound for the actual BET values of the particles after reduction, they remain approximate estimates (they likely underestimate them). A more accurate methodology would involve sieving the uncombusted particles to retain only those with diameters that were not entrained in the furnace, followed by conducting BET analyses on this selected fraction. This approach would yield the BET values corresponding to the uncombusted powder fraction. From these results, a direct comparison of the BET value changes could be performed, and—by assuming that the relative variations are independent of particle diameter—a more reliable estimation of the BET values for the average particle diameter of the combusted powders could be obtained.

The fit reliability isn't good, and as such the micropore values should be treated as "not detected or unreliable.": the very small micropore volumes are signs that the micropore model is not meaningful here. The mesopore and BET numbers are more informative in this case.

In order to remove the entrainment uncertainty the entrained fraction should be collected and analysed (hypotetically through a cyclone or a disc filter) and include its mass and BET in the mass balance. Without that, any statement about the bulk product is based on guesswork.

A possible follow up could be scanning electron images of the retained and entrained fractions, that could help identify whether the newly measured porosity is from fragmentation, fissuring, or selective oxidation/reduction reactions.

5.2 Estimation of the Reduction degree

A rough estimation of the reduction degree achieved before the post-oxidation is possible by comparing the results from the BET analysis done on the unreacted powders, the BET results on the reacted powders, and by keeping the CR powder that reacted at 500 °C as a baseline (therefore assuming that the result obtained with that powder was not affected by any post-oxidation).

From looking at the values in 4.11, it is apparent that a higher temperature correlates with a lower post-oxidation degree (with the obvious exception of the CR powder), and the proportion between the values is approximately 1.5.

Apart from that, even after extensive calculations, no link between the BET properties (either the ones before or after the relative reaction) and the post-oxidation degree was found (or at least no link that was obtained from a reasonable combination of properties).

So, despite the apparent trends, the correlations between the BET parameters and the post-oxidation degree remain weak and inconsistent. Several factors likely contribute to this outcome. First and foremost, the limited number of data points makes any statistical relationship highly uncertain. With only a few samples available, even small variations in measurement or material behaviour can significantly influence the apparent correlation. Moreover, the powders investigated are not strictly equivalent: differences in composition, phase distribution, or microstructural features may introduce sample-specific effects that mask any general trend.

Another important consideration is the possible confounding effect of temperature and handling conditions. Since the post-reaction BET measurements and the reaction temperatures are inherently linked, it is difficult to disentangle whether the observed differences arise from thermal effects, from the extent of reduction, or from subsequent re-oxidation during cooling and exposure to air. The handling procedures between reaction and BET measurement may therefore introduce variability that is not captured by the parameters themselves.

Measurement uncertainty further limits the reliability of the correlations. Both BET and calorimetric analyses involve sources of experimental error, and when the total variation in the data is of the same order of magnitude as this uncertainty, even real physical trends become difficult to detect statistically. Finally, it is plausible that the underlying relationship between morphology and oxidation behaviour is non-linear or dependent on multiple factors.

The absence of strong correlations does not imply that the BET data are irrelevant, but rather that they are insufficient to describe the complexity of the oxidation-reduction behaviour of these iron oxide powders. The specific surface area and pore volume quantify important aspects of the microstructure, yet they do not capture surface chemistry, phase composition, or the distribution of reactive sites, all of which can exert an influence on the extent of post-oxidation.

It is therefore reasonable to conclude that re-oxidation is a multifactorial process, controlled not only by surface morphology but also by the chemical and structural state of the particles.

Overall, while the BET data provide valuable insight into the evolution of the samples during reduction and subsequent re-oxidation, they do not appear to be sufficient

on their own to explain the variations in the final oxidation degree. The weak and inconsistent correlations observed suggest that the governing mechanisms are complex and do not involve only surface area and porosity.

5.3 Possible Solutions

In order to avoid the errors discussed in this chapter, various solutions and recommendations are possible:

- Knowing the fluidization velocity accurately: doing multiple tests using appropriate experimental conditions in order to be certain of the actual fluidization velocity at room temperature is advised, in order to be able to exclude any experimental runs that do not match the expected results (which are to be calculated using a variety of different theoretical correlations, for the same reason);
- If the fluidization velocity is calculated correctly, the entrainment of particles should be greatly reduced. It is never possible to completely eliminate it, since a perfectly monodisperse particle size distribution is impossible to achieve, which means that there will always be fines that will entrain. Having a cyclone after the reduction chamber could help with the collection of these fines, possibly giving more information on the percentage and typology of particles that leave the bed.
- Finding a way to reliably keep the nitrogen flowing for a longer period of time. Since it is evident that, especially for powders that require higher gas flows because of their higher minimum fluidization velocity, one single bottle might not be enough for both keeping the correct gas mixture during reaction and for the cooling phase, a system to have two nitrogen bottles working in parallel could be an optimal solution. This setup could also improve the safety of the system, since if one of the gas bottles stopped working, the other one could pick up the slack.
- Repeated tests. In general running experiments multiple times is always good practice. Due to time constraints during this work, this was not always possible, which might have caused some of the errors.

In conclusion, while several sources of uncertainty and experimental error were identified throughout this work, most can be mitigated through careful preparation and improved system reliability.

6. Conclusions

The transition towards a sustainable energy system has identified metal fuels, and specifically the iron cycle, as a promising solution for the storage and transport of renewable energy. While the regeneration of iron oxides using green hydrogen in fluidized bed reactors represents a technologically viable path to close this cycle with zero emissions, its practical implementation still faces significant challenges. A critical open issue concerns the behavior of actual iron ores, which differ substantially from the pure oxides often employed in theoretical studies. The variability in morphological properties, particle size distribution, and the presence of chemical impurities in raw ores profoundly influence both the fluidization properties and the reduction kinetics. Consequently, predictive models often prove inadequate to model the process, necessitating experimental runs in order to understand how these material-specific characteristics dictate the efficiency of the reduction cycle.

This work investigated how particle size distribution, morphology and chemical composition influence the fluidization behaviour and hydrogen reduction of iron-oxide powders in a laboratory-scale fluidized-bed reactor. Using a combination of TGA, BET, XRD, SEM/EDS, ICP-OES, cold-fluidization tests and high-temperature reduction experiments, the thesis developed an interpretation of how structural and chemical features determine macroscopic reactivity and fluidization behaviour.

The results showed that the differences between the powders are not governed by particle size alone. Sample 36/24 exhibited a highly porous microstructure, 01/25 showed irregular and jagged shapes, and 39/24 contained a significant amount of magnesium and had a compact morphology. These characteristics strongly influenced the powders' surface area development, reduction behaviour and fluidization performance.

Compositional impurities were found to play an important role. Aluminum and silicon, detected in 36/24 and in smaller amounts in 01/25, may form phases that affect hydrogen access and modify reduction kinetics. The presence of magnesium in 39/24 (around 3 wt%) likely reduced the effective particle density, contributing to the failure of this powder to fluidise. These findings show that impurity chemistry directly affects both reduction behaviour and the mechanical response of the powders in a fluidized bed.

Morphology also influenced the evolution of BET surface area. Large increases after reduction, especially for 36/24 at 500 °C, are consistent with pore formation or expansion during reduction. However, these measurements were strongly affected by excessive entrainment during the furnace experiments. Many fines were lost because the room-temperature reference flow was incorrectly applied to high-temperature conditions. As a result, the measured BET values represent mainly the coarse fraction that remained in the crucible and do not describe the powder as a whole.

Experimental handling played a major role in the interpretation of the reduction degree. In addition to entrainment losses, an insufficient nitrogen flow during cooling led to partial re-oxidation of some samples. This makes it difficult to determine the true reduction degree from the furnace experiments. One CR sample reduced at 500 °C appeared to reach nearly complete reduction and can be used as a qualitative reference, but a reliable quantitative comparison between powders is not possible without improved cooling and protection.

Several recommendations arise from these findings. Future experiments should recover and analyse the entrained fines to close the mass and surface-area balance. Minimum fluidization velocity should be re-evaluated at room temperature using improved procedures to avoid flow overestimation at high temperature. The cooling protocol should be redesigned with redundant nitrogen supply to prevent re-oxidation. Finally, the retained and entrained fractions should be characterised separately to determine whether fines originate from fragmentation, selective reduction or pre-existing size differences.

In conclusion, this thesis demonstrates that the behaviour of iron-oxide powders in hydrogen fluidized-bed reduction results from the combined effects of morphology, impurity chemistry, porosity and operating conditions. Inclusions and foreign phases were shown to have practical consequences for fluidization performance and reduction kinetics. Addressing the experimental limitations identified here will improve the reliability of future reduction campaigns and enable a more accurate assessment of the intrinsic properties of iron-oxide materials.

A. Appendix

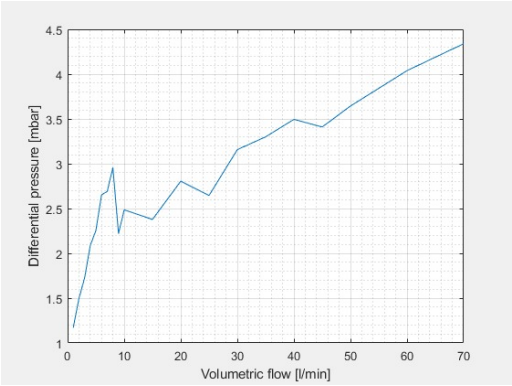
After determining (as seen at the beginning of section 4.2.2) that the MP24 powder's fluidization capabilities were poor, a first round of measurements was then carried out with each of the three remaining suitable powders, using 150 ml, 250 ml and 350 ml of powder. The choice of maintaining a constant powder volume rather than constant mass was based on the fact that, as seen in equation 2.15, keeping a constant bed height (which depends on the powder volume, given the fixed bed cross-section) ensures comparable results.

Three different flow modes were studied:

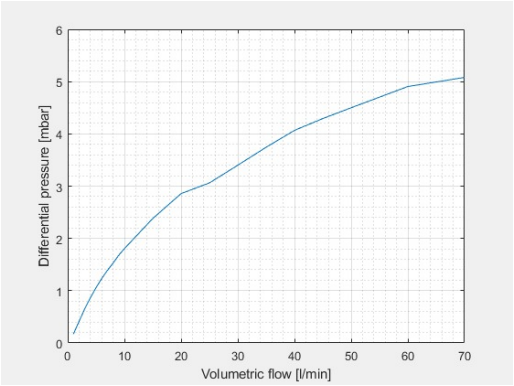
1. An initial increase in flow rate;
2. A gradual decrease;
3. A second increase identical to the first.

This procedure allowed verification of potential hysteresis effects and comparison between the first and second flow increases.

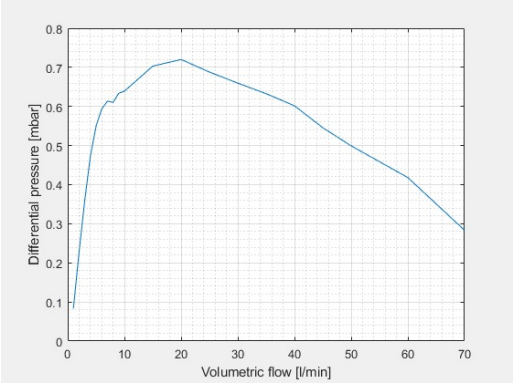
After analyzing the data from this first experimental series, some issues were identified. The graphs obtained for the first flow increase displayed a choppy appearance, which disappeared during the flow decrease and the subsequent increase. This was likely caused by non-uniform powder distribution when first loaded into the vessel, resulting in a non-constant bed height and settling, which disturbed the pressure-drop readings. Once fluidization was achieved, the bed height stabilized, explaining the smoother appearance of subsequent measurements. Moreover, the graphs corresponding to the decrease and second increase did not display the typical increase-plateau shape expected in proper fluidization:



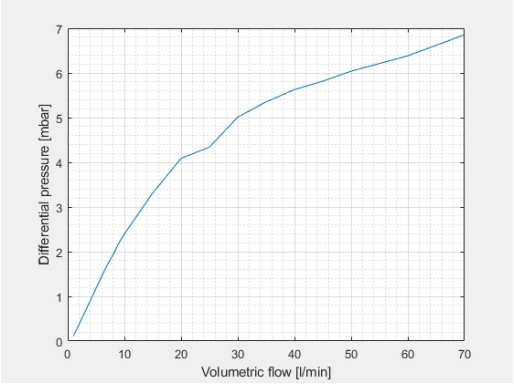
(a) Graph with a choppy appearance from a first flow increase.



(b) Smoother graph, without the typical fluidization graph appearance.



(c) This graph shows a decrease in differential pressure instead of the more typical plateau.



(d) Similarly to graph (b) this graph shows an increase in differential pressure instead of the plateau, but with a different increasing trend.

Figure A.1: Examples of graphs that show an atypical shape.

This behaviour can be explained by noting that the pressure drop across the bed should be greater than or equal to that across the diffuser plate. The diffuser plate's pressure drop is shown below:

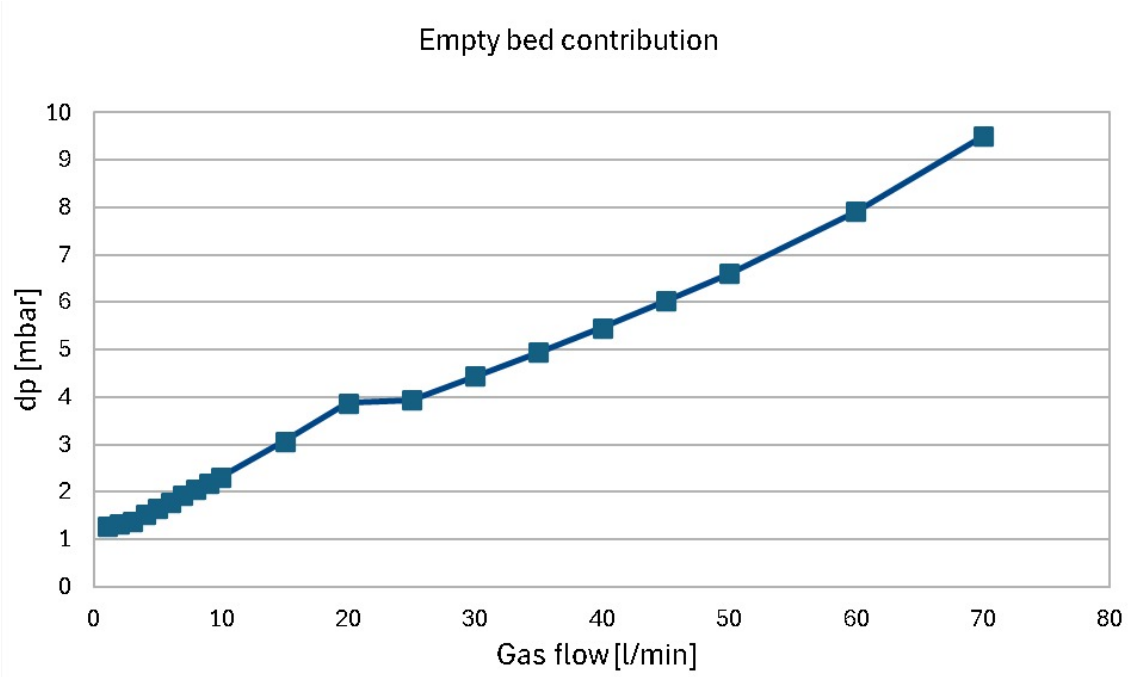


Figure A.2: Graph of the pressure drop through the diffuser. The step at 20 l/min is due to the change in flow controller, that, as stated previously, is less accurate at lower flows.

It is evident that, in these cases, the diffuser plate caused a pressure drop more than twice that of the powder bed.

To address this issue, a second series of experiments was carried out (the one actually shown in section 4.2.2). This time, only the first flow increase was analysed, since the previous results showed no significant differences between the decreasing and second increasing flow curves.

Bibliography

1. *Effects of climate change* Page Version ID: 1313801038. https://en.wikipedia.org/w/index.php?title=Effects_of_climate_change&oldid=1313801038 (2025).
2. *Recyclable metal fuels for clean and compact zero-carbon power - ScienceDirect* https://www.sciencedirect.com/science/article/pii/S0360128518300327?via%3Dihub (2025).
3. Wen, D. S. Nanofuel as a potential secondary energy carrier. *ResearchGate.* https://www.researchgate.net/publication/240497487_Nanofuel_as_a_potential_secondary_energy_carrier (2025) (2010).
4. Bergthorson, J. M. *et al.* Direct combustion of recyclable metal fuels for zero-carbon heat and power. *Applied Energy* **160,** 368–382. ISSN: 0306-2619. https://www.sciencedirect.com/science/article/pii/S0306261915011071 (2025) (Dec. 15, 2015).
5. Mignard, D. & Pritchard, C. A review of the sponge iron process for the storage and transmission of remotely generated marine energy. *International Journal of Hydrogen Energy* **32,** 5039–5049. ISSN: 0360-3199. https://www.sciencedirect.com/science/article/pii/S0360319907003679 (2025) (Dec. 1, 2007).
6. Mattisson, T., Lyngfelt, A. & Cho, P. The use of iron oxide as an oxygen carrier in chemical-looping combustion of methane with inherent separation of CO2. *Fuel* **80,** 1953–1962. ISSN: 0016-2361. https://www.sciencedirect.com/science/article/pii/S0016236101000515 (2025) (Oct. 1, 2001).
7. Lyngfelt, A. Chemical-looping combustion of solid fuels – Status of development. *Applied Energy* **113,** 1869–1873. ISSN: 0306-2619. https://www.sciencedirect.com/science/article/pii/S0306261913004558 (2025) (Jan. 1, 2014).
8. Nocera, D. G. The Artificial Leaf. *Accounts of Chemical Research* **45,** 767–776. ISSN: 0001-4842. https://doi.org/10.1021/ar2003013 (2025) (May 15, 2012).
9. Auner, N. & Holl, S. Silicon as energy carrier—Facts and perspectives. *Energy. ECOS 2003* **31,** 1395–1402. ISSN: 0360-5442. https://www.sciencedirect.com/science/article/pii/S0360544205002768 (2025) (Aug. 1, 2006).
10. Bardsley, W. E. The Sustainable Global Energy Economy: Hydrogen or Silicon? *Natural Resources Research* **17,** 197–204. ISSN: 1573-8981. https://doi.org/10.1007/s11053-008-9077-6 (2025) (Dec. 1, 2008).
11. Spreitzer, D. & Schenk, J. Reduction of Iron Oxides with Hydrogen—A Review. *steel research international* **90,** 1900108. ISSN: 1869-344X. https://onlinelibrary.wiley.com/doi/abs/10.1002/srin.201900108 (2025) (2019).

12. Habermann, A., Winter, F., Hofbauer, H., Zirngast, J. & Schenk, J. L. An Experimental Study on the Kinetics of Fluidized Bed Iron Ore Reduction. *ISIJ International* **40,** 935–942 (2000).

13. El-Geassy, A. A., Nasr, M. I., Khedr, M. & Abdel-Halim, K. S. Reduction Behaviour of Iron Ore Fluxed Pellets under Load at 1 023-1 273 K. *ISIJ International* **44,** 462–469 (2004).

14. Kawasaki, E., Sanscrainte, J. & Walsh, T. J. Kinetics of reduction of iron oxide with carbon monoxide and hydrogen. *AIChE Journal* **8,** 48–52. ISSN: 1547-5905. https://onlinelibrary.wiley.com/doi/abs/10.1002/aic.690080114 (2025) (1962).

15. Teplov, O. A. Kinetics of the low-temperature hydrogen reduction of magnetite concentrates. *Russian Metallurgy (Metally)* **2012,** 8–21. ISSN: 1555-6255. https://doi.org/10.1134/S0036029512010132 (2025) (Jan. 1, 2012).

16. Higuchi, K. & Heerema, R. H. Influence of Artificially Induced Porosity on Strength and Reduction Behavior of Hematite Compacts. *ISIJ International* **45,** 574–581 (2005).

17. *Gangue* Page Version ID: 1308694671. https://en.wikipedia.org/w/index.php?title=Gangue&oldid=1308694671 (2025).

18. Feinman, J., Smith, N. D. & Muskat, D. A. Effect of Gas Flow Rate on Kinetics of Reduction of Iron Oxide Pellets with Hydrogen. *Industrial & Engineering Chemistry Process Design and Development* **4,** 270–274. ISSN: 0196-4305. https://doi.org/10.1021/i260015a007 (2025) (July 1, 1965).

19. Perrone, A., Cavaliere, P., Sadeghi, B., Dijon, L. & Laska, A. Optimization of Hydrogen Utilization and Process Efficiency in the Direct Reduction of Iron Oxide Pellets: A Comprehensive Analysis of Processing Parameters and Pellet Composition. *steel research international* **96,** 2400565. ISSN: 1869-344X. https://onlinelibrary.wiley.com/doi/abs/10.1002/srin.202400565 (2025) (2025).

20. Zuo, H.-b., Wang, C., Dong, J.-j., Jiao, K.-x. & Xu, R.-s. Reduction kinetics of iron oxide pellets with H2 and CO mixtures. *International Journal of Minerals, Metallurgy, and Materials* **22,** 688–696. ISSN: 1869-103X. https://doi.org/10.1007/s12613-015-1123-x (2025) (July 1, 2015).

21. *Air - Diffusion Coefficients of Gases in Excess of Air* https://www.engineeringtoolbox.com/air-diffusion-coefficient-gas-mixture-temperature-d_2010.html (2026).

22. Lin, H.-Y., Chen, Y.-W. & Li, C. The mechanism of reduction of iron oxide by hydrogen. *Thermochimica Acta* **400,** 61–67. ISSN: 0040-6031. https://www.sciencedirect.com/science/article/pii/S0040603102004781 (2025) (Apr. 17, 2003).

23. Rippy, K., Bell, R. T. & Leick, N. Chemical and electrochemical pathways to low-carbon iron and steel. *npj Materials Sustainability* **2,** 33. ISSN: 2948-1775. https://www.nature.com/articles/s44296-024-00036-6 (2025) (Oct. 1, 2024).

24. Hui, W., Liu, L., Li, K. & Zhong, D. Modeling and Experimental Researches on Redox Reactions of Iron Ore Oxygen Carriers in Chemical Looping. *Engineering Reports* **7,** e13064. ISSN: 2577-8196. https://onlinelibrary.wiley.com/doi/abs/10.1002/eng2.13064 (2025) (2025).

25. Szekely, J. & Evans, J. W. A structural model for gas—solid reactions with a moving boundary. *Chemical Engineering Science* **25,** 1091–1107. ISSN: 0009-2509. https://www.sciencedirect.com/science/article/pii/0009250970850539 (2025) (Jan. 1, 1970).

26. Bhatia, S. K. & Perlmutter, D. D. A random pore model for fluid-solid reactions: I. Isothermal, kinetic control. *AIChE Journal* **26,** 379–386. ISSN: 1547-5905. https://onlinelibrary.wiley.com/doi/abs/10.1002/aic.690260308 (2025) (1980).

27. Bhatia, S. K. & Perlmutter, D. D. A random pore model for fluid-solid reactions: II. Diffusion and transport effects. *AIChE Journal* **27,** 247–254. ISSN: 1547-5905. https://onlinelibrary.wiley.com/doi/abs/10.1002/aic.690270211 (2025) (1981).

28. Bhaskar, A., Assadi, M. & Nikpey Somehsaraei, H. Decarbonization of the Iron and Steel Industry with Direct Reduction of Iron Ore with Green Hydrogen. *Energies* **13,** 758. ISSN: 1996-1073. https://www.mdpi.com/1996-1073/13/3/758 (2025) (Jan. 2020).

29. Hazlett, J. Entrainment From Gas-solid Fluidized Beds (volumes I And Ii). *Digitized Theses.* https://ir.lib.uwo.ca/digitizedtheses/1884 (Jan. 1, 1990).

30. Dry, M. The Fischer-Tropsch process: 1950-2000. *Catalysis Today* **71** (Jan. 15, 2002).

31. Chew, J. W., LaMarche, W. C. Q. & Cocco, R. A. 100 years of scaling up fluidized bed and circulating fluidized bed reactors. *Powder Technology* **409,** 117813. ISSN: 0032-5910. https://www.sciencedirect.com/science/article/pii/S0032591022007008 (2025) (Sept. 1, 2022).

32. Baddour, C. E. & Briens, C. Carbon Nanotube Synthesis: A Review. *International Journal of Chemical Reactor Engineering* **3.** ISSN: 1542-6580. https://www.degruyterbrill.com/document/doi/10.2202/1542-6580.1279/html (2025).

33. Grace, J. R. in *Essentials of Fluidization Technology* Section: 1 _eprint: https://onlinelibrary.wiley.
1–9 (John Wiley & Sons, Ltd, 2020). ISBN: 978-3-527-69948-3. https://onlinelibrary.wiley.com/doi/abs/10.1002/9783527699483.ch1 (2025).

34. Bi, H. T. & Grace, J. R. Flow regime diagrams for gas-solid fluidization and upward transport. *International Journal of Multiphase Flow* **21,** 1229–1236. ISSN: 0301-9322. https://www.sciencedirect.com/science/article/pii/030193229500037X (2025) (Nov. 1, 1995).

35. Geldart, D. The effect of particle size and size distribution on the behaviour of gas-fluidised beds. *Powder Technology* **6,** 201–215. ISSN: 0032-5910. https://www.sciencedirect.com/science/article/pii/0032591072830146 (2025) (Oct. 4, 1972).

36. Geldart, D. Types of gas fluidization. *Powder Technology* **7,** 285–292. ISSN: 0032-5910. https://www.sciencedirect.com/science/article/pii/0032591073800373 (2025) (May 1, 1973).

37. Grace, J. R. in *Essentials of Fluidization Technology* Section: 2 _eprint: https://onlinelibrary.wiley.
11–31 (John Wiley & Sons, Ltd, 2020). ISBN: 978-3-527-69948-3. https://onlinelibrary.wiley.com/doi/abs/10.1002/9783527699483.ch2 (2025).

38. Hausner, H. H. FRICTION CONDITIONS IN A MASS OF METAL POWDER. *Int. J. Powder Met., 3: No. 4, 7-13(Oct. 1967).* https://www.osti.gov/biblio/4566075 (2025) (Dec. 31, 1966).

39. *Surface roughness* Page Version ID: 1335672826. https://en.wikipedia.org/w/index.php?title=Surface_roughness&oldid=1335672826 (2026).

40. Nanayakkara, S. D. J. S., Zhao, J., Terrington, S. J., Thompson, M. C. & Hourigan, K. Effects of surface roughness on the drag coefficient of spheres freely rolling on an inclined plane. *Journal of Fluid Mechanics* **984,** A13. ISSN: 0022-1120, 1469-7645. https://www.cambridge.org/core/journals/journal-of-fluid-mechanics/article/effects-of-surface-roughness-on-the-drag-coefficient-of-spheres-freely-rolling-on-an-inclined-plane/EBAFFE51CF75D1D545CC27FFE6B20474 (2026) (Apr. 2024).

41. Wen, C. Y. & Yu, Y. H. A generalized method for predicting the minimum fluidization velocity. *AIChE Journal* **12,** 610–612. ISSN: 1547-5905. https://onlinelibrary.wiley.com/doi/abs/10.1002/aic.690120343 (2025) (1966).

42. Xu, C. C. & Zhu, J. Prediction of the Minimum Fluidization Velocity for Fine Particles of Various Degrees of Cohesiveness. *Chemical Engineering Communications* **196,** 499–517. ISSN: 0098-6445. https://doi.org/10.1080/00986440802483855 (2025) (Nov. 19, 2008).

43. Kuczynski, G. C. in *Sintering Key Papers* (eds Sōmiya, S. & Moriyoshi, Y.) 509–527 (Springer Netherlands, Dordrecht, 1990). ISBN: 978-94-009-0741-6. https://doi.org/10.1007/978-94-009-0741-6_33 (2025).

44. Hessels, C. J. M. *et al.* Minimum fluidization velocity and reduction behavior of combusted iron powder in a fluidized bed. *Fuel* **342,** 127710. ISSN: 0016-2361. https://www.sciencedirect.com/science/article/pii/S001623612300323X (2025) (June 15, 2023).

45. *Thermophysical Properties of Fluid Systems* https://webbook.nist.gov/chemistry/fluid/ (2025).

46. Wilke, C. R. A Viscosity Equation for Gas Mixtures. *Journal of Chemical Physics* **18,** 517–519. ISSN: 0021-9606. https://ui.adsabs.harvard.edu/abs/1950JChPh..18..517W (2025) (Apr. 1, 1950).

47. *Description - C 200* IKA. https://www.ika.com (2025).

48. https://analyzing-testing.netzsch.com/_Resources/Persistent/9/0/d/8/90d8410d1a7fd276ea43bb702c3a5ea5cece66ba/TG_209_F1_Libra_en_web.pdf.

49. https://ch.ntust.edu.tw/var/file/21/1021/img/1657/413568049.pdf.

50. https://www.meteo-tech.co.il/ImagesDownloadFiles/BELSORP-miniII.pdf.

51. *X-ray scattering techniques* Page Version ID: 1280267937. https://en.wikipedia.org/w/index.php?title=X-ray_scattering_techniques&oldid=1280267937 (2025).

52. Inc, M. P. *Electron Microscope and Analysis | Tech* Matsusada Precision. https://www.matsusada.com/column/sem-tech3.html (2025).

53. *The Assay Guide to Iron Ore* https://www.theassay.com/articles/the-assay-insights/the-assay-guide-to-iron-ore/ (2025).

54. Raghavan, V. Al-Fe-O (Aluminum-Iron-Oxygen). *Journal of Phase Equilibria and Diffusion* **31,** 367–367. ISSN: 1863-7345. https://doi.org/10.1007/s11669-010-9712-x (2025) (Aug. 1, 2010).

55. Transformation of the Corundum Structure upon High-Temperature Reduction. *ResearchGate.* https://www.researchgate.net/publication/215470635_Transformation_of_the_Corundum_Structure_upon_High-Temperature_Reduction (2025) (Aug. 7, 2025).

56. Kaplan, A. F. H., Fedina, T., Brueckner, F. & Powell, J. Laser induced reduction of iron ore by silicon. *Journal of Alloys and Metallurgical Systems* **4,** 100039. ISSN: 2949-9178. https://www.sciencedirect.com/science/article/pii/S2949917823000391 (2025) (Dec. 1, 2023).

57. *A Review on Prevention of Sticking during Fluidized Bed Reduction of Fine Iron Ore* https://www.jstage.jst.go.jp/article/isijinternational/60/1/60_ISIJINT-2019-392/_html/-char/en (2025).

58. Characterization of Chemical Composition and Microstructure of Natural Iron Ore from Muko Deposits. *ResearchGate.* https://www.researchgate.net/publication/258403487_Characterization_of_Chemical_Composition_and_Microstructure_of_Natural_Iron_Ore_from_Muko_Deposits (2025) (Aug. 6, 2025).

59. Deer, W. A., Howie, R. A. & Zussman, J. *An Introduction to the Rock-Forming Minerals* ISBN: 978-0-903056-43-4. https://pubs.geoscienceworld.org/minersoc/books/book/952/An-Introduction-to-the-Rock-Forming-Minerals (2025) (Mineralogical Society of Great Britain and Ireland, Jan. 1, 2013).

60. Influence of magnesia on sintering characteristics of iron ore. *ResearchGate.* https://www.researchgate.net/publication/233632208_Influence_of_magnesia_on_sintering_characteristics_of_iron_ore (2025).

61. Seitz, M. *et al. Influence of Initial Morphology on Reduction of Micron-Sized Iron Oxide Particles in a Fluidized Bed Reactor with Hydrogen: Morphology and Phase Analysis* Rochester, NY, Mar. 13, 2025. https://papers.ssrn.com/abstract=5177544 (2025).

62. Liu, X. *et al.* Regeneration of iron fuel in fluidized beds Part II: Reduction experiments. *Powder Technology* **420,** 118183. ISSN: 0032-5910. https://www.sciencedirect.com/science/article/pii/S0032591022010646 (2025) (Apr. 15, 2023).

63. Liu, X. *et al.* Regeneration of iron fuel in fluidized beds, Part I: Defluidization experiments and theoretical prediction model. *Powder Technology* **420,** 118182. ISSN: 0032-5910. https://www.sciencedirect.com/science/article/pii/S0032591022010634 (2025) (Apr. 15, 2023).

64. *Adsorption* Page Version ID: 1304065158. https://en.wikipedia.org/w/index.php?title=Adsorption&oldid=1304065158#BET (2025).

65. Nikolaeva, N. V., Aleksandrova, T. N., Chanturiya, E. L. & Afanasova, A. Mineral and Technological Features of Magnetite–Hematite Ores and Their Influence on the Choice of Processing Technology. *ACS Omega* **6,** 9077–9085. ISSN: 2470-1343. https://www.ncbi.nlm.nih.gov/pmc/articles/PMC8028150/ (2025) (Mar. 24, 2021).

66. Kiessling, R. Clean steel - a debatable concept. *Metal Science.* ISSN: 0267-0836. https://www.tandfonline.com/doi/abs/10.1080/02670836.2020.12097372 (2025) (Apr. 1, 1980).

67. *Hercynite* Page Version ID: 1268964682. https://en.wikipedia.org/w/index.php?title=Hercynite&oldid=1268964682 (2025).

68. Liu, W. *et al.* Kinetics of the reduction of wüstite by hydrogen and carbon monoxide for the chemical looping production of hydrogen. *Chemical Engineering Science* **120,** 149–166. ISSN: 0009-2509. https://www.sciencedirect.com/science/article/pii/S000925091400428X (2025) (Dec. 16, 2014).

69. Zhang, Z. The Characteristics and Reduction of Wustite. https://www.intechopen.com/chapters/1126784 (2025) (Mar. 7, 2023).

70. *Influence of the Original Structure on the Kinetics of Hydrogen Reduction of Hematite Compacts* https://www.jstage.jst.go.jp/article/isijinternational1966/28/8/28_8_650/_article/-char/ja/ (2025).

71. El-Rahaiby, S. K. & Rao, Y. K. The kinetics of reduction of iron oxides at moderate temperatures. *Metallurgical Transactions B* **10,** 257–269. ISSN: 2379-0229. https://doi.org/10.1007/BF02652470 (2025) (June 1, 1979).

72. Zheng, H., Schenk, J., Spreitzer, D., Wolfinger, T. & Daghagheleh, O. Review on the Oxidation Behaviors and Kinetics of Magnetite in Particle Scale. *steel research international* **92,** 2000687. ISSN: 1869-344X. https://onlinelibrary.wiley.com/doi/10.1002/srin.202000687 (2025) (Aug. 1, 2021).

73. Hasanbeigi, A., Arens, M. & Price, L. Alternative emerging ironmaking technologies for energy-efficiency and carbon dioxide emissions reduction: A technical review. *Renewable and Sustainable Energy Reviews* **33,** 645–658. ISSN: 1364-0321. https://www.sciencedirect.com/science/article/pii/S136403211400152X (2025) (May 1, 2014).

74. Mali, H. & Spuida, B. Automatisierte Mikrobild-Analyse zur Klassifizierung von Eisenerz für die Roheisenherstellung. *BHM Berg- und Hüttenmännische Monatshefte* **158,** 47–52. ISSN: 1613-7531. https://doi.org/10.1007/s00501-013-0119-y (2025) (Feb. 1, 2013).

75. Li, P., Li, Y., Yu, J., Gao, P. & Han, Y. Kinetics and microstructural changes during fluidized reduction of magnetite with hydrogen at low temperatures. *International Journal of Hydrogen Energy* **47,** 31140–31151. ISSN: 0360-3199. https://www.sciencedirect.com/science/article/pii/S0360319922030464 (2025) (Aug. 26, 2022).

76. Sathiyamoorthy, D. & Horio, M. On the influence of aspect ratio and distributor in gas fluidized beds. *Chemical Engineering Journal* **93,** 151–161. ISSN: 1385-8947. https://www.sciencedirect.com/science/article/pii/S1385894702002577 (2025) (June 15, 2003).

77. Cocco, R., Karri, S. B. R. & Knowlton, T. Introduction to Fluidization. *Back to Basics* (2014).

78. *National Institute of Standards and Technology* NIST. Last Modified: 2025-09-10T11:13-04:00. https://www.nist.gov/ (2025).

79. *Stokes' law* Page Version ID: 1287866591. https://en.wikipedia.org/w/index.php?title=Stokes%27_law&oldid=1287866591#Terminal_velocity_of_sphere_falling_in_a_fluid (2025).

80. Bi, X. in *Essentials of Fluidization Technology* Section: 4 _eprint: https://onlinelibrary.wiley.com/d 55–74 (John Wiley & Sons, Ltd, 2020). ISBN: 978-3-527-69948-3. https://onlinelibrary.wiley.com/doi/abs/10.1002/9783527699483.ch4 (2025).

81. Ellis, N. Experimental Investigation of Fluidized Bed Systems, 75–108. https://onlinelibrary.wiley.com/doi/abs/10.1002/9783527699483.ch5 (2025) (2020).

Acknowledgements